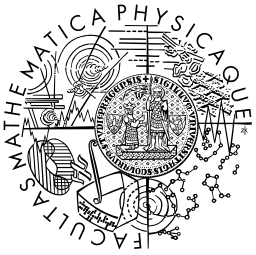

FACULTY
OF MATHEMATICS
AND PHYSICS
Charles University

DOCTORAL THESIS

Mgr. Aleš Kuchař

Coupling processes of various timescales in the middle atmosphere

Department of Atmospheric Physics

Supervisor of the doctoral thesis:	doc. RNDr. Petr Pišoft, Ph.D.
Study programme:	Physics
Study branch:	Meteorology and Climatology

Prague 2018

I declare that I carried out this doctoral thesis independently, and only with the cited sources, literature and other professional sources.

I understand that my work relates to the rights and obligations under the Act No. 121/2000 Sb., the Copyright Act, as amended, in particular the fact that the Charles University has the right to conclude a license agreement on the use of this work as a school work pursuant to Section 60 subsection 1 of the Copyright Act.

In ..... date ..... signature of the author

Firstly, I would like to express my gratitude to my supervisor Petr Pišoft for his leadership during my PhD studies. Petr Šácha deserves many thanks for his valuable advises and productive collaboration on our common projects.

I would also like to thank Thomas Peter for giving me the opportunity to spend such a productive year in his Atmospheric Chemistry research group. Special thanks to William Ball, Eugene Rozanov and Andrea Stenke for their guidance and fruitful collaboration during my research stay in Zurich. I should not forget about my officemates and friends Pavle Arsenovic and Blaž Gasparini who provided me second home in Zurich. Many thanks to the co-authors of my publication for their diverse contribution.

However, the biggest thanks belong to my family and partner Eliška without their unlimited support and love this would never happen.

Finally, I am grateful to the whole python open-source community for amazing tools I could use in this thesis and partly contribute to as well.

This thesis was supported by the Charles University, Grant Agency project 1474314, the Czech Science Foundation (GAČR) 16-01562J, and by the Swiss Government Excellence Scholarship, reference 2014.0190.

Title: Coupling processes of various timescales in the middle atmosphere

Author: Mgr. Aleš Kuchař

Department: Department of Atmospheric Physics

Supervisor: doc. RNDr. Petr Pišoft, Ph.D., Department of Atmospheric Physics

Abstract: The thesis deals with the manifestation of coupling processes of various timescales in the middle atmosphere. Longer and shorter timescales are represented here by the 11-year solar cycle (SC) and orographic gravity waves (oGWs) considered on the intraseasonal timescale of the north hemisphere winter, respectively. The first two chapters deal with the application of rigorous attribution the variability of temperature, ozone and circulation characteristics in the stratosphere and lower mesosphere with regard to the SC using multiple nonlinear techniques (support vector regression and neural networks) besides the multiple linear regression approach. The aliasing of the SC with volcanic eruptions or the El Niño Southern Oscillation is qualitatively assessed and its impact on conclusions about the top-down coupling mechanisms discussed. The last chapter examines the role of parametrized oGWs in the lower stratosphere. The Himalayan hotspot reveals common features with sudden stratospheric warmings such as the residual circulation amplification leading to a warming and ozone enrichment in the polar latitudes of the lower stratosphere.

Keywords: middle atmosphere, 11-year solar cycle, attribution techniques, wave-mean flow interactions, coupling processes

Contents

Introduction

The thesis deals with the manifestation of so-called top-down and bottom-up coupling processes of various timescales in the middle atmosphere. The formal structure of this thesis adopts a form of *compilation thesis*, i.e. the thesis is presented as a collection of papers that have been published or prepared for further publication.

The atmosphere, is among other criteria, divided into layers based on the vertical temperature gradient (see Fig. 1). Andrews and McIntyre (1987) have defined the middle atmosphere as a region from the tropopause (10-16 km) to the homopause ($\sim$110 km), i.e. the region where eddy mixing dominates over molecular diffusion. Since most of tools for the middle atmosphere research, such as chemistry-climate models and reanalyses, do not represent the thermosphere, in this thesis the middle atmosphere represents the region of the stratosphere and mesosphere.

Understanding of either top-down or bottom-up coupling mechanisms between, in particular between troposphere, stratosphere and mesosphere still remains a significant challenge for the middle atmosphere research. As a top-down mechanism on decadal timescale here is considered the 11-year solar cycle variation in ultra-violet (UV) irradiance which causes changes in stratospheric temperature and ozone (Gray et al., 2010). It has been hypothesized (Kodera and Kuroda, 2002) that the downward propagation of these changes is the prime stratosphere-troposphere coupling mechanism of the solar influence on climate (Haigh, 1994). However, it has been shown later (Rozanov et al., 2005; Seppälä et al., 2014) that the solar activity in the form of solar storms and geomagnetic disturbances could be the missing top-down link from the mesosphere to the surface. The bottom-up mechanism includes changes near the Earth's surface induced by the (non-UV) total solar irradiance (TSI) variations propagating upwards (Meehl et al., 2009). Furthermore, there is a evidence about the similar stratospheric pathway to the surface and bottom-up influence initiated by surface cooling in occurrence of volcanic eruptions (Robock, 2000; Graf et al., 2007).

The top-down and bottom-up mechanisms are not necessarily mutually exclusive since UV-induced changes in the upper stratosphere propagating downwards can partly drive the troposphere-ocean response, in addition to direct forcing by TSI variations at the surface (Hood and Soukharev, 2012). In addition, the downward propagation of the solar-induced changes in the stratosphere modulates planetary and gravity wave propagation from below and can indirectly affect the temperature distribution in the mesosphere and lower thermosphere (Cullens et al., 2016). Moreover, studies show that the stratosphere-troposphere coupling mechanisms may be modulated by phases of the quasi-biennial oscillation (Labitzke, 1987; Lu et al., 2009; Matthes et al., 2013) or by the occurrence of sudden stratospheric warmings (Gray et al., 2004; Cnossen et al., 2011; Seppälä et al., 2013). Therefore, it is very challenging to understand top-down and bottom-up contributions to climate effects of the solar activity, volcanic eruptions and their potential aliasing on decadal timescales (Chiodo et al., 2014), Furthermore, disentangling these mechanisms from atmosphere-ocean modes of internal variability such as e.g. the El Niño Southern Oscillation (Marsh and Garcia, 2007) or the

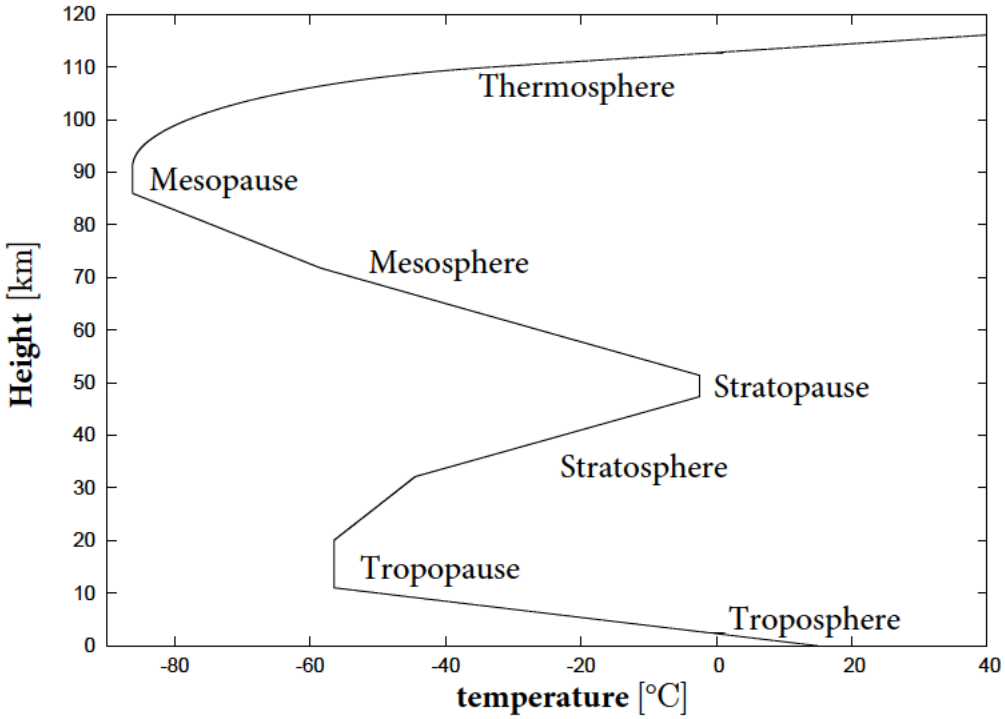

Figure 1: Midlatitude temperature profile. Based on Standard atmosphere (1976).

North Atlantic Oscillation (Thiéblemont et al., 2015) presents another challenge.

The stratosphere-troposphere dynamical coupling through a perturbation, e.g. in the form of a stratospheric heating, leads to an increase in the strength of the stratospheric circumpolar jet and manifests in a poleward shift of the tropospheric jet stream and an increase in the meridional pressure gradient near the surface (Baldwin and Dunkerton, 1999). Although the underlying dynamical mechanisms may not be fully understood, a single unifying mechanism may act across different timescales ranging from daily to decadal variations (Garfinkel et al., 2015; Kidston et al., 2015). Attribution of robust and realistic signals in observational datasets and their reproduction in model simulations is essential for the understanding the stratosphere-troposphere dynamical coupling mechanisms (Gerber et al., 2012) and may increase the confidence in climate projections on various timescales (Kidston et al., 2015).

This thesis addresses the attributions of the coupling processes of various timescales in the middle atmosphere. The first chapter, published as Kuchar et al. (2015), investigates the attribution of the variability of temperature, ozone and circulation patterns in the stratosphere and lower mesosphere with regard to the 11-year solar cycle. The second chapter (Kuchar et al., 2017) deals with the aliasing of the solar cycle with volcanic eruptions and ENSO influence in the lower stratospheric tropical temperature. These results may enrich our understanding of propagation of stratospheric temperature perturbations implied by the 11-year solar cycle. The third chapter (Kuchar et al., in prep.) examines the role of parametrized oGWs in the lower stratosphere, i.e. in the regions of significant mountain wave breaking between tropospheric and stratospheric jet. Furthermore, we hypothesize their possible links to SSW events. The concluding chapter brings out the major findings of each chapter, conclusions and the outlook of the

thesis.

In this thesis we try to adopt open-science features (e.g. Gewin, 2016) either by publishing calculation scripts (Kuchar, 2015) or produced datasets (Kuchar and Revell, 2017; Kuchar, 2018). This should ensure a reproducibility of results and further research of the middle atmosphere which may be out of scope of this thesis.

1. The 11-year solar cycle in current reanalyses: a (non)linear attribution study of the middle atmosphere

1.1 Introduction

The Sun is a prime driver of various processes in the climate system. From observations of the Sun's variability on decadal or centennial timescales, it is possible to identify temporal patterns and trends in solar activity, and consequently to derive the related mechanisms of the solar influence on the Earth's climate (e.g. Gray et al., 2010). Of the semi-regular solar cycles, the most prominent is the approximate 11-year periodicity which manifests in the solar magnetic field or through fluctuations of sunspot number, but also in the total solar irradiance (TSI) or solar wind properties. For the dynamics of the middle atmosphere, where most of the ozone production and destruction occur, the changes in the spectral solar irradiance (SSI) are the most influential, since the TSI as the integral over all wavelengths exhibits variations of orders lower than the ultraviolet part of the spectrum (Lean, 2001). This fact was supported by original studies (e.g. Labitzke, 1987; Haigh, 1994) that suggested the solar cycle (SC) influence on the variability of the stratosphere. Gray et al. (2009) have shown, with the fixed dynamical heating model, that the response of temperature in the photochemically controlled region of the upper tropical stratosphere is due to both direct solar heating and an indirect effect caused by the ozone changes.

Numerous studies have identified temperature and ozone changes linked to the 11-year cycle by multiple linear regression. The use of ERA-40 reanalysis (Frame and Gray, 2010) pointed to a manifestation of annually averaged solar signal in temperature, exhibited predominantly around the Equator with amplitudes up to 2 K around the stratopause and with a secondary amplitude maximum of up to 1 K in the lower stratosphere. Soukharev and Hood (2006), Hood et al. (2010) and Randel and Wu (2007) have used satellite ozone data sets to characterise statistically significant responses in the upper and lower stratosphere. The observed double-peaked ozone response in the vertical profile around the Equator was reproduced in some chemistry climate models, although concerns about the physical mechanism of the lower stratospheric response were expressed (Austin et al., 2008).

The ozone and temperature perturbations associated with the SC have an impact on the middle atmospheric circulation. They produce a zonal wind anomaly around the stratopause (faster subtropical jet) during solar maxima through the enhanced meridional temperature gradient. Since planetary wave propagation is affected by the zonal mean flow (Andrews and McIntyre, 1987), we can suppose that a stronger subtropical jet can deflect planetary waves propagating from higher latitudes. Reduced wave forcing can lead to decreasing/increasing or upwelling/downwelling motions in the equatorial or higher latitudes respectively

(Kodera and Kuroda, 2002). The Brewer–Dobson circulation (BDC) is weaker during solar maxima (Kuroda and Kodera, 2001), although this appears to be sensitive to the state of the polar winter. Observational studies, together with model experiments (e.g. Matthes et al., 2006), suggest a so-called "top-down" mechanism where the solar signal is transferred from the upper to lower stratosphere, and even to tropospheric altitudes.

Statistical studies (e.g. Labitzke et al., 2006; Camp and Tung, 2007) have also focused on the lower stratospheric solar signal in the polar regions and have revealed modulation by the Quasi-Biennial Oscillation (QBO), or the well known Holton–Tan relationship (Holton and Tan, 1980) modulated by the SC. Proposed mechanisms by Matthes et al. (2004, 2010) suggested that the solar signal induced during early winter in the upper equatorial stratosphere propagates poleward and downward when the stratosphere transits from a radiatively controlled state to a dynamically controlled state involving planetary wave propagation (Kodera and Kuroda, 2002). The mechanism of the SC and QBO interaction, which stems from reinforcing each other or canceling each other out (Gray et al., 2004), has been verified by WACCM3.1 model simulations (Matthes et al., 2013). These proved the independence of the solar response in the tropical upper stratosphere from the response dependent on the presence of the QBO at lower altitudes. However, fully coupled WACCM-4 model simulations by Kren et al. (2014) raised the possibility of occurrence by chance of the observed solar-QBO response in the polar region. The internally generated QBO was not fully realistic though. In particular, the simulated internal QBO descended down to only about 50 hPa.

It has been shown that difficulties in the state-of-the-art climate models arise when reproducing the solar signal influence on winter polar circulation, especially in less active sun periods (Ineson et al., 2011). The hypothesis is that solar UV forcing is too weak in the models. Satellite measurements indicate that variations in the solar UV irradiance may be larger than previously thought (Harder et al., 2009). However, the measurements by Harder et al. (2009) from the SORCE satellite may have been affected by instrument degradation with time and so may be overestimating the UV variability (see the review by Ermolli et al., 2013). The latter authors have also concluded that the SORCE measurements probably represent an upper limit on the magnitude of the SSI variation. Consequent results of general circulation models, forced with the SSI from the SORCE measurements, have shown a larger stratospheric response than for the NRL SSI data set. Thus, coordinated work is needed to have reliable SSI input data for GCM and CCM simulations (Ermolli et al., 2013), and also to propose robust conclusions concerning SC influence on climate (Ball et al., 2014b).

At the Earth's surface, the detection of the SC influence is problematic since there are other significant forcing factors, e.g. greenhouse gases, volcanoes and aerosol changes (e.g. Chiodo et al., 2012), as well as substantial variability attributable to internal climate dynamics. However, several studies (van Loon et al., 2007; van Loon and Meehl, 2008; Hood and Soukharev, 2012; Hood et al., 2013; Gray et al., 2013; Scaife et al., 2013) detected the solar signal in sea level pressure and sea surface temperature, which supports the hypothesis of a troposphere–ocean response to the SC. Some studies (e.g. Hood and Soukharev, 2012) suggest a so-called "bottom-up" solar forcing mechanism that contributes to the lower stratospheric ozone and temperature anomaly in connection with the

lower stratosphere deceleration of the BDC.

The observed double-peaked ozone anomaly in the vertical profile around the Equator was supported by the simulations of coupled chemistry climate models (Austin et al., 2008). However, the results presented by Chiodo et al. (2014) suggest the contribution of SC variability could be smaller since two major volcanic eruptions are aligned with solar maximum periods and also given the shortness of the analysed time series (in our case, 35 years). These concerns related to the lower stratospheric response of ozone and temperature derived from observations have already been raised (e.g. Solomon et al., 1996; Lee and Smith, 2003). However, another issue is whether or not the lower stratospheric response could depend on the model employed in the simulations (Mitchell et al., 2015c).

Several past studies (e.g. Soukharev and Hood, 2006; Frame and Gray, 2010; Gray et al., 2013; Mitchell et al., 2015b) used multiple linear regression to extract the solar signal and separate other climate phenomena like the QBO, the effect of aerosols, North Atlantic Oscillation (NAO), El Niño–Southern Oscillation (ENSO) or trend variability. Apart from this conventional method, it is possible to use alternative approaches to isolate and examine particular signal components, such as wavelet analysis (Pisoft et al., 2012, 2013) or empirical mode decomposition (Coughlin and Tung, 2004). The nonlinear character of the climate system also suggests potential benefits from the application of fully nonlinear attribution techniques to study the properties and interactions in the atmosphere. However, such nonlinear methods have been used rather sporadically in the atmospheric sciences (e.g. Walter and Schönwiese, 2003; Pasini et al., 2006; Blume and Matthes, 2012), mainly due to their several disadvantages such as the lack of explanatory power (Olden and Jackson, 2002).

To examine middle atmospheric conditions, it is necessary to study reliable and sufficiently vertically resolved data. Systematic and global observations of the middle atmosphere only began during the International Geophysical Year (1957–1958) and were later expanded through the development of satellite measurements (Andrews and McIntyre, 1987). Supplementary data come from balloon and rocket soundings, though these are limited by their vertical range (only the lower stratosphere in the case of radiosondes) and the fact that the in situ observations measure local profiles only. By assimilation of these irregularly distributed data and discontinuous measurements of particular satellite missions into an atmospheric/climatic model, we have modern basic data sets available for climate research, so-called reanalyses. These types of data are relatively long, globally gridded with a vertical range extending to the upper stratosphere or the lower mesosphere and thus suitable for 11-year SC research. In spite of their known limitations (such as discontinuities in ERA reanalysis – McLandress et al., 2014), they are considered an extremely valuable research tool (Rienecker et al., 2011).

Coordinated intercomparison has been initiated by the SPARC (Stratospheric Processes and their Role in Climate) community to understand them, and to contribute to future reanalysis improvements (Fujiwara et al., 2012). Under this framework, Mitchell et al. (2015b) have examined nine reanalysis data sets in terms of 11-year SC, volcanic, ENSO and QBO variability. Complementing their study, we provide here a comparison with nonlinear regression techniques, assessing robustness of the results obtained by multiple linear regression (MLR). Furthermore, EP flux diagnostics are used to examine solar-induced response

during the winter season in both hemispheres, and solar-related variations of assimilated ozone are investigated.

The paper is arranged as follows. In Sect. 1.2 the used data sets are described. In Sect. 1.3 the analysis methods are presented along with regressor terms employed in the regression model. Section 1.4 is dedicated to the description of the annual response results. In Sect. 1.4.1 solar response in MERRA reanalysis is presented. Next, in Sect. 1.4.1 other reanalyses are compared in terms of SC. Comparison of linear and nonlinear approaches is presented in Sect. 1.4.1. Section 1.4.2 describes monthly evolution of SC response in the state variables. Section 1.5 is aimed at dynamical consequences of the SC analysed using the EP flux diagnostics.

1.2 Data sets

Our analysis was applied to the most recent generation of three reanalysed data sets: MERRA (Modern Era Reanalysis for Research and Applications, developed by NASA) (Rienecker et al., 2011), ERA-Interim (ECMWF Interim Reanalysis) (Dee et al., 2011a) and JRA-55 (Japanese 55-year Reanalysis) (Ebita et al., 2011). We have studied the series for the period 1979–2013. All of the data sets were analysed on a monthly basis. The Eliassen–Palm (EP) flux diagnostics (described below) was computed on a 3-hourly basis from MERRA reanalysis and subsequently monthly means were produced. A similar approach has already been used by Seviour et al. (2012) and Mitchell et al. (2015a). The former study proposed that even 6-hourly data are sufficient to diagnose tropical upwelling in the lower stratosphere. The vertical range extends to the lower mesosphere (0.1 hPa) for MERRA, and to 1 hPa for the remaining reanalyses. The horizontal resolution of the gridded data sets was $1.25^\circ \times 1.25^\circ$ for MERRA and JRA-55 and $1.5^\circ \times 1.5^\circ$ for ERA-Interim respectively.

In comparison with previous generations of reanalyses, it is possible to observe a better representation of stratospheric conditions. This improvement is considered to be connected with increasing the height of the upper boundary of the model domain (Rienecker et al., 2011). For example, the Brewer–Dobson circulation was markedly overestimated by ERA-40; an improvement was achieved in ERA-Interim, but the upward transport remains faster than observations indicate (Dee et al., 2011a). Interim results of JRA-55 suggest a less biased reanalysed temperature in the lower stratosphere relative to JRA-25 (Ebita et al., 2011).

In addition to the standard variables provided in reanalysis, i.e. air temperature, ozone mixing ratio and circulation characteristics – zonal, meridional or omega velocity – we have also analysed other dynamical variables. Of particular interest were the EP flux diagnostics – a theoretical framework to study interactions between planetary waves and the zonal mean flow (Andrews and McIntyre, 1987). Furthermore, this framework allows the study of the wave propagation characteristics in the zonal wind and the induced (large-scale) meridional circulation as well. For this purpose the quasi-geostrophic approximation of transformed Eulerian mean (TEM) equations were used in the form employed by Edmon Jr et al. (1980), i.e. using their formula (3.1) for EP flux vectors, (3.2) for EP flux divergence and (3.4) for residual circulation. These variables were then interpolated to a regular vertical grid. For the visualisation purposes, the EP flux arrows were

scaled by the inverse of the pressure. The script was publicly released (Kuchar, 2015).

1.3 Methods

To detect variability and changes due to climate-forming factors, such as the 11-year SC, we have applied an attribution analysis based on multiple linear regression (MLR) and two nonlinear techniques. The regression model separates the effects of climate phenomena that are supposed to have an impact on middle atmospheric conditions. Our regression model of a particular variable X as a function of time t, pressure level p, latitude φ and longitude λ is described by the following equation:

$$\begin{aligned} X(t,z,\varphi,\lambda) =& \alpha(t;z,\varphi,\lambda) + \beta(z,\varphi,\lambda)\,\mathrm{TREND}(t) \\ &+\gamma(z,\varphi,\lambda)\,\mathrm{SOLAR}(t) + \delta_1(z,\varphi,\lambda)\,\mathrm{QBO}_1(t) \\ &+\delta_2(z,\varphi,\lambda)\,\mathrm{QBO}_2(t) + \delta_3(z,\varphi,\lambda)\,\mathrm{QBO}_3(t) \\ &+\varepsilon(z,\varphi,\lambda)\,\mathrm{ENSO}(t) + \zeta(z,\varphi,\lambda)\,\mathrm{SAOD}(t) \\ &+\eta(z,\varphi,\lambda)\,\mathrm{NAO}(t) + e(t,z,\varphi,\lambda). \end{aligned} \tag{1.1}$$

After deseasonalising, which can be represented by the α index for every month in a year, the individual terms represent a trend regressor $\mathrm{TREND}(t)$ either in linear form or including the equivalent effective stratospheric chlorine (EESC) index (this should be employed due to the ozone turnover trend around the middle of the 90s), a $\mathrm{SOLAR}(t)$ represented by the 10.7 cm radio flux as a proxy for solar ultraviolet variations at wavelengths 200–300 nm that are important for ozone production and radiative heating in the stratosphere, and which correlates well with sunspot number variation (the data were acquired from Dominion Radio Astrophysical Observatory (DRAO) in Penticton, Canada).

We have also included the quasi-biennial proxies $\mathrm{QBO}_{1,2,3}(t)$ as another stratosphere-related predictor. Similar studies have represented the QBO in multiple regression methods in several ways. Our approach involves three separate QBO indices extracted from each reanalysis. These three indices are the first three principal components of the residuals of our linear regression model (1.1) excluding QBO predictors applied to the equatorial zonal wind. The approach follows the paper by Frame and Gray (2010) or the study by Crooks and Gray (2005) to avoid contamination of the QBO regressors by the solar signal or other regressors. The three principal components explain 49, 47 and 3 % of the total variance for the MERRA; 60, 38 and 2 % for the JRA-55; and 59, 37 and 3 % for the ERA-Interim. The extraction of the first two components reveals a 28-month periodicity and an out-of phase relationship between the upper and lower stratospheres. The out-of phase relationship or orthogonality manifests approximately in a quarter period shift of these components. The deviation from the QBO quasi-regular period represented by the first two dominant components is contained in the residual variance. Linear regression analysis of the zonal wind with the inclusion of the first two principal components reveals a statistically significant linkage between the third principal component and the residuals of this analysis. Furthermore, the regression coefficient of this QBO proxy was statistically significant for all variables p value < 0.05 (see below for details about significance testing techniques).

Wavelet analysis for the MERRA demonstrates three statistically significant but non-stationary periods exceeding the level of the white noise wavelet spectrum (not shown): an approximate annual cycle (a peak period of 1 year and 2 months), a cycle with a peak period of 3 years and 3 months and a long-period cycle (a peak period between 10 and 15 years). Those interferences can be attributed to the possible nonlinear interactions between the QBO itself and other signals like the annual cycle or long-period cycle such as the 11-year SC at the equatorial stratosphere.

The El Niño–Southern Oscillation is represented by the multivariate ENSO index ENSO(t) which is computed as the first principal component of the six main observed variables over the Pacific Ocean: sea level pressure, zonal and meridional wind, sea surface temperature, surface air temperature and total cloudiness fraction of the sky (NCAR, 2013). The effect of volcanic eruptions is represented by the stratospheric aerosol optical depth SAOD(t). The time series was derived from the optical extinction data (Sato et al., 1993). We have used globally averaged time series in our regression model. The North Atlantic Oscillation has also been included through its index NAO(t) derived by rotated principal component analysis applied to the monthly standardised 500 hPa height anomalies obtained from the Climate Data Assimilation System (CDAS) in the Atlantic region between 20 and 90° N (NOAA, 2013).

The robustness of the solar regression coefficient has been tested in terms of including or excluding particular regressors in the regression model; e.g. the NAO term was removed from the model and the resulting solar regression coefficient was compared with the solar regression coefficient from the original regression set-up. The solar regression coefficient seems to be highly robust since neither the amplitude nor the statistical significance field was changed significantly when NAO or QBO_3 or both of them were removed. However, cross-correlation analysis reveals that the correlation between NAO and TREND, SOLAR and SAOD regressors is statistically significant, but small (not shown).

The multiple regression model of Eq. (1.1) has been used for the attribution analysis, and supplemented by two nonlinear techniques. The MLR coefficients were estimated by the least squares method. To avoid the effect of autocorrelation of residuals and to obtain the best linear unbiased estimate (BLUE) according to the Gauss–Markov theorem (Thejll, 2005), we have used an iterative algorithm to model the residuals as a second-order autoregressive process. A Durbin–Watson test (Durbin and Watson, 1950) confirmed that the regression model was sufficient to account for most of the residual autocorrelations in the data.

As a result of the uncorrelated residuals, we can suppose the standard deviations of the estimated regression coefficients not to be diminished (Neter et al., 2004). The statistical significance of the regression coefficients was computed with a t test.

The nonlinear approach, in our case, consisted of a multi-layer perceptron (MLP) and the relatively novel epsilon support vector regression (ε–SVR) technique with the threshold parameter $\varepsilon = 0.1$. The MLP as a technique inspired by the human brain is capable of capturing nonlinear interactions between inputs (regressors) and output (modelled data) (e.g. Haykin, 2009). The nonlinear approach is achieved by transferring the input signals through a sigmoid function in a particular neuron and within a hidden layer propagating to the output (a so-

called feed–forward propagation). The standard error back–propagation iterative algorithm to minimise the global error has been used.

The support vector regression technique belongs to the category of kernel methods. Input variables were nonlinearly transformed to a high-dimensional space by a radial basis (Gaussian) kernel, where a linear classification (regression) can be constructed (Cortes and Vapnik, 1995). However, cross-validation must be used to establish a kernel parameter and cost function searched in the logarithmic grid from 10^{-5} to 10^{1} and from 10^{-2} to 10^{5} respectively. We have used 5-fold cross-validation to optimise the SVR model selection for every point in the data set as a trade-off between the recommended number of folds (Kohavi, 1995) and computational time. The MLP model was validated by the holdout cross-validation method since this method is more expensive in order of magnitude in terms of computational time. The data sets were separated into a training set (75 % of the whole data set) and a testing set (25 % of the whole data set). The neural network model was restricted to only one hidden layer with the maximum number of neurons set up to 20.

The earlier mentioned lack of explanatory power of the nonlinear techniques in terms of complicated interpretation of statistical models (Olden and Jackson, 2002) mainly comes from nonlinear interactions during signal propagation and the impossibility to directly monitor the influence of the input variables. In contrast to the linear regression approach, the understanding of relationships between variables is quite problematic. For this reason, the responses of our variables have been modelled by a technique originating from sensitivity analysis studies and also used by e.g. Blume and Matthes (2012). The relative impact RI of each variable was computed as

$$\mathrm{RI} = \frac{I_k}{\sum I_k}, \tag{1.2}$$

where $I_k = \sigma(\hat{y} - \hat{y_k})$. $\sigma(\hat{y} - \hat{y_k})$ is the variance of the difference between the original model output $\hat{y}$ and the model output $\hat{y_k}$ when the k-input variable was held at its constant level. There are many possibilities with regard to which constant level to choose. It is possible to choose several levels and then to observe the sensitivity of model outputs varying for example on minimum, median and maximum levels. Our sensitivity measure (relative impact) was based on the median level. The primary reason comes from purely practical considerations – to compute our results fast enough as another weakness of the nonlinear techniques lies in the larger requirement of computational capacity. In general, this approach was chosen because of their relative simplicity for comparing all techniques to each other and to be able to interpret them too. The contribution of variables in neural network models has already been studied and Gevrey et al. (2003) produced a review and comparison of these methods.

1.4 Results

1.4.1 Annual response (MERRA)

Figure 1.1a, d, g, j shows the annually averaged solar signal in the zonal means of temperature, zonal wind, geopotential height and ozone mixing ratio. The signal is expressed as the average difference between the solar maxima and minima in

the period 1979–2013, i.e. normalised by 126.6 solar radio flux units. Statistically significant responses detected by the linear regression in the temperature series (see Fig. 1.1a) are positive and are located around the Equator in the lower stratosphere with values of about 0.5 K. The temperature response increases to 1 K in the upper stratosphere at the Equator and up to 2 K at the poles. The significant solar signal anomalies are more variable around the stratopause and not limited to the equatorial regions. Hemispheric asymmetry of the statistical significance can be observed in the lower mesosphere.

From a relative impact point of view (in Fig. 1.2a–c marked as RI), it is difficult to detect a signal with an impact larger than 20 % in the lower stratosphere where the volcanic and QBO impacts dominate. In the upper layers (where the solar signal expressed by the regression coefficient is continuous across the Equator) we have detected relatively isolated signals (over 20 %) around $\pm 15^{\circ}$ using the relative impact method. The hemispheric asymmetry also manifests in the relative impact field, especially in the SVR field in the mesosphere.

The annually averaged solar signal in the zonal mean of zonal wind (Figs. 1.1d and 1.2d–f) dominates around the stratopause as an enhanced subtropical westerly jet. The zonal wind variability due to the SC corresponds to the temperature variability due to the change in the meridional temperature gradient and via the thermal wind equation. The largest positive anomaly in the Northern Hemisphere reaches $4\,\mathrm{m\,s^{-1}}$ around 60 km (Fig. 1.1d). In the Southern Hemisphere, the anomaly is smaller and not statistically significant. There is a significant negative signal in the southern polar region. The negative anomalies correspond to a weakening of the westerlies or an amplification of the easterlies. The relative impact of the SC is similarly located zonally even for both nonlinear techniques (Fig. 1.2d–f). The equatorial region across all the stratospheric layers is dominantly influenced by the QBO (expressed by all three QBO regressors) and for this reason the solar impact is minimised around the Equator.

The pattern of the solar response in geopotential height (Figs. 1.1g and 1.2g–i) shows positive values in the upper stratosphere and lower mesosphere. This is also consistent with the zonal wind field through thermal wind balance. In the geopotential field, the SC influences the most extensive area among all regressors. The impact area includes almost the whole mesosphere and the upper stratosphere.

Figure 1.1j also shows the annual mean solar signal in the zonal mean of the ozone mixing ratio (expressed as a percent change per annual mean). By including an EESC regressor term in the regression model instead of a linear trend over the whole period (for a detailed description see the methodology Sect. 1.3), we tried to capture the ozone trend change around the year 1996. Another possibility was to use our model over two individual periods, e.g. 1979–1995 and 1996–2013, but the results were quantitatively similar. The main common feature of the MERRA solar ozone response in Fig. 1.1j with observational results is the positive ozone response in the lower stratosphere, ranging from a 1 to 3 percent change. In the equatorial upper stratosphere, no solar signal was detected that is comparable to that estimated from satellite measurement (Soukharev and Hood, 2006). By the relative impact method (Fig. 1.2j–l), we have obtained results comparable with linear regression coefficients, but especially around the stratopause the impact suggested by nonlinear techniques does not reach the values achieved by linear

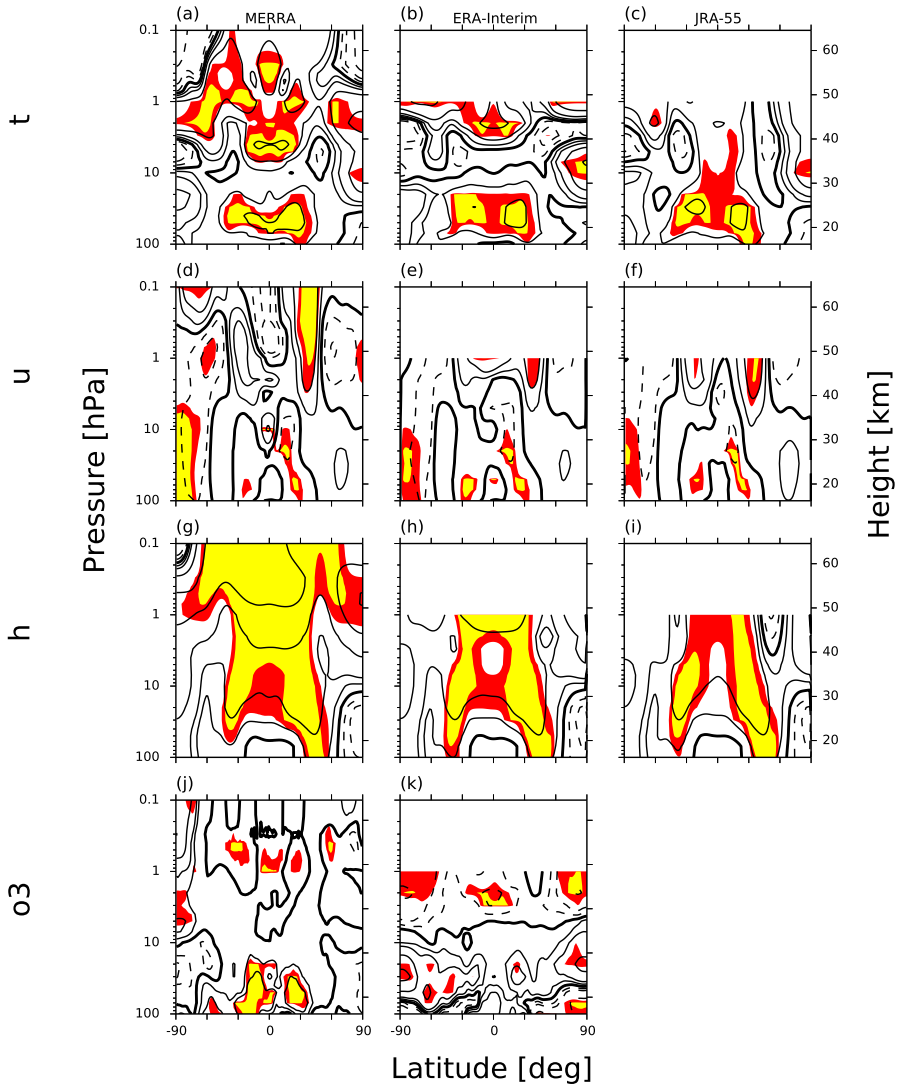

Figure 1.1: The annually averaged response of the solar signal in the MERRA, ERA-Interim and JRA-55 zonal-mean temperature t **(a–c)**, unit: K, contour levels: 0, ±0.25, ±0.5, ±1, ±2, ±5, ±10, ±15, ±30; zonal wind u **(d–f)**, unit: $\mathrm{m\,s^{-1}}$, contour levels: 0, ±1, ±2, ±5, ±10, ±15, ±30; geopotential height h **(g–i)**, unit: gpm, contour levels: 0, ±10, ±20, ±50, ±100, ±150; and ozone mixing ratio $o3$ **(j–k)**, unit: percentage change per annual mean, contour levels: 0, ±1, ±2, ±5, ±10. The response is expressed as a regression coefficient RC (corresponding units per $S_{\max}$ minus $S_{\min}$). The statistical significance of the scalar fields was computed by a t test. Red and yellow areas indicate p values < 0.05 and 0.01.

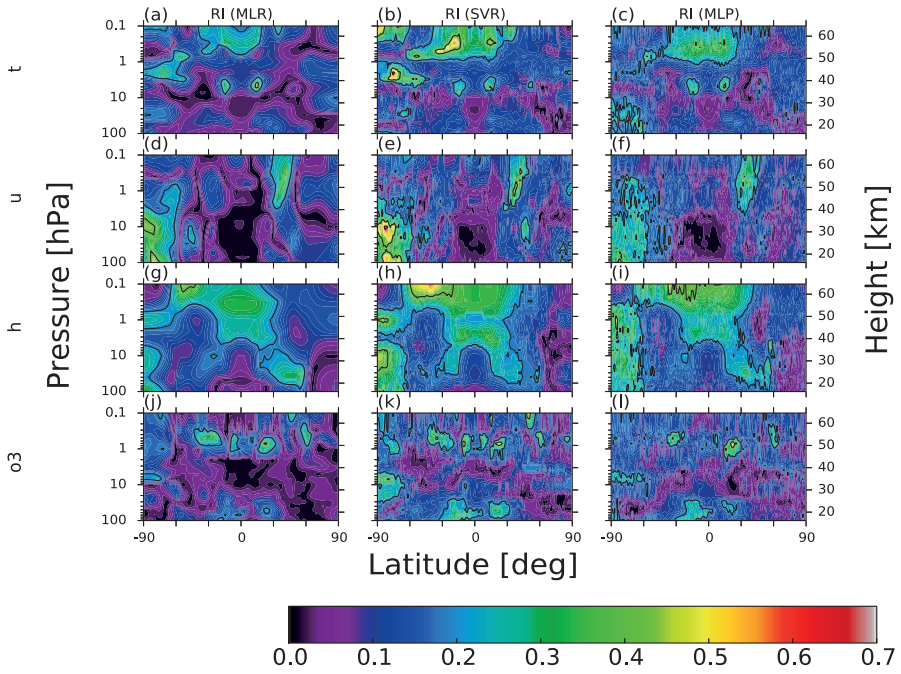

Figure 1.2: The annually averaged response of the solar signal in the MERRA zonal-mean temperature t **(a–c)**, unit: K; zonal wind u **(d–f)**, unit: $\mathrm{m\,s^{-1}}$; geopotential height h **(g–i)**, unit: gpm; and ozone mixing ratio $o3$ **(j–l)**, unit: percentage change per annual mean. The response is expressed as a relative impact RI approach. The relative impact was modelled by MLR, SVR and MLP techniques. The black contour levels in the RI plots are 0.2, 0.4, 0.8 and 1.0.

regression.

Annual response – comparison with JRA-55, ERA-Interim

Comparison of the results for the MERRA, ERA-Interim and JRA-55 temperature, zonal wind and geopotential height shows that the annual responses to the solar signal are in qualitative agreement (compare individual plots in Fig. 1.1). The zonal wind and geopotential response seem to be consistent in all presented methods and data sets. The largest discrepancies can be seen in the upper stratosphere and especially in the temperature field (the first row in these figures). The upper stratospheric equatorial anomaly was not detected by any of the regression techniques in the case of the JRA-55 reanalysis although the JRA-25 showed a statistically significant signal with structure and amplitude of 1–1.25 K comparable with ERA-Interim in the equatorial stratopause (Mitchell et al., 2015b). Although the anomaly in the MERRA temperature in Fig. 1.1a in the upper stratosphere is comparable to that in the ERA Interim temperature in Fig. 1.1b, the former signal is situated lower down at around 4 hPa (see also Mitchell et al., 2015b).

However, upper stratospheric temperature response could be less than accurate due to the existence of discontinuities in 1979, 1985 and 1998 (McLandress et al., 2014) coinciding with major changes in instrumentation or analysis procedure. Therefore, the temperature response to solar variation may be influenced by these discontinuities in the upper stratosphere. The revised analysis with the adjustments of ERA Interim temperature data from McLandress et al.

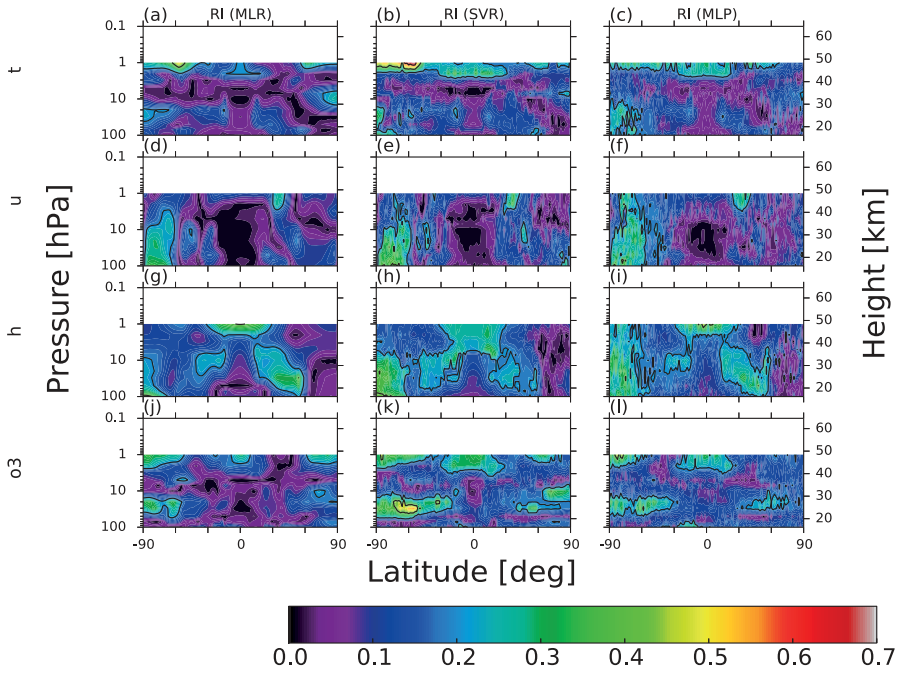

Figure 1.3: The annually averaged response of the solar signal in the ERA-Interim zonal-mean temperature t **(a–c)**, unit: K; zonal wind u **(d–f)**, unit: $\mathrm{m\,s^{-1}}$; geopotential height h **(g–i)**, unit: gpm; and ozone mixing ratio $o3$ **(j–l)**, unit: percentage change per annual mean. The response is expressed as a relative impact RI approach. The relative impact was modelled by MLR, SVR and MLP techniques. The black contour levels in the RI plots are 0.2, 0.4, 0.8 and 1.0.

(2014) showed in comparison with the original analysis without any adjustment that the most pronounced differences are apparent in higher latitudes and especially in 1 hPa. The regression coefficients decreased by about 50 % when using the adjusted data set, but the differences are not statistically significant in terms of 95 % confidence interval. The difference in tropical latitudes is about $0.2\,\mathrm{K}/(S_{\max} - S_{\min})$. The trend regressor t from Eq. 1.1 reveals a large turnaround from positive trend to negative in the adjusted levels, i.e. 1, 2, 3 and 5 hPa. Other regressors do not reveal any remarkable difference. The results in Figs. 1.1b, e, h, k and 1.3 from the raw data set were kept in order to refer and discuss the accordance and differences between our results and results from Mitchell et al. (2015b), where no adjustments have been considered either.

The variability of the solar signal in the MERRA stratospheric ozone series was compared with the ERA-Interim results. The analysis points to large differences in the ozone response to the SC between the reanalyses and in comparison with satellite measurements by Soukharev and Hood (2006). In comparison with the satellite measurements, no relevant solar signal was detected in the upper stratosphere in the MERRA series. The signal seems to be shifted above the stratopause (confirmed by all techniques, shown in Figs. 1.2 and 1.3j–l). Regarding the ERA-Interim, there is a statistically significant ozone response to the SC in the upper stratosphere, but it is negative in sign, with values reaching up to 2 % above the Equator and up to 5 % in the polar regions of both hemispheres. However, a negative ozone and a positive temperature response in the upper stratosphere to a positive UV flux change from solar minimum to maximum is not

physically reasonable. It must reflect an artifact of the assimilation model scheme and/or internal variability of the model rather than an effect of solar forcing (for more details about ozone as a prognostic variable in ERA-Interim, see Dee et al., 2011a). There is a clear inverse correlation between the ERA-Interim temperature response in Fig. 1.1b and the ozone response in Fig. 1.1k. This does probably imply that the temperature response is producing the negative ozone response in the assimilation model. However, it is not physically reasonable because both the ozone and the temperature in the upper stratosphere respond positively to an increase in solar UV (e.g. Hood et al., 2015). In the case of MERRA, while SBUV ozone profiles are assimilated with SC passed to the forecast model (as the ozone analysis tendency contribution), no SC was passed to the radiative part of the model. The same is also true for ERA-Interim and JRA-55 (see the descriptive table of the reanalysis product on SC in irradiance and ozone in Mitchell et al. (2015b). Despite the fact that the analysed ozone should contain a solar signal, the signal is not physically reasonable and is dominated by internal model variability in terms of dynamics and chemistry. Since the SBUV ozone profiles have very low vertical resolution, this may also affect the ozone response to the SC in the MERRA reanalysis. These facts should also be taken into account in case of monthly response discussion of particular variables in Sect. 4.2.

The lower stratospheric ozone response in the ERA-interim is not limited to the equatorial belt $\pm 30^\circ$ up to 20 hPa, as in the case of the MERRA reanalysis, and the statistical significance of this signal is rather reduced. The solar signal is detected higher and extends from the subtropical areas to the polar regions. The results suggest that the solar response in the MERRA series is more similar to the results from satellite measurements (Soukharev and Hood, 2006). Nevertheless, further comparison with independent data sets is needed to assess the data quality in detail.

Comparison of the linear and nonlinear approaches (MLR vs. SVR and MLP)

In this paper, we have applied and compared one linear (MLR) and two nonlinear attribution (SVR and MLP) techniques. The response of the studied variables to the solar signal and other forcings was studied using the sensitivity analysis approach in terms of averaged response deviation from the equilibrium represented by the original model output $\hat{y}$ (Blume and Matthes, 2012). This approach does not recognise a positive or negative response as the linear regression does. For this reason, the relative impact results are compared to the regression's coefficients. Using linear regression, it would be possible to assess the statistical significance of the regression's coefficients and a particular level of the relative impact since they are linearly proportional. A comparison between the linear and nonlinear approaches by the relative impact fields shows qualitative and in most regions also quantitative agreement. The most pronounced agreement is observed in the zonal wind (Figs. 1.2, 1.3 and 1.4d–f) and geopotential height fields (Figs. 1.2, 1.3 and 1.4g–i). On the other hand worse agreement is captured in the ozone and temperature field. In the temperature field the upper stratospheric solar signal reaches values over 20 %, some individual signals in the Southern Hemisphere even reach 40 %. However, using the relative impact approach, the lower stratospheric solar signal in the temperature field (which is well established by the

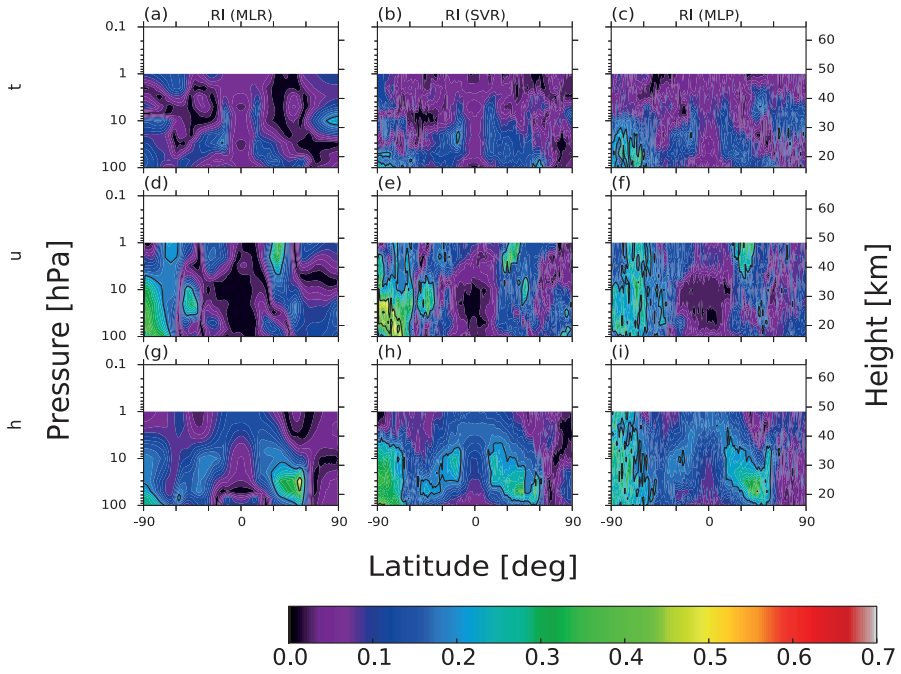

Figure 1.4: The annually averaged response of the solar signal in the JRA-55 zonal-mean temperature t **(a–c)**, unit: K; zonal wind u **(d–f)**, unit: $\mathrm{m\,s^{-1}}$; geopotential height h **(g–i)**, unit: gpm; and ozone mixing ratio $o3$ **(j–l)**, unit: percentage change per annual mean. The response is expressed as a relative impact RI approach. The relative impact was modelled by MLR, SVR and MLP techniques. The black contour levels in the RI plots are 0.2, 0.4, 0.8 and 1.0.

regression coefficient) does not even reach 20 % because of the dominance of the QBO and volcanic effects. These facts emphasise that nonlinear techniques contribute to the robustness of attribution analysis since the linear regression results were plausibly confirmed by the SVR and MLP techniques.

In conclusion, the comparison of various statistical approaches (MLR, SVR and MLP) should actually contribute to the robustness of the attribution analysis including the statistically assessed uncertainties. These uncertainties could partially stem from the fact that the SVR and neural network techniques are dependent on an optimal model setting which is based on a rigorous cross-validation process, which places a high demand on computing time.

The major differences between the techniques can be seen in how much of the temporal variability of the original time series is explained, i.e. in the coefficient of determination. For instance, the differences of the explained variance reach up to 10 % between linear and nonlinear techniques, although the zonal structure of the coefficient of determination is almost the same. To conclude, nonlinear techniques show an ability to simulate the middle atmosphere variability with a higher accuracy than cross-validated linear regression.

1.4.2 Monthly response (MERRA)

As was pointed out by Frame and Gray (2010), it is necessary to examine the solar signal in individual months because of a solar impact on polar-night jet oscillation (Kuroda and Kodera, 2001). For example, the amplitude of the lower stratospheric solar signal in the northern polar latitudes in February exceeds the

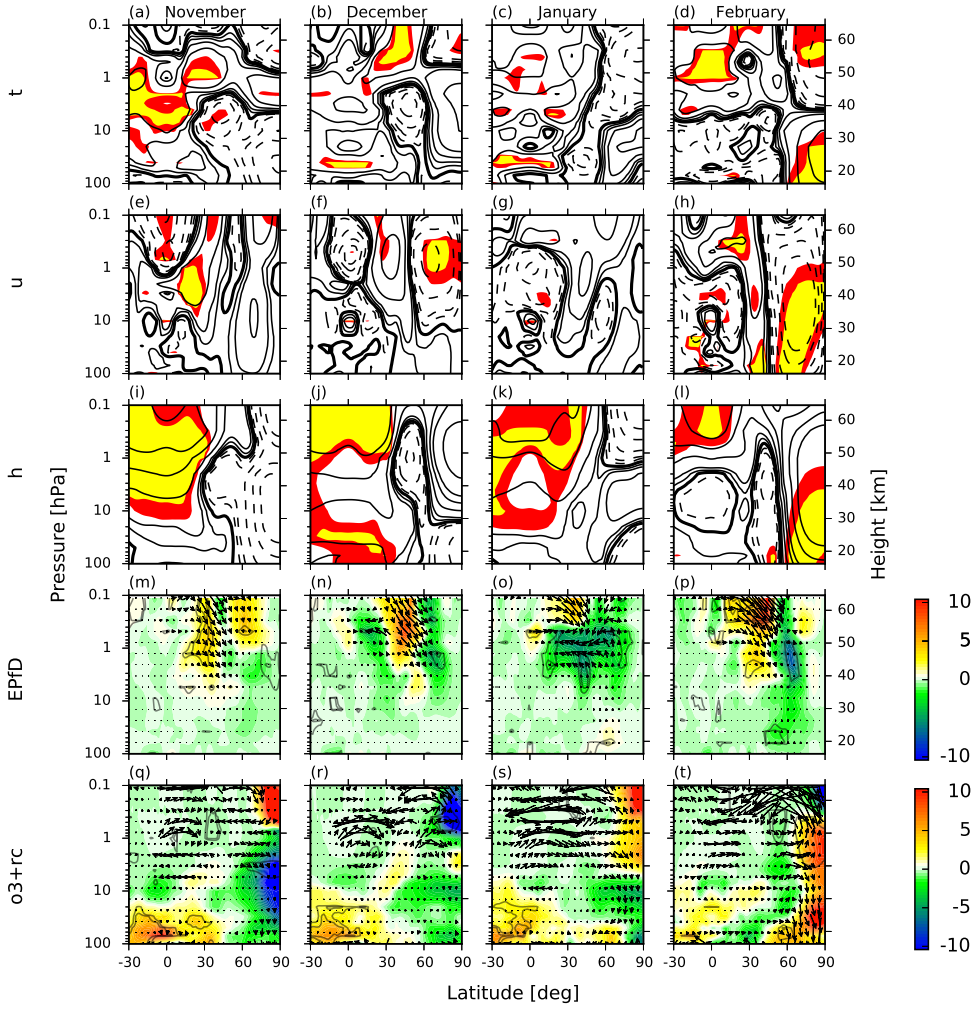

Figure 1.5: The monthly averaged response of the solar signal in the MERRA zonal-mean temperature t **(a–d)**, unit: K, contour levels: 0, ±0.25, ±0.5, ±1, ±2, ±5, ±10, ±15, ±30; zonal wind u **(e–h)**, unit: $\mathrm{m\,s^{-1}}$, contour levels: 0, ±1, ±2, ±5, ±10, ±15, ±30; geopotential height h (j–l), unit: gpm, contour levels: 0, ±10, ±20, ±50, ±100, ±150, ±300; EP flux divergence EPfD **(m–p)**, unit: $\mathrm{m\,s^{-1}\,day^{-1}}$; together with EP flux vectors scaled by the inverse of the pressure, unit: $\mathrm{kg\,s^{-2}}$; and ozone mixing ratio, unit: percentage change per monthly mean; with residual circulation $o3 + \mathrm{rc}$ **(q–t)**, units: $\mathrm{m\,s^{-1}}$; $-10^{-3}\,\mathrm{Pa\,s^{-1}}$ during northern hemispheric winter. The response is expressed as a regression coefficient (corresponding units per $S_{\max}$ minus $S_{\min}$). The statistical significance of the scalar fields was computed by a t test. Red and yellow areas in Panels **(a–l)** and grey contours in Panels **(m–t)** indicate p values of < 0.05 and 0.01 respectively.

annual response since the SC influence on vortex stability is most pronounced in February. Besides the radiative influences of the SC, we discuss the dynamical response throughout the polar winter (Kodera and Kuroda, 2002).

Statistically significant upper stratospheric equatorial anomalies in the temperature series (winter months in Figs. 1.5 and 1.6a–d) are expressed in almost all months. Their amplitude and statistical significance vary throughout the year. The variation between the solar maxima and minima could be up to 1 K in some months. Outside the equatorial regions, the fluctuation could reach several Kelvin. The lower stratospheric equatorial anomaly strengthens during winter. This could be an indication of dynamical changes, i.e. alteration of the residual circulation between the equatorial and polar regions (for details, please see Sect. 1.5). Aside from the radiative forcing by direct or ozone heating, other factors are linked to the anomalies in the upper levels of the middle atmosphere (Haigh, 1994; Gray et al., 2009). It is necessary to take into consideration the dynamical coupling with the mesosphere through changes of the residual circulation (see the dynamical effects discussion below). That can be illustrated by the positive anomaly around the stratopause in February (up to 4 K around 0.5 hPa). This anomaly extends further down and, together with spring radiative forcing, affects the stability of the equatorial stratopause. Hemispheric asymmetry in the temperature response above the stratopause probably originates from the hemispheric differences, i.e. different wave activity (Kuroda and Kodera, 2001). These statistically significant and positive temperature anomalies across the subtropical stratopause begin to descend and move to higher latitudes in the beginning of the northern winter. The anomalies manifest fully in February in the region between 60 and 90° N and reach tropospheric levels – contrary to the results for the Southern Hemisphere (see Fig. 10 in Mitchell et al., 2015b). The southern hemispheric temperature anomaly is persistent above the stratopause and the SC influence on the vortex stability differs from those in the Northern Hemisphere.

The above described monthly anomalies of temperature correspond to the zonal wind anomalies throughout the year (Figs. 1.5 and 1.6e–h). The strengthening of the subtropical jets around the stratopause is most apparent during the winter in both hemispheres. This positive zonal wind anomaly gradually descends and moves poleward, similar to the Frame and Gray (2010) analysis based on ERA-40 data. In February, the intensive stratospheric warming and mesospheric cooling is associated with a more pronounced transition from winter to summer circulation attributed to the SC (in relative impact methodology up to 30 %). However, GCMs have not yet successfully simulated the strong polar warming in February (e.g. Schmidt et al., 2010; Mitchell et al., 2015c). Due to the short (35-year) time series, it is possible that this pattern is not really solar in origin but is instead a consequence of internal climate variability or aliasing from the effects of the two major volcanic eruptions aligned to solar maximum periods.

In the Southern Hemisphere, this poleward motion of the positive zonal wind anomaly halts approximately at 60° S. For example, in August, we can observe a well-marked latitudinal zonal wind gradient (Fig. 1.6h). Positive anomalies in the geopotential height field correspond to the easterly zonal wind anomalies. The polar circulation reversal is associated with intrusion of ozone from the lower latitudes, as is apparent e.g. in August in the Southern Hemisphere and in February in the Northern Hemisphere (last rows of Figs. 1.5 and 1.6).

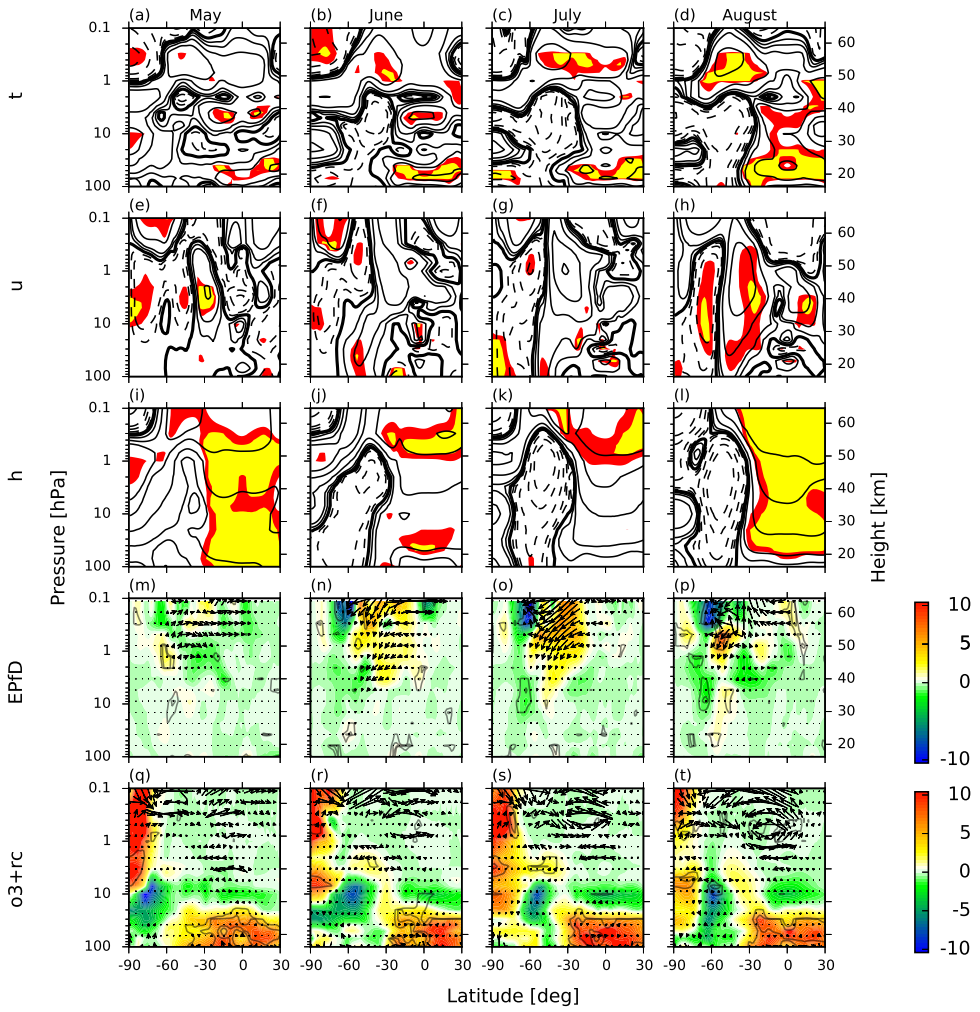

Figure 1.6: The monthly averaged response of the solar signal in the MERRA zonal-mean temperature t **(a–d)**; unit: K; contour levels: 0, ±0.25, ±0.5, ±1, ±2, ±5, ±10, ±15, ±30; zonal wind u **(e–h)**, unit: $\mathrm{m\,s^{-1}}$; contour levels: 0, ±1, ±2, ±5, ±10, ±15, ±30; geopotential height h **(j–l)**; unit: gpm; contour levels: 0, ±10, ±20, ±50, ±100, ±150, ±300; EP flux divergence EPfD **(m–p)**, unit: $\mathrm{m\,s^{-1}\,day^{-1}}$; together with EP flux vectors scaled by the inverse of the pressure; unit: $\mathrm{kg\,s^{-2}}$; and ozone mixing ratio, unit: percentage change per monthly mean; with residual circulation $o3{+}\,\mathrm{rc}$ **(q–t)**; units: $\mathrm{m\,s^{-1}}$, $-10^{-3}\,\mathrm{Pa\,s^{-1}}$ during southern hemispheric winter. The response is expressed as a regression coefficient (corresponding units per $S_{\max}$ minus $S_{\min}$). The statistical significance of the scalar fields was computed by a t test. Red and yellow areas in Panels **(a–l)** and grey contours in Panels **(m–t)** indicate p values of < 0.05 and 0.01 respectively.

When comparing the results from the MERRA and ERA-40 series studied by Frame and Gray (2010), distinct differences were found (Fig. 1.5e, f) in the equatorial region of the lower mesosphere in October and November. While in the MERRA reanalysis we have detected an easterly anomaly above 1 hPa in both months (only November shown), a westerly anomaly was identified in the ERA-40 series. Further distinct differences in the zonal mean temperature and zonal wind anomalies were not found.

1.5 Dynamical effects discussion

In this section, we discuss the dynamical impact of the SC and its influence on middle atmospheric winter conditions. Linear regression was applied to the EP diagnostics. Kodera and Kuroda (2002) suggested that the solar signal produced in the upper stratosphere region is transmitted to the lower stratosphere through the modulation of the internal mode of variation in the polar-night jet and through a change in the Brewer–Dobson circulation (prominent in the equatorial region in the lower stratosphere). In our analysis, we discussed the evolution of the winter circulation with an emphasis on the vortex itself rather than the behaviour of the jets. Furthermore, we try to describe the possible processes leading to the observed differences in the quantities of state between the solar maximum and minimum period. Because the superposition principle only holds for linear processes, it is impossible to deduce the dynamics merely from the fields of differences. As noted by Kodera and Kuroda (2002), the dynamical response of the winter stratosphere includes highly nonlinear processes, e.g. wave–mean flow interactions. Thus, both the anomaly and the total fields, including climatology, must be taken into account.

We start the analysis of solar maximum dynamics with the period of the northern hemispheric winter circulation formation. The anomalies of the ozone, temperature, geopotential in the lower stratosphere only and Eliassen–Palm flux divergence mostly in the upper stratosphere support the hypothesis of weaker BDC during the solar maximum due to the less intensive wave pumping. This is possible through the "downward control" principle when modification of wave–mean flow interaction in the upper levels governs changes in residual circulation below (Haynes et al., 1991). The finding about weaker BDC during the solar maximum is consistent with previous studies (Kodera and Kuroda, 2002; Matthes et al., 2006). The causality is unclear, but the effect is visible in both branches of BDC as is illustrated by Fig. 1.5 and summarised schematically in Fig. 1.7.

During the early Northern Hemisphere (NH) winter (including November) when westerlies develop in the stratosphere, we can observe a deeper polar vortex and consequent stronger westerly winds both inside and outside the vortex. However, only the westerly anomaly outside the polar region and around 30°N from 10 hPa to the lower mesosphere is statistically significant (see the evolution of zonal wind anomalies in Fig. 1.5e–h). The slightly different wind field has a direct influence on the vertical propagation of planetary waves. From the Eliassen–Palm flux anomalies and climatology we can see that the waves propagate vertically with increasing poleward instead of equatorward meridional direction with height. This is then reflected in the EP flux divergence field, where the region of maximal convergence is shifted poleward and the anomalous convergence region emerges

inside the vortex above approximately 50 hPa (Fig. 1.5m–p).

The poleward shift of the maximum convergence area further contributes to the reduced BDC. This is again confirmed by the temperature and ozone anomalies. The anomalous convergence inside the vortex induces anomalous residual circulation, the manifestation of which is clearly seen in the quadrupole-like temperature structure (positive and negative anomalies are depicted schematically in Fig. 1.7 using red and blue boxes respectively). This pattern emerges in November and even more clearly in December. In December, the induced residual circulation leads to an intrusion of the ozone-rich air into the vortex at about the 1 hPa level (Fig. 1.5r). The inhomogeneity in the vertical structure of the vortex is then also pronounced in the geopotential height differences. This corresponds to the temperature analysis in the sense that above and in the region of the colder anomaly there is a negative geopotential anomaly and vice versa. The geopotential height difference has a direct influence on the zonal wind field (via the thermal wind balance). The result is a deceleration of the upper vortex parts and consequent broadening of the upper parts (due to the conservation of angular momentum).

Considering the zonal wind field, the vortex enters January approximately with its average climatological extent. The wind speeds in its upper parts are slightly higher. This is because of the smaller geopotential values corresponding to the negative temperature anomalies above approximately 1 hPa. This probably results from the absence of adiabatic heating due to the suppressed BDC, although the differences in the quantities of state (temperature and geopotential height) are small and insignificant (see the temperature anomalies in Fig. 1.5c). It is important to note that these differences change sign around an altitude of 40 km inside the vortex further accentuating the vertical inhomogeneity of the vortex. This might start balancing processes inside the vortex, which is confirmed by analysis of the dynamical quantities, i.e. EP flux and its divergence (Fig. 1.5o).

Significant anomalies of the EP flux indicate anomalous vertical wave propagation resulting in the strong anomalous EP flux convergence being significantly pronounced in a horizontally broad region and confined to upper levels (convergence (negative values) drawn by green or blue shades in Fig. 1.5m–p). This leads to the induction of an anomalous residual circulation starting to gain intensity in January. The situation then results in the disruption of the polar vortex visible in significant anomalies in the quantities of state in February – in contrast to January. Further strong mixing of air is suggested by the ozone fields. The quadrupole-like structure of the temperature is visible across the whole NH middle atmosphere in February (indicated in the lower diagram of Fig. 1.7), especially in the higher latitudes. This is very significant and well pronounced by the stratospheric warming and mesospheric cooling.

The hemispheric asymmetry of the SC influence can be especially documented in winter conditions, as was already suggested in Sect. 1.4.2. Since the positive zonal wind anomaly halts at approximately 60° S and intensifies over $10\,\mathrm{m\,s^{-1}}$, one would expect the poleward deflection of the planetary wave propagation to be according to NH winter mechanisms discussed above. This is actually observed from June to August when the highest negative anomalies of the latitudinal component of EP flux are located in the upper stratosphere and in the lower me-

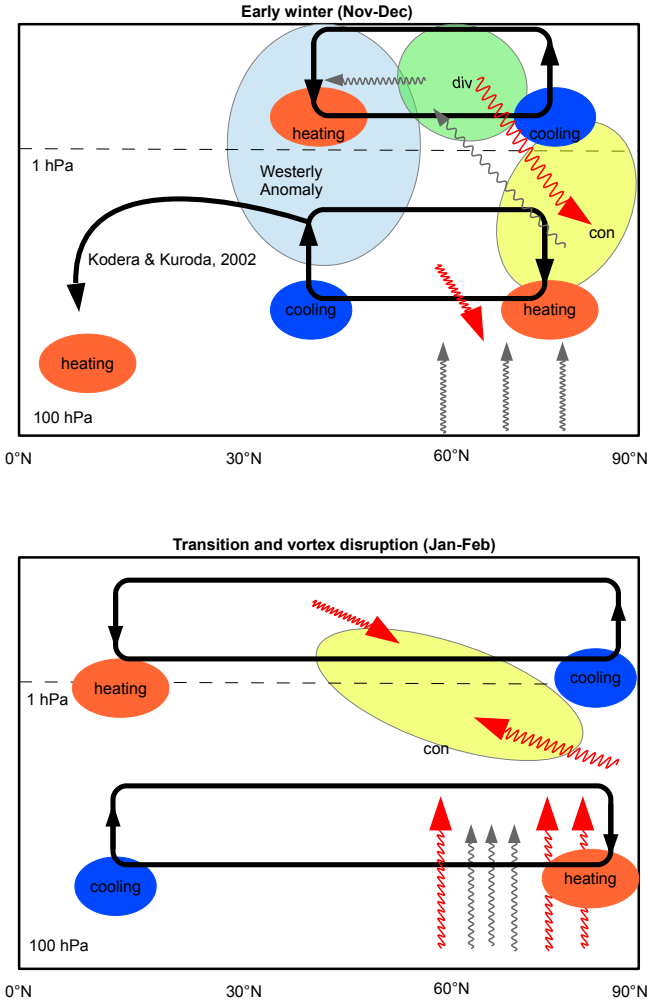

Figure 1.7: Solar cycle modulation of the winter circulation: schema of the related mechanisms. The upper and lower figure show early and later winter respectively. The heating and cooling anomalies are drawn with red and blue boxes. The EP flux divergence and convergence are drawn with green and yellow boxes. The wave propagation anomaly is expressed as a wavy red arrow in contrast to the climatological average drawn by a wavy grey arrow. The induced residual circulation according to the quasi-geostrophic approximation is highlighted by the bold black lines.

sosphere (Fig. 1.6m–p). The anomalous divergence of EP flux develops around the stratopause between 30 and 60° S. Like the hypothetical mechanism of weaker BDC described above, we can observe less wave pumping in the stratosphere and consequently less upwelling in the equatorial region. In line with that, we can see in the lower stratosphere of equatorial region (Figs. 1.5b and 1.6b) a more pronounced temperature response in August (above 1 K) than in December (around 0.5 K) as already mentioned in previous observational (van Loon and Labitzke, 2000) or reanalysis (Mitchell et al., 2015b) studies. Although this can point to a weaker BDC, the residual circulation (Fig. 1.6q–t) as a proxy for BDC (Butchart, 2014) does not reveal this signature. Hypothetically, this could be due to a higher role of unresolved wave processes in reanalysis (small-scale gravity waves) or due to the worse performance of residual circulation as a proxy for the large-scale transport in SH (e.g. larger departure from steady waves approximation comparing to NH), or because of the other processes than BDC leading to the temperature anomaly, e.g. aliasing with volcanic signal.

Overall, the lower stratospheric temperature anomaly is more coherent for the SH winter than for the NH winter, where the solar signal is not so apparent or statistically significant in particular months and reanalysis data sets.

1.6 Conclusions

We have analysed the changes in air temperature, ozone and circulation characteristics driven by the variability of the 11-year solar cycle's influence on the stratosphere and lower mesosphere. Attribution analysis was performed on the three reanalysed data sets, MERRA, ERA-Interim and JRA-55, and aimed to compare how these types of data sets resolve the solar variability throughout the levels where the "top-down" mechanism is assumed. Furthermore, the results that originated in linear attribution using MLR were compared with other relevant attribution studies and supported by nonlinear attribution analysis using SVR and MLP techniques.

The nonlinear approach to attribution analysis, represented by the application of the SVR and MLP, largely confirmed the solar response computed by linear regression. Consequently, these results can be considered quite robust regarding the statistical modelling of the solar variability in the middle atmosphere. This finding indicates that linear regression is a sufficient technique to resolve the basic shape of the solar signal through the middle atmosphere. However, some uncertainties could partially stem from the fact that the SVR and MLP techniques are highly dependent on an optimal model setting that requires a rigorous cross-validation process (which places a high demand on computing time). As a benefit, nonlinear techniques show an ability to simulate the middle atmosphere variability with higher accuracy than linear regression.

The solar signal extracted from the temperature field from MERRA and ERA-Interim reanalysis using linear regression has the amplitudes around 1 and 0.5 K, in the upper stratospheric and in the lower stratospheric equatorial region respectively. However, the peak amplitudes of the temperature response in the equatorial upper stratosphere occur at different levels (about 4 and 2 hPa respectively). These signals, statistically significant at a p value < 0.01, are in qualitative agreement with previous attribution studies (e.g. Frame and Gray, 2010;

Mitchell et al., 2015b). A statistically significant signal was only observed in the lower part of the stratosphere in the JRA-55 reanalysis, however with similar amplitudes as the other data sets.

Similar to the temperature response, the double-peaked solar response in ozone was detected in satellite measurements (e.g. Soukharev and Hood, 2006), although concerns were expressed about the physical mechanism of the lower stratospheric response (e.g. Austin et al., 2008). However, the exact position and amplitude of both ozone anomalies remain a point of disagreement between models and observations. The results of our attribution analysis point to large differences in the upper stratospheric ozone response to the SC in comparison with the studies mentioned above and even between reanalyses themselves. The upper stratospheric ozone anomaly reaches 2 % in the SBUV(/2) satellite measurements (e.g. Soukharev and Hood, 2006, Fig. 5) which were assimilated as the only source of ozone profiles in MERRA reanalysis. This fact is remarkable since the same signal was not detected in the upper stratosphere in the MERRA results. However, the solar signal in the ozone field seems to be shifted above the stratopause where similar and statistically significant solar variability was attributed. Concerning the solar signal in the ERA-Interim, there is a negative ozone response via a regression coefficient in the upper stratosphere, although the solar variability expressed as relative impact appears to be in agreement with satellite measurements. The negative ozone response in the tropical upper stratosphere is not consistent with physical expectations for a nominal positive change in solar UV irradiance (e.g. Hood et al., 2015).

Furthermore, the lower stratospheric solar response in the ERA-Interim's ozone around the Equator is reduced in this data set and shifted to higher latitudes. Another difference was detected in the monthly response of the zonal wind in October and November in the equatorial region of the lower mesosphere between the results for the MERRA series and ERA-40 data studied by Frame and Gray (2010). While in the MERRA reanalysis we have detected an easterly anomaly, a westerly anomaly was identified in the ERA-40 series.

A similar problem with the correct resolving of the double-peaked ozone anomaly was registered in the study of Dhomse et al. (2011) which investigated the solar response in the tropical stratospheric ozone using a 3-D chemical transport model. The upper stratospheric solar signal observed in SBUV/SAGE and SAGE-based data could only be reproduced in model runs with unrealistic dynamics, i.e. with no inter-annual meteorological changes.

The reanalyses have proven to be extremely valuable scientific tools (Rienecker et al., 2011). On the other hand, they have to be used with caution, for example, due to the existence of large discontinuities occurring in 1979, 1985 and 1998 (McLandress et al., 2014) that translated into errors in the derived solar coefficients. Our revised analysis with the adjustments from McLandress et al. (2014) resulted in an $0.2\,\mathrm{K}/(S_{\max} - S_{\min})$ reduction in the temperature solar regression coefficients in tropical latitudes of the upper stratosphere.

In the dynamical effects discussion, we described the dynamical impact of the SC on middle atmospheric winter conditions. The relevant dynamical effects are summarised in schematic diagrams (Fig. 1.7). Both diagrams depict average conditions and anomalies induced by the SC. The first one summarises how equatorward wave propagation is influenced by the westerly anomaly around

the subtropical stratopause. The quadrupole-like temperature structure is explained by anomalous residual circulation in the higher latitudes together with the anomalous branch heading towards the equatorial region already hypothesised by Kodera and Kuroda (2002). The second diagram concludes the transition time to vortex disruption during February. Again, a very apparent quadrupole-like temperature structure is even more pronounced, especially in the polar region, and seems to be more extended to lower latitudes.

Fields of residual circulation and EP flux divergence in February are opposite to what would be expected from the suppressed BDC in the SC max. There is an enhanced downwelling in the polar and an enhanced upwelling in the equatorial region below 1 hPa. This suggests a need to diagnose the influence of SC on transport at least on a monthly scale because the changes in the underlying dynamics (compare the upper and lower diagrams in Fig. 1.7) would make the transport pathways more complicated. The negative zonal wind response in late northern winter may be caused by an increased likelihood of major stratospheric warmings later in the winter under solar maximum conditions when the polar vortex in early winter is stronger, on average, and therefore less susceptible to disruption (e.g. Gray et al., 2004). Since GCMs have not yet successfully simulated this pattern (e.g. Schmidt et al., 2010; Mitchell et al., 2015c) and due to the short (35-year) time series, it is possible that this pattern is not really solar in origin but is instead a consequence of internal climate variability or aliasing from effects of the two major volcanic eruptions aligned to solar maximum periods.

However, we can strongly assume that the dynamical effects are not zonally uniform, as is shown here using two-dimensional (2-D) EP diagnostics and TEM equations. Hence, it would be interesting to extend the discussion of dynamical effects for other relevant characteristics, for example, for the analysis of wave propagation and wave–mean flow interaction using the 3-D formulation (Kinoshita and Sato, 2013).

This paper is fully focused on the SC influence, i.e. on decadal changes in the stratosphere and lower mesosphere, although a huge number of results concerning other forcings was generated by attribution analysis. The QBO phenomenon in particular could be one of the points of future interest since the solar–QBO interaction and the modulation of the Holton–Tan relationship by the SC are regarded as highly challenging, especially in global climate simulations (Matthes et al., 2013).

2. On the aliasing of the solar cycle in the lower-stratospheric tropical temperature

2.1 Introduction

The influence of the 11-year solar cycle (SC) on reanalysis temperature data (Frame and Gray, 2010; Mitchell et al., 2015b) or ozone observations (Hood and Soukharev, 2012) has been well documented. The solar cycle is often attributed using multiple linear regression analysis. In the tropics, the response consists of statistically significant warming and ozone increases in the upper (∼1 hPa) and lower (∼50 hPa) stratosphere, but with a minimum between (∼10 hPa). Several transient CCM simulations have partially reproduced the observed double-peaked temperature and ozone responses (Egorova et al., 2004; Austin et al., 2008). However, there are concerns that the origin of the lower peak is due to potential aliasing of the solar cycle with El Niño Southern Oscillation (ENSO) events (Marsh and Garcia, 2007), or volcanic eruptions (Chiodo et al., 2014). Marsh et al. (2007) also demonstrated that the solar cycle response from time-slice simulations with fixed solar maximum or minimum forcings is very similar to the solar cycle response in transient simulations without a volcanic forcing and with variable sea surface temperature, for the period 1950–2003. However, for 1979–2003 the solar signal detected in transient simulations differs significantly from the signal simulated in time slice simulations with fixed solar maximum or minimum conditions. This difference already indicates a possible aliasing from using such a short (∼ 2 cycles long) record.

It has been hypothesized that the lower-stratospheric anomaly is caused by reduced upwelling at low latitudes, i.e. the Brewer-Dobson circulation (BDC) is weaker during solar maxima (Kodera and Kuroda, 2002; Hood and Soukharev, 2012). These mechanisms — thought to be driven by the UV-induced changes in the upper stratosphere propagating downward ("top-down" mechanism) or by the non-UV-induced changes generated near the surface propagating upward ("bottom-up" mechanism) (Gray et al., 2010) — are expected to be particularly pronounced during the boreal winter when wave forcing is most active. Muthers et al. (2016) found a weak positive relationship between the 11 year solar cycle and age of air (a descriptive variable of the transport time, related to the BDC) when using the coupled atmosphere-ocean-chemistry-climate model SOCOL-MPIOM. Furthermore, other processes, such as the Quasi-Biennial Oscillation (QBO), ENSO and volcanic eruptions, must also be taken into account.

While the influence of the QBO on the solar signal in this region has been discussed elsewhere (e.g. Lee and Smith, 2003; Smith and Matthes, 2008; Matthes et al., 2013), we focus here on variability in the tropical lower stratosphere (TLS) caused by ENSO and volcanic eruptions. Positive ENSO events (El Niño) cause a negative temperature anomaly at 50 hPa over the equator, whereas an opposite temperature response was detected in the case of volcanic eruptions (Mitchell et al., 2015b; Fujiwara et al., 2015).

It is important to point out that previous attribution studies differ in terms of regressors used, their time lag, and treatment of regression residuals. The choice of the applied regression can lead to different, even incorrect, interpretation of results. Two considerations should be made to properly attribute the signal through MLR. The first is to avoid the effect of autocorrelation of residuals, which could bias the variances of the ordinary least squares (OLS) estimates for the regression coefficients — the OLS estimates are still unbiased in the presence of residual autocorrelations, though inefficient (Thejll, 2005). The second is to account for, or eliminate possible aliasing (multicollinearity) of regressors. Both of these are addressed in our analysis.

Mitchell et al. (2015c) assessed the 11-year SC in CMIP5 historical simulations, reporting that the signal in TLS temperature depends on the length of the analysis period. They pointed out that the strongest solar signal is found in the 1979–2005 period, and acknowledged the possibility of aliasing effects. These have been already addressed by Marsh and Garcia (2007) and Chiodo et al. (2014) who suggested that the period covered by satellite measurements (1979–present) is insufficient for solar signal detection by MLR due to contamination by ENSO events and volcanic eruptions, respectively. Thus, identification of a period from which a robust solar signal could be detected, i.e. separated from other phenomena influencing the lower-stratospheric variability, is required. Furthermore, Chiodo et al. (2014) used CCM WACCMv3.5, which heavily overestimates the stratospheric warming after the Mt. Pinatubo by $\sim 3.5\,\mathrm{K}$). In fact, this overestimated warming may enhance aliasing effects. Therefore, different models not suffering this discrepancy should also be used.

The paper is arranged as follows. First, we introduce our model experiments using the SOCOL (SOlar Climate Ozone Links) CCM (Section 2.2.1), meteorological reanalysis and observational datasets used for model evaluation (Section 2.2.2) and methodology based on MLR (Section 2.3). Secondly, we validate the SOCOL CCM against observational and reanalysis records in terms of the temperature response to the SC and volcanic eruptions. By using CCM sensitivity simulations, we explain and quantify how the solar signal in the TLS was affected by volcanic eruptions and ENSO events during the past 50 years (Section 2.4.1). In Section 2.4.2, we show how the amplitude of the signal depends on the period and methodology applied in the regression analysis. Furthermore, we provide an elegant statistical explanation of the solar signal misattribution when using MLR, and then we reiterate that consideration of autoregressive (AR) components in MLR analysis is essential also that higher AR orders may be relevant for the lower stratosphere. Conclusions are presented in Section 2.5.

2.2 Data and models

2.2.1 Model simulations

To carry out the model sensitivity simulations we use version 3 of the SOCOL CCM (Stenke et al., 2013), which is composed of the general circulation model MA-ECHAM-5 (Manzini et al., 2006) and the chemistry part of the atmospheric chemistry transport model MEZON (Egorova et al., 2003). Our model experiments were performed with T42 horizontal resolution (grid cell sizes correspond

to approximately 2.8° × 2.8°) and 39 vertical levels between the Earth's surface and 0.01 hPa (∼80 km). The model setup is not able to simulate the QBO spontaneously, so equatorial stratospheric winds between 20°S and 20°N and from 90 hPa to 3 hPa have been relaxed towards observed wind (Giorgetta et al., 2006; Stenke et al., 2013).

The reference simulation (REF-C1) is part of the Chemistry-Climate Model Initiative (CCMI) activity (Eyring et al., 2014; Revell et al., 2015; Morgenstern et al., 2017a). REF-C1 was forced by boundary conditions specified from observations, i.e. observed sea surface temperatures (SST) and sea ice concentrations (SIC) (see Table 2.1), greenhouse gas concentrations, ozone depleting substances, tropospheric emissions, and volcanic and tropospheric aerosols. The Naval Research Laboratory Solar Spectral Irradiance (NRLSSI) model was used to calculate solar irradiance forcing (Lean et al., 2005), which was also used in previous CCMVal (CCMVal, 2010) and CMIP5 (Hood et al., 2015; Mitchell et al., 2015c) experiments. One such simulation (REF-C1) was performed with a 10-year spin-up period starting in 1950.

To investigate the role of volcanic eruptions or SST/SIC boundary conditions on the solar cycle signal, additional sensitivity simulations were performed, covering the period 1961–2009. REF-C1-q was performed to simulate volcanically *quiescent* conditions; its setup was identical to REF-C1 but without any forcing by volcanic aerosols (i.e. only background stratospheric aerosols from year 2000 were used for the entire simulation). However, REF-C1-q may still contain volcanic perturbations embedded in the prescribed, historical SST/SIC. In order to avoid volcanic, and additional SST/SIC impacts such as ENSO, on stratospheric variability, we performed another simulation, termed REF-C1-q-clim, using a monthly *climatology* of SST/SIC values from 1960 to 2009. REF-C1-q and REF-C1-q-clim consist of 3 transient ensemble runs with slightly different initial CO_2 concentrations during the first simulated month (about ±0.5%).

Furthermore, we investigate the influence of prescribed volcanic forcing on the temperature in the TLS region. Therefore additional sensitivity simulations were performed, covering the Mt. Pinatubo and Agung eruption periods using the new CMIP6 volcanic forcing (Luo, 2016) instead of the original volcanic forcing used in the CCMI framework (Luo, 2013). All simulations are summarized in Table 2.1.

2.2.2 Datasets used for model evaluation

To validate our SOCOL simulations we use two reanalyses: MERRA2 (Koster et al., 2015) and JRA-55 (Ebita et al., 2011). The latter is used because it covers the whole simulated period (available from 1958 to present). Furthermore, we use merged satellite temperature measurements from the NOAA Stratospheric Sounding Unit (SSU) and Advanced Microwave Sounding Unit-A (AMSU-A) (Zou and Qian, 2016) for the period 1980–2009. SSU temperature time series are represented by its three channels whose weighting functions peak at pressures of approximately 14.6, 4.6, and 1.9 hPa (Chen et al., 2011). For the TLS validation, AMSU satellite temperature measurements (Mears and Wentz, 2009) are included (at a pressure level of approximately 83 hPa) together with radiosonde dataset HadAT2 (Thorne et al., 2005).

Table 2.1: Description of model simulations. Simulations correspond to the CCMI REF-C1 scenario (Morgenstern et al., 2017a); volcanically quiescent variants are denoted by "q"; simulations without historical variability in sea surface temperature and sea ice coverage (SST/SIC) are denoted by "clim", i.e. climatology.

Simulation	Simulated period	SST/SIC	Volcanic forcing	# of ens. members
REF-C1	1960–2009	Hadley record	$\surd$ (CCMI)	3
REF-C1-q	1961–2009	Hadley record	$\times$	3
REF-C1-q-clim	1961–2009	Hadley climatology wrt 1960–2009	$\times$	3
REF-C1-CMIP6aer (Mt. Agung)	1960–1965	Hadley record	$\surd$ (CMIP6)	3
REF-C1-CMIP6aer (Mt. Pinatubo)	1986–2005	Hadley record	$\surd$ (CMIP6)	5

2.3 Regression analysis

To detect variability and changes due to external climate factors, including the 11-year solar cycle, we have used an attribution method based on the MLR analysis applied by Kuchar et al. (2015). This regression model[1] is applied to a monthly deseasonalized time series Y, reconstructing it as a function of time t:

$$\begin{aligned} Y(t) &= \alpha + \beta\,\mathrm{SAD}(t) + \gamma\,\mathrm{F}_{10.7}(t) \\ &\quad +\delta_1\,\mathrm{QBO}_1(t) + \delta_2\,\mathrm{QBO}_2(t) + \epsilon\,\mathrm{ENSO}(t) \\ &\quad +\zeta\,\mathrm{TREND}(t) + e(t). \end{aligned} \tag{2.1}$$

The regression model uses predictors representing climate forming factors that have an impact on middle atmosphere conditions, i.e. the 10.7 cm radio flux as a solar proxy[2] ($F_{10.7}$), globally averaged aerosol surface area density at 54 hPa (SAD) for volcanic eruptions, the ENSO3.4 index representing ENSO variability, and two proxies for the Quasi-Biennial Oscillation (QBO). Values for SAD in Eq. (2.1) have been obtained from the CCMI data set of Luo (2013) (see also Arfeuille et al. (2013)). The ENSO3.4 index (averaged sea surface temperature anomaly in the region bounded by 5°N to 5°S, and from 170°W to 120°W) is extracted from the HadISST data set (Rayner et al., 2003), which was also used as the SST/SIC boundary condition for our simulations. REF-C1-q and REF-C1-q-clim were both evaluated without volcanic regressors and the latter without an ENSO regressor. After assessing the structure of the regression residuals, there is no indication of bias from the residuals resulting from the absence of an important missing regressor for our regression analysis setups.

The QBO proxies were extracted by principal component analysis (PCA) from the residuals of our regression model excluding QBO regressors and residual modeling following Frame and Gray (2010). The zonal mean of the model's zonal winds, between 10°S and 10°N and from 50 hPa to 10 hPa, is used as an input for extraction of QBO proxies.

The linear regression is based on estimating regression coefficients by least squares minimization. To avoid autocorrelation of residuals $e(t)$, an iterative algorithm was used to model residuals as a second-order autoregressive process (generally termed AR2). Statistical significance at 2σ confidence intervals computed by t-test is presented. We obtained similar results using a more robust bootstrap method based on 5000 samples using our regression model with AR2 to account for autocorrelation of residuals (not shown).

Furthermore, we also used MLR to derive the tropical temperature response to the eruptions of Mt. Agung, El Chichón and Mt. Pinatubo. The temperature response for each eruption was extracted as the difference between 12-month averaged $R(t)$ after each eruption and the 36-month averaged $R(t)$ before each eruption (following Fujiwara et al., 2015). $R(t)$ is the residual of our regression model 2.1 when volcanic regressors and residual modeling (AR2) were not used.

To facilitate the reproducibility of results within the solar-climate modeling community, where MLR is widely used, and to account for possible differences in

[1] Greek letters represent regression coefficients.

[2] The dataset was acquired from Dominion Radio Astrophysical Observatory (DRAO) in Penticton, Canada. Follow this link: `ftp://ftp.geolab.nrcan.gc.ca/data/solar_flux/monthly_averages/`

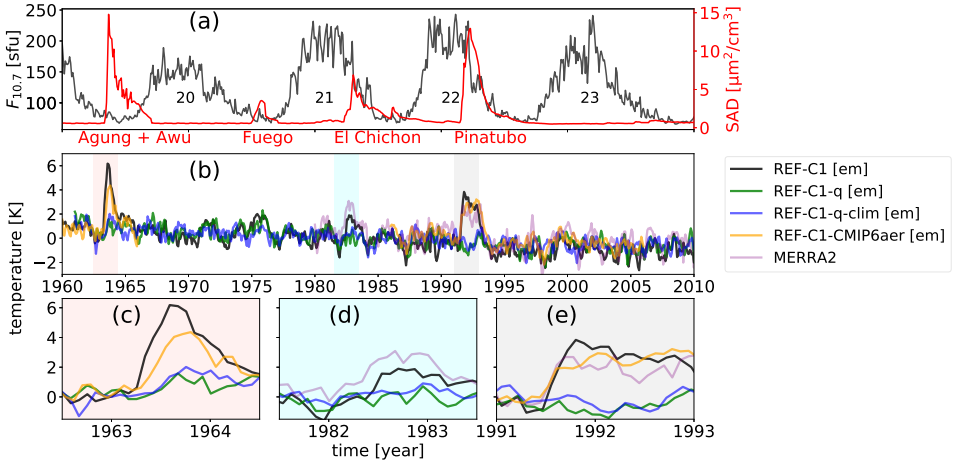

Figure 2.1: **(a)** Time series of 10.7 cm solar radio flux ($F_{10.7}$; black line) and globally averaged aerosol surface area density at 54 hPa (SAD; red line) from 1960 to 2009 used in CCMI simulations (Luo, 2013). **(b)** Deseasonalized tropical temperature time series at 50 hPa for REF-C1 and REF-C1-CMIP6aer (all forcings, black and orange line), REF-C1-q (quiescent, i.e. without volcanic forcing, green line), REF-C1-q-clim (quiescent and replacing SST/SIC interannual variability by climatological values, blue line) and MERRA2 reanalysis (purple). Temperature time series from **(b)** Mt. Agung, El Chichón and Mt. Pinatubo volcanic eruptions are enlarged in **(c)**, **(d)** and **(e)**, respectively.

regression approaches, we developed an MLR-based tool called *X-regression* (Kuchar, 2016). An accompanying Github repository has been created to document the methodological approach used in this paper and to accelerate future activities focused on solar cycle attribution and validation of climate models. This tool is based on the Python open-source software library *statsmodels* (Seabold and Perktold, 2010) coupled with *xarray* (Hoyer et al., 2016).

2.4 Results

To introduce the aliasing within the TLS, Figure 2.1a shows how two major volcanic eruptions, El Chichón in 1982 and Mt. Pinatubo in 1991, represented by time series of globally averaged SAD at 54 hPa, are aligned with the descending phase of solar maxima 21 and 22 represented by time series of 10.7 cm solar radio flux, respectively. Figure 2.1b provides a comparison of deseasonalized tropical temperature time series between SOCOL simulations and MERRA2 reanalysis at 50 hPa. The time series in Fig. 2.1b highlights three important source of variability: the QBO, the longterm stratospheric cooling trend from 1960 up to 2000, and several warming peaks associated with volcanic eruptions. It is also apparent that the REF-C1 simulation overestimates the tropical temperature response in the TLS to Mt. Pinatubo eruption as compared to MERRA2 reanalysis. This overestimation disappears in the REF-C1-CMIP6aer ensemble due to different gap-filling procedures used to compile the CCMI and CMIP6 stratospheric aerosol data sets when the lower stratosphere is too optically thick following the eruption for occultation instruments onboard satellites to measure (Revell et al., 2017) (see also enlarged Figs. 2.1c, d and e for Mt. Agung, El Chichón and Mt. Pinatubo volcanic eruptions, respectively).

2.4.1 Tropical temperature response to the SC

Figure 2.2a shows the modelled solar cycle maximum-to-minimum[3] zonally averaged temperature response between 25°S and 25°N using monthly mean averages compared with MERRA2 and SSU. In Fig. 2.2a the upper-stratospheric response of REF-C1 (black line) peaking at 1.5 hPa agrees well with MERRA2 (shading) and, in particular, SSU (red errorbars) estimates. A stronger signal in the reanalysis can be partly attributed to the existence of discontinuities in 1979, 1985 and 1998 as discussed by (McLandress et al., 2014), coinciding with major changes in instrumentation or reanalysis procedure, particularly at 5 hPa and above, and also seen in ERA-Interim (Dee et al., 2011a; Rienecker et al., 2011). Kuchar et al. (2015) stated that the difference between the temperature response to the SC of non-adjusted and adjusted ERA-Interim datasets is about 0.2 K in the upper tropical stratosphere. Another reason for the difference between model results, MERRA2 and SSU in the upper stratosphere may result from the use of the NRLSSI solar forcing (Lean et al., 2005) used in CCMI, which gives a smaller temperature response in comparison to other forcings (see Fig. 10 for SOCOL in Ermolli et al. (2013)). This is most likely related to the NRLSSI model's conservative SSI variability in the UV range in comparison with other SSI datasets. However, it is unlikely that using e.g. the SATIRE SSI forcing (Krivova et al., 2010; Yeo, K. L. et al., 2014), would change the temperature response so significantly (Ball et al., 2014a; Matthes et al., 2016). At ∼15 hPa, REF-C1 shows a similar response as SSU, and from 50 hPa downward REF-C1 is in good agreement with MERRA2 and AMSU. The double-peaked structure calculated using reanalysis datasets for the period starting in 1979 (e.g. Frame and Gray, 2010; Mitchell et al., 2015b), observational datasets (Randel et al., 2009; Hood and Soukharev, 2012) and also model transient simulations (e.g. Austin et al., 2008; Hood et al., 2015) is also found in the SOCOL reference simulation REF-C1 (black line in Fig. 2.2a). While the SC detected in SOCOL peaks between 20 and 30 hPa (see Table 2.2), the SC detected in MERRA2 peaks between 40 and 50 hPa. The origin of this systematic difference is likely a result of using the CCMI volcanic forcing and we discuss this further below.

In Figs. 2.2a and 2.2b we show how attributed solar and volcanic effects overlap in the TLS. Figure 2.2b shows the tropical temperature response to the eruptions of Mt. Agung, El Chichón and Mt. Pinatubo (following the procedure by Fujiwara et al., 2015, described in Section 2.3). This suggests that aerosol heating can either mimic the solar signal, thus enhancing its amplitude, or cancel out the solar signal, thus decreasing its amplitude in the TLS.

The REF-C1 results provide a reference for the following sensitivity tests with slightly different boundary conditions. To estimate the direct impact of volcanic eruptions on the extraction of the solar cycle signal from the SOCOL model, we perform the same ensemble set as before, but with only background stratospheric aerosols included (REF-C1-q; green line in Fig. 2.2a). Elimination of the volcanic aerosol in REF-C1-q leads to a weaker equatorial temperature response than in REF-C1 throughout the whole stratosphere and especially from 20 hPa downwards; below 30 hPa the signal is not statistically different from

[3]The signal is expressed as the average difference between the solar maxima and minima in the period 1979–2013, i.e. normalised by $F_{10.7} = 126.6$ solar flux units (sfu, see Fig. 2.1a).

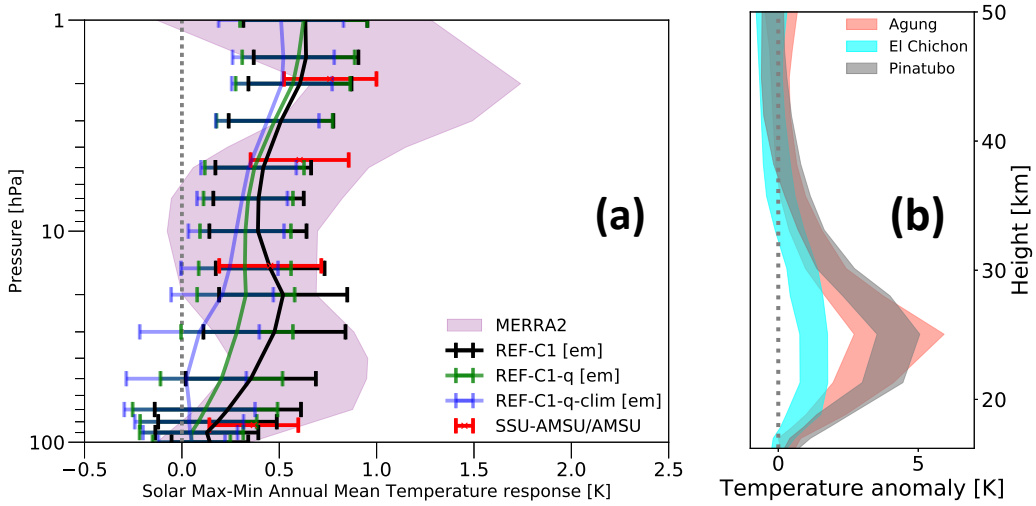

Figure 2.2: **(a)** Tropical (zonal mean between 25°S and 25°N) annual mean temperature response to solar variability, i.e. normalized regression coefficient γ from Eq. 2.1, over the period 1980–2009 in SOCOLv3 (ensemble mean (em) of REF-C1, REF-C1-q and REF-C1-q-clim), in comparison with MERRA2, SSU-AMSU and AMSU. The signal is expressed as the average difference between solar maxima and minima in the period 1979–2013. Horizontal bars and shaded area (MERRA2): 95% confidence interval of γ coefficient in Eq. 2.1 (determined with AR2). **(b)** Tropical temperature response to the eruptions of Mt. Agung (orange shading), El Chichón (cyan shading) and Mt. Pinatubo (gray shading) in REF-C1 simulation. Error bars represents 95% confidence intervals for the difference in the means.

zero. While the double-peaked structure in REF-C1-q is still apparent (a weak secondary maximum around 20 hPa), the lower-stratospheric temperature shows a reduced response to the 11-year SC. Given that the only difference between REF-C1 and REF-C1-q is that the latter has no volcanic aerosol forcing, the implication is that the temperature response to the solar forcing is overestimated (almost doubled near 50 hPa) due to the volcanic aliasing in the solar signal. This confirms the conclusion of Chiodo et al. (2014) who used WACCMv3.5 — a model different to SOCOL, but overestimating the warming after Mt. Pinatubo as well.

To completely eliminate any volcanic influence that may reach the stratosphere indirectly via a feedback response from the oceans, we performed a historical simulation similar to REF-C1-q, but with SST/SIC boundary conditions set to the climatology of the period, i.e. REF-C1-q-clim. The temperature response in the TLS attributed to solar forcing is further reduced in the REF-C1-q-clim simulation with climatological SST/SIC boundary conditions (blue line in Fig. 2.2a). The TLS temperature responses for all our simulations and MERRA2 regarding TLS is listed in Table 2.2.

The signal attributed to the SC is reduced by 44% and 50% at 50 and 70 hPa respectively when volcanoes are quiescent; switching off SST/SIC interannual variability leads to a 94% reduction of the mean SC signal at 50 hPa (0.36 K vs 0.02 K in Table 2). This highlights that SST/SIC interannual variability for simulating the secondary maximum in the TLS may be crucial. In addition to REF-C1-q, REF-C1-q-clim aims to avoid the possibility of volcanic signal artifacts being carried via SST/SIC in the HadISST data (Gray et al., 2013), or even other types of SST/SIC interannual variability that could contain ENSO varia-

bility or imprints of solar, or other decadal-like, oscillation (e.g. Pacific Decadal Oscillation (Wang et al., 2016)). Therefore, we hypothesize that since the solar signal above 10 hPa attributed from REF-C1-q-clim is essentially the same as in REF-C1, it represents the "top-down" mechanism only (Gray et al., 2010), i.e. a separation from a "bottom-up" mechanism and aliasing with volcanic eruptions. However, "top-down" and "bottom-up" mechanisms are not necessarily mutually exclusive since UV-induced changes in the upper stratosphere propagating downward can partly drive the troposphere-ocean response, in addition to direct forcing by total solar irradiance variations at the surface (Hood and Soukharev, 2012).

Note that the results in Table 2.2 for REF-C1-q and REF-C1-q-clim are insensitive to when our full regression model (discussed in Section 2.3) was appliedwith all regressors or when we intentionally omitted the volcanic predictor, or volcanic *and* ENSO predictors, in the original regression analysis for REF-C1-q or REF-C1-q-clim, respectively. However, the results for REF-C1 are sensitive to removing the volcanic predictor in particular. This confirms that there is the physical aliasing in the time series between the SC and other variability drivers missing from our idealized simulations REF-C1-q and REF-C1-q-clim.

Table 2.2: Normalized regression coefficient γ [unit: K] values from Eq. 2.1 and Fig. 2.2a, over the period 1980–2009 in SOCOLv3 (REF-C1, ensemble mean (em) of REF-C1-q and REF-C1-q-clim), in comparison with MERRA2 at 4 pressure levels. Values in bold denote statistical significance at 2σ confidence intervals computed by the test.

pressure levels [hPa]:	**20**	**30**	**50**	**70**
MERRA2	**0.35**	**0.52**	**0.58**	**0.47**
REF-C1 [em]	**0.52**	**0.48**	**0.35**	0.23
REF-C1-q [em]	**0.33**	0.28	0.20	0.12
REF-C1-q-clim [em]	0.21	0.09	0.02	0.04

Further evidence to support these results comes from looking at the global wavelet power spectra (Torrence and Compo, 1998), obtained for three pressure levels in the tropical stratosphere. In Fig. 2.3 we identify the occurrence of an 11-year SC periodicity in our simulations' time series. The spectra are in agreement in the upper stratosphere (Fig. 2.3a; ~ 1 hPa) for all our simulations that show a decadal periodicity that we attribute to solar variability, and a periodicity related to the QBO (~ 28 months). At lower pressure levels (20 hPa; Fig. 2.3b), we can see that the power of these two periodic signals is enhanced (note different y-axis scale) in REF-C1, where decadal variability is increased due an approximate decade of separation between volcanic eruptions (Fig. 2.1a). We confirm this by removing 3 years following the Mt. Pinatubo eruption (compare black lines in Fig. 3). QBO periodicity is enhanced especially during the Mt. Agung and Mt. Pinatubo eruptions (as indicated by the local wavelet amplitude — not shown). This enhancement may come from the fact that diabatic warming in the TLS caused by a volcanic eruption masks potential warming or cooling induced by the QBO via adiabatic heating or heating associated with downward or upward vertical motion, respectively. Down to 20 hPa we can also see that the solar (decadal-like) signal was almost identical for our two sensitivity simulations REF-C1-q and REF-C1-q-clim (see green and blue lines in Fig. 2.2a). The same fact is valid for their global power spectra in Fig. 2.3b. At 50 hPa (Fig. 2.3c) we

can see pronounced differences for periods longer than normal for the QBO between REF-C1-q and REF-C1-q-clim, i.e. decadal and ENSO-like periods (see e.g. Torrence and Compo, 1998) were filtered out in the case of REF-C1-q-clim. This supports our finding that the solar signal was reduced to almost zero at this level in the REF-C1-q-clim simulation (Fig. 2.2a). While the QBO-matched periodicity is statistically significant at all pressure levels in all simulations, i.e. the global wavelet power is above the 95% confidence interval of the corresponding mean red-noise spectrum, the decadal-like periodicity is significant only at 1 hPa in all simulations. Furthermore, while the decadal-like periodicity in REF-C1 is significant at all shown pressure levels, the global wavelet power of this periodicity in REF-C1-q exceeds the mean red-noise spectrum power only down to 20 hPa (not shown).

Before proceeding further, we briefly digress from the SC discussion to deal with an important question related to the sensitivity of the volcanic signal to the model configuration, or to the prescribed aerosol boundary conditions, since the temperature response to a volcanic eruption , and aliasing with the SC, potentially depends on both of these factors. Furthermore, it can affect the magnitude of the volcanic aliasing of the temperature response to the SC in the TLS. Figure 2.4 compares observational (HadAT2) and reanalysis (MERRA2, JRA-55) datasets with SOCOL simulations. Using time series' comparison in Fig. 2.1b-e, we have already shown that REF-C1 overestimates the warming after the Mt. Agung and Pinatubo eruptions in the TLS (see gray bar in Fig. 2.4). The warming after the Pinatubo eruption is about 1.55 and 1.50 K higher than in MERRA2 reanalysis (purple bar) and HadAT2 radiosonde data (light blue bar), respectively. The simulated warming in REF-C1 after the Mt. Agung eruption seems to be biased in terms of mean values with respect to HadAT2 and JRA-55 (about 1.40 K), though with high uncertainty. On the other hand, the warming in REF-C1 after El Chichón is slightly underestimated by 0.31 K, but is still within the range of confidence intervals. Simulated temperature anomalies in SOCOLv3 REF-C1 are overestimated because there is substantially more aerosol loading in the TLS following the Mt. Pinatubo eruption in the CCMI aerosol dataset cf. the CMIP6 dataset (Revell et al., 2017). Therefore, the magnitude of the volcanic aliasing of the solar signal in the TLS may be overestimated as well.

To examine the excessive model response to volcanic aerosols, we performed additional sensitivity simulations based on the REF-C1 setup, with 5 ensemble members covering the Mt. Pinatubo and Agung eruption periods, employing the volcanic forcing prepared for CMIP6 simulations (see orange colored bar in Fig. 2.4). For more details about the CMIP6 volcanic forcing based on the SAGE-3λ algorithm (Luo, 2016), see Revell et al. (2017). Fig. 2.4 shows that the tropical temperature response to both eruptions was reduced and is in agreement with reanalyses and HadAT2 datasets. However, this result needs to be confirmed for other CCMI models since this result holds only for SOCOLv3 and may not necessarily hold for other CCMI models.

Since the REF-C1 simulation with the CMIP6 volcanic forcing (REF-C1-CMIP6aer) did not show the overestimated warming after the Mt. Pinatubo eruption in the TLS, we test whether this change affects the magnitude of the volcanic aliasing. Fig. 2.5 shows an analogical analysis to Fig. 2.2a, i.e. profiles of the tropical temperature response to the SC, but the period 1986–2005, the period over

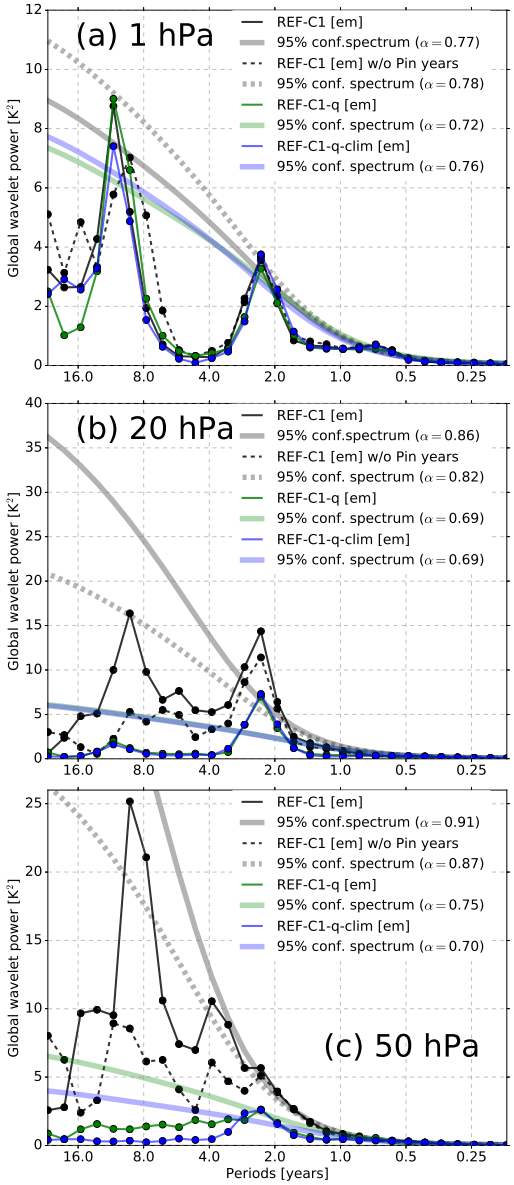

Figure 2.3: Global wavelet power spectra using a Morlet wavelet with the parameters (see details in Torrence and Compo, 1998): wavenumber $\omega_0 = 6$, $\delta t = 1/12\,\mathrm{yr}$, $s_0 = 2\delta t$, $\delta j = 0.25$ and $J = 7/\mathrm{d}j$; applied on tropical temperature detrended time series over the simulated period of particular simulation at 1 hPa (**a**), 20 hPa (**b**) and 50 hPa (**c**) for REF-C1 (black and solid lines with points), REF-C1 with $\{1991, 1992, 1993\}$ years excluded (black and dashed lines), REF-C1-q (green and solid lines with points) and REF-C1-q-clim (blue and solid line with points) simulations. The wider and less intense lines (without points) represent the 95% confidence spectrum based on the mean red-noise spectrum assuming a lag-1 α autoregressive process (AR1) of particular simulations denoted in the legend.

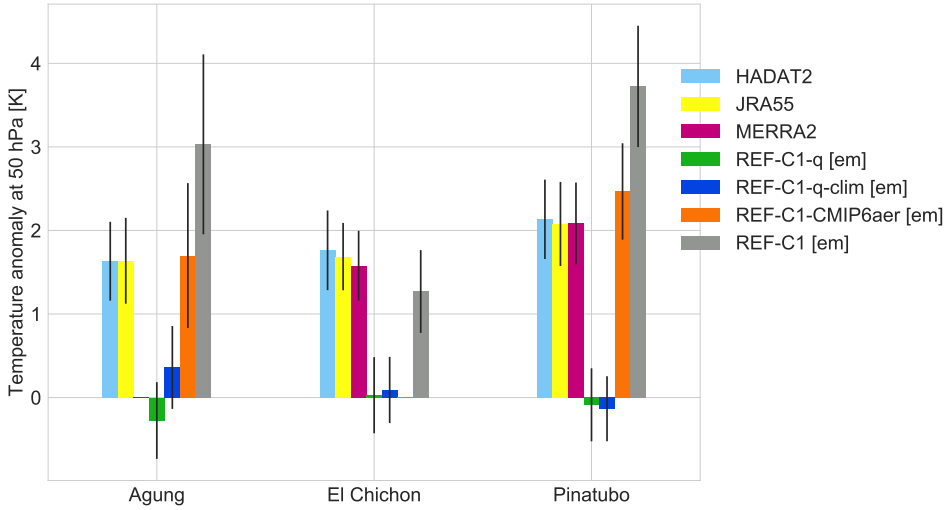

Figure 2.4: Comparison of tropical temperature responses to the eruptions of Mt. Agung, El Chichón and Mt. Pinatubo at 50 hPa between ensemble mean (em) of REF-C1 (gray bar), REF-C1 with the CMIP6 forcing (orange bar), REF-C1-q (blue bar), REF-C1-q-clim (green bar) and reanalyses MERRA2 (magenta bar) and JRA-55 (yellow bar); and radiosondes HadAT2 (light blue bar). Error bars represents 95% confidence intervals for the difference in those means.

which we have available all five ensemble members of REF-C1-CMIP6aer. The temperature response to the SC in REF-C1-CMIP6aer reveals agreement in the upper stratosphere with other SOCOL simulations. From 3 hPa downward its profile starts to diverge — revealing an overall reduced response in comparison to the original REF-C1 simulation and much closer to MERRA2 between 10 and 30 hPa. To conclude, the REF-C1-CMIP6aer ensemble shows that when the overestimated warming due to volcanic aerosols in the TLS is reduced, the magnitude of the volcanic aliasing of the temperature response to the SC is reduced as well, albeit not eliminated completely.

To document how the systematic altitude shift in volcanic forcing may influence the systematic altitude shift in the solar signal. While the temperature response to the Mt. Pinatubo volcanic eruption in REF-C1 peaks at 30 hPa, in MERRA2 it peaks at 40 hPa. This systematic shift may be a result of the CCMI volcanic forcing used: for example zonally averaged (25°S – 25°N) extinction coefficients within the infrared solar band (between 2380 nm and 4000 nm) reach a maximal height of 22.6 km ($\sim$ 35 hPa) on average during the first year after the Mt. Pinatubo eruption, and it also leads to a systematic shift in the SC temperature response (see Fig. 2.2a). In the TLS the solar signal in REF-C1-CMIP6aer peaks at 30 hPa, which is the last pressure level statistically different from zero. This documents a systematic shift in the solar signal detected in the TLS between REF-C1 with the CCMI volcanic forcing peaking at $\sim$ 20 hPa and REF-C1 with the CMIP6 volcanic forcing peaking at $\sim$ 30 hPa.

2.4.2 Effects of aliasing (multicollinearity) and autocorrelated residuals

In this subsection we examine a linear relationship between the regressors used in our attribution model Eq. 2.1, to reveal potential signs of aliasing between

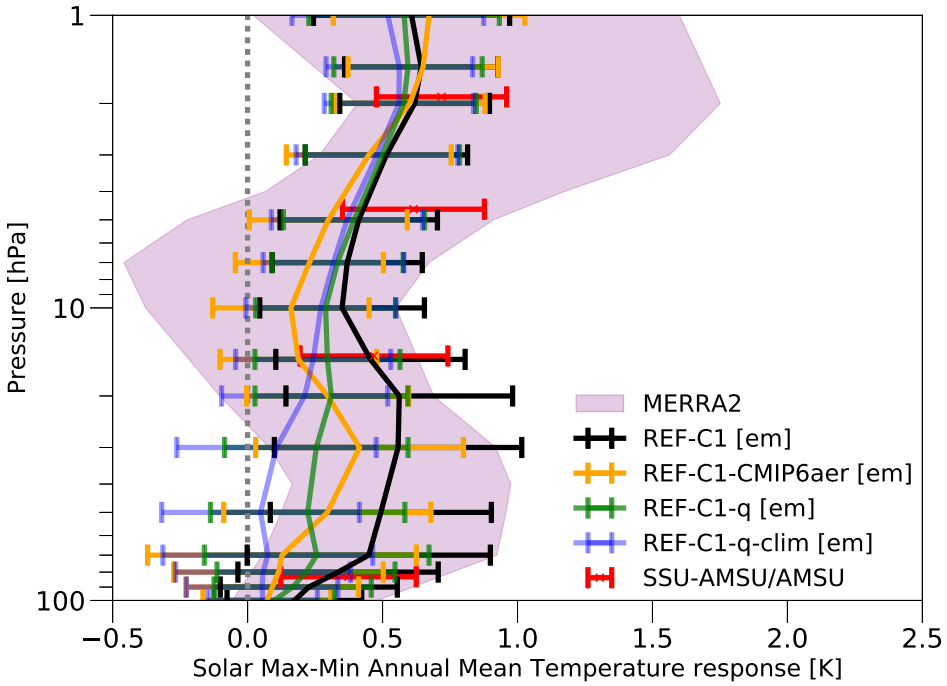

Figure 2.5: Tropical (zonal mean between 25°S and 25°N) annual mean temperature response to solar variability, i.e. normalized regression coefficient γ from Eq. 2.1, over the period 1986–2005 in SOCOLv3 (ensemble mean (em) of REF-C1, REF-C1 with the CMIP6 volcanic forcing, REF-C1-q and REF-C1-q-clim), in comparison with MERRA2, SSU-AMSU and AMSU. The signal is expressed as the average difference between solar maxima and minima in the period 1979–2013. Horizontal bars and shaded area (MERRA2): 95% confidence interval of γ coefficient (determined with AR2).

our explanatory variables. There is evidence that the alignment between the two major volcanic eruptions El Chichón and Mt. Pinatubo with the descending phases of solar maxima is likely projected into the correlation between solar and volcanic proxiesand therefore a change in the regression coefficients. However, similar alignment may also occur between solar activity and another regressor in our regression model Eq. 2.1. Therefore, in Fig. 2.6 we illustrate the evolution of the correlation matrix between all regressors used in Eq. 2.1 for an expanding analysis period that starts between years 1960 and 1999 and ending in 2009 (blue line and top blue axis), or starting in 1960 and ending between 1970 and 2009 (red line and bottom red axis). Note that the correlations were not statistically different from zero when regressors' autocorrelations were employed in estimating the statistical significance using effective sample size (see Bretherton et al., 1999, equation 31).

The correlation between solar and volcanic proxies (see zoomed-in correlation plot in the lower left corner of Fig. 2.6f) for the whole period 1960–2009 is slightly negative (far left values; ~ 0.1). After the blue curve, after Mt. Agung eruption, the correlation increases and becomes positive by 1965. Following El Chichón, the correlation reaches 0.1, and increases to 0.2 by the time of the Mt. Pinatubo eruption. Afterwards the correlation becomes negative. The negative correlation is persistent also when, instead of changing the initial year of our correlation analysis with fixed ending year 2009, we change the ending year with fixed initial year 1960 (red line and bottom axis in Fig. 2.6). This is because Mt. Agung and Awu eruptions occurred in a solar minimum between the solar maxima 19 and 20. Similarly, the negative correlation between 2000 and 2009 pertains to a period when increasing SAD values, caused by minor volcanic eruptions (Vernier et al., 2011), coincide with the declining phase of the solar maximum 23.

While correlation values between solar and volcanic proxies mostly do not exceed 0.2 (except for a very short period after the Mt. Pinatubo eruption), correlations between solar and trend proxies reach higher values and decrease as the start year is shifted back from 1999 to 1960 (red line), with an apparent solar cycle variation superimposed. Furthermore, we can see periods shorter than 1975–2009 revealing nonzero correlations between solar and ENSO proxies. This correlation sensitivity to initial and ending year of the analysis period should be taken into account when assessing whether such aliasing interferes with the attribution of the solar signal, as demonstrated in Fig. 2.2a. Since the relationships between our regressors are sensitive to the time period considered, the regression coefficients are sensitive to the initial year of the analysis period as well.

To demonstrate the impact of the regressor aliasing for various datasets, we vary the length of the regression window either with a fixed initial year or a ending year for the tropical temperature response to the SC at 50 hPa, i.e. following the approach used by Chiodo et al. (2014). The results are plotted as red errorbars in Figs. 2.7 and 2.8. In addition to SOCOL (a,b,c) and MERRA2 (e), we include the JRA-55 (d) and HadAT2 (f). The shortest period analysed was 10 years, i.e. 1999–2009 or 1960–1970, respectively.

The REF-C1 temperature response (Fig. 2.7a) is sensitive to the initial year of analysis in terms of both magnitude and statistical significance. By increasing the number of years considered in the analysis, the confidence interval becomes narrower and the response varies from near-zero (from 1992 onwards) to 0.5 K

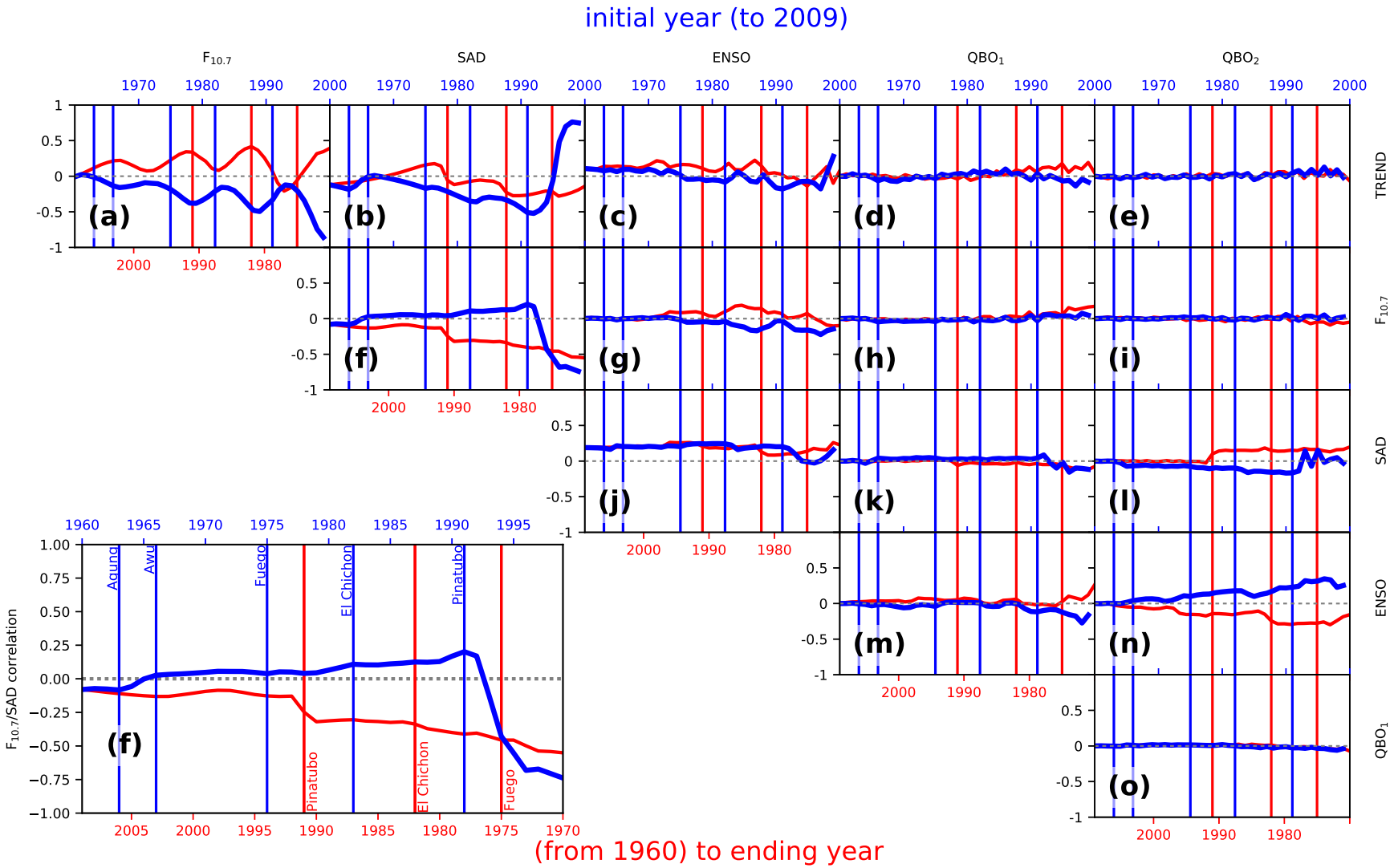

Figure 2.6: Correlation coefficients between all regressors. Blue: correlations from periods ending in the year 2009 and beginning in different starting years (indicated in time top axis). Red: correlations starting in the year 1960 closing in different ending years (indicated in the bottom axis). Vertical lines: eruptions of Mt. Agung (1963), Mt. Awu (1966), Mt. Fuego (1974), El Chichón (1982) and Mt. Pinatubo (1991). In the lower left corner the correlation plot between $F_{10.7}$ and SAD is enlarged for clarity. The statistical significance was computed by a test when regressors' autocorrelations were employed (Bretherton et al., 1999). Blue and red dots would indicate periods when $p$values < 0.05.

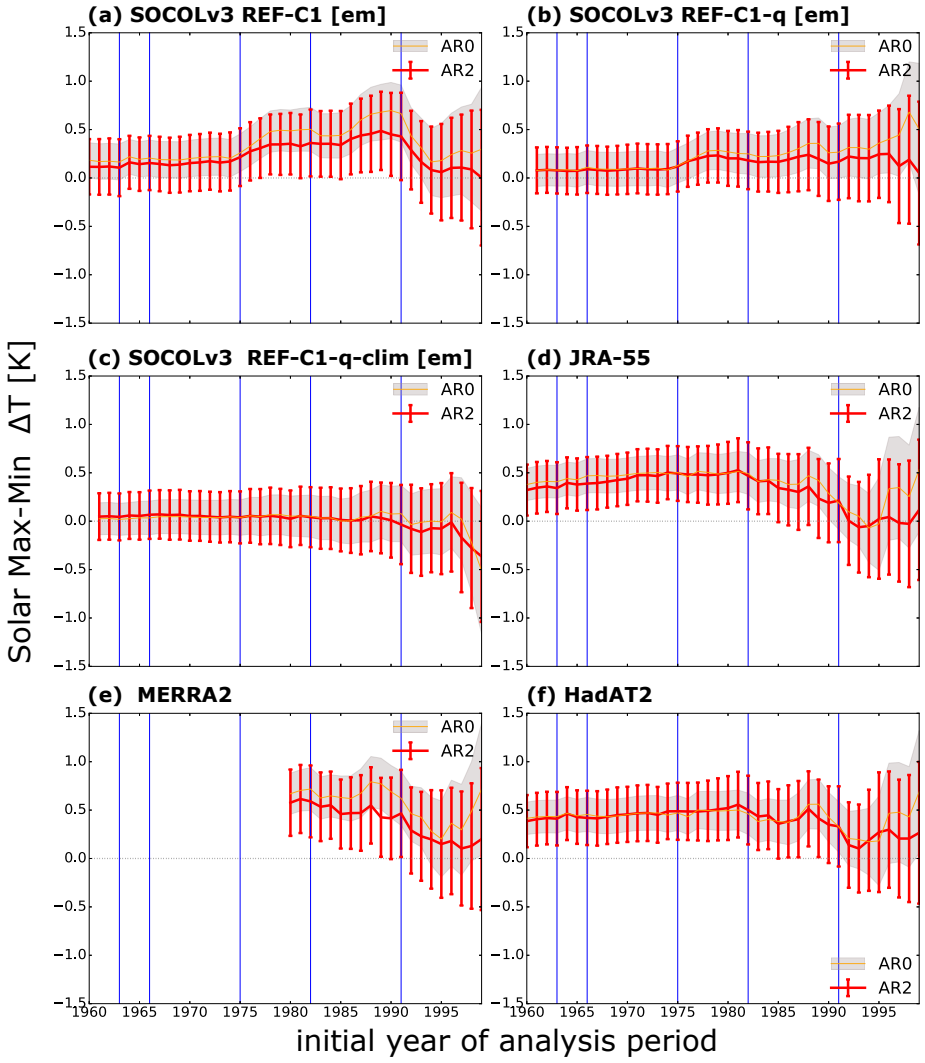

Figure 2.7: Tropical (25°S–25°N zonal mean) temperature response of various datasets or ensemble means (em) to $F_{10.7}$ at 50 hPa, when the initial year of the analysis is shifted backward in time and the ending year is fixed at 2009. Minimal analysed period: 10 years, i.e. 1999–2009. Blue vertical lines: volcanic eruptions as labeled in Fig. 2.1a. Vertical bars and shaded areas show the 95% confidence intervals, obtained with or without the AR2 residual model.

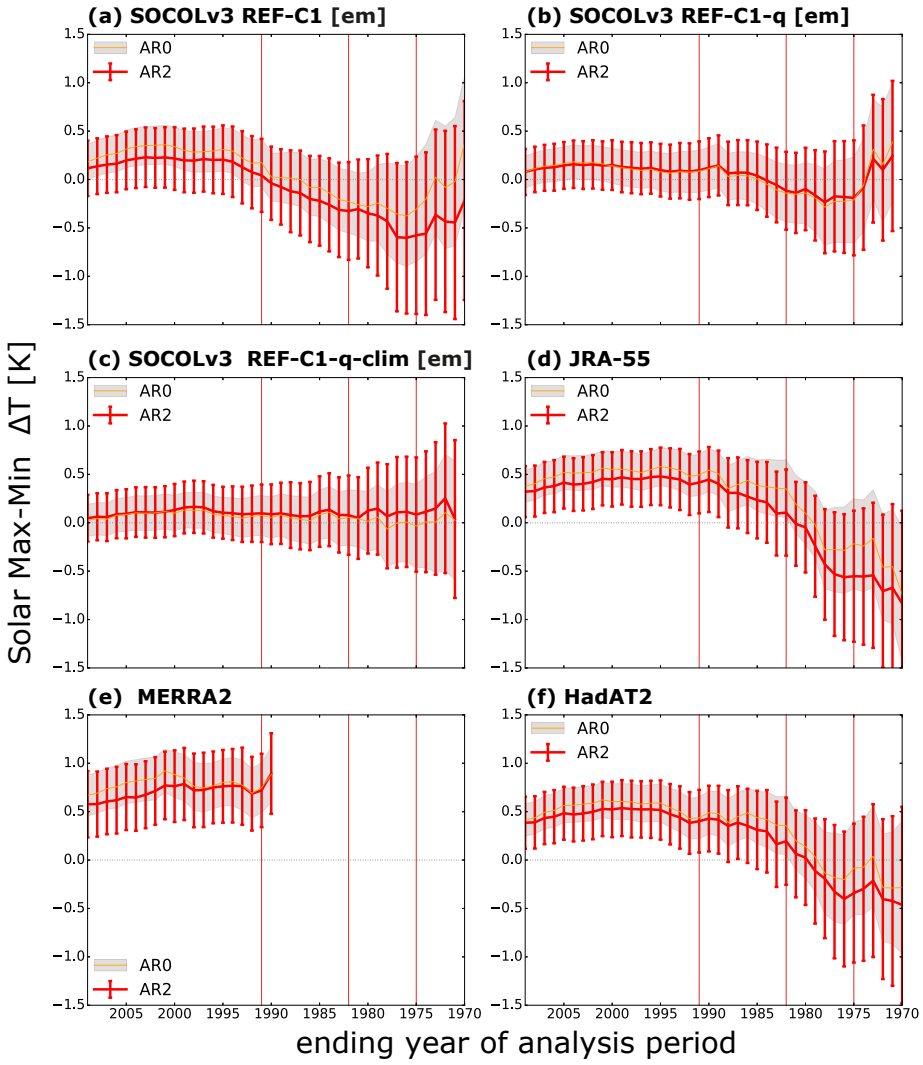

Figure 2.8: Tropical (25°S–25°N zonal mean) temperature response to $F_{10.7}$ at 50 hPa, when the ending year of the target period is shifted between 1970 and 2009 while the initial year is fixed at 1960 (minimal analysed period: 10 years). Red vertical lines: volcanic eruptions as labeled in Fig. 2.1a. Errorbars and shaded areas represent the 95% confidence intervals when using AR2 residual model or without considering the residual autocorrelations (AR0), respectively.

(1990–2009). However, when considering the whole period, i.e. 1960–2009, the temperature response converges to stable values that are not statistically different from zero. By "stability" we mean that the amplitude and confidence intervals stop varying with the initial year of analysis, which can be seen in Fig. 2.7a for periods with an initial year earlier than 1975. Note that the REF-C1-q and REF-C1-q-clim temperature responses are never statistically different from zero in Fig. 2.7b and c, respectively. The analysis with the regression window starting in 1960 and ending between 1970 and 2009 shows a similar tendency to stabilized values for longer periods where $F_{10.7}$ and SAD aliasing diminishes (see Fig. 2.8). This corresponds to the correlation analysis in Fig. 2.6f (red lines)

The evolution of the signal in REF-C1 (Fig. 2.7a), starting from 1979, is similar to the signal in MERRA2 (Fig. 2.7e) and JRA-55 (Fig. 2.7d), i.e. the regression coefficients are inflated during periods when El Chichón and Mt. Pinatubo

eruptions are considered. It clearly resembles the shape (and evolution) of the correlation between solar and volcanic proxies in Fig. 2.6f (blue line). The evolution of the signal in REF-C1-q (Fig. 2.7b) reveals "bumps" in periods with initial years after 1975 and 1985, reminiscent of the evolution of the correlation between solar and ENSO proxies. This variation diminishes in REF-C1-q-clim (Fig. 2.7c). On the other hand, the signals' stabilization effect in JRA-55 and HadAT2 is a bit shifted towards longer periods and they are still statistically significant even for the periods prior to 1980, similar to other reanalyses that have data available back to 1960, e.g. 20CR (Compo et al., 2011) or NCEP1 (Kalnay et al., 1996) (not shown). This corresponds to the fact that our simulations REF-C1 and REF-C1-q converge to positive values when periods shorter than 1960–1975 are analyzed in Figs. 2.8a and b. On the other hand, JRA-55 and HadAT2 (Figs. 2.8d and f) rather converge further to negative values for the same periods. However, they are not statistically different from zero for all cases. This indicates that the regressed solar variability is different in SOCOL simulations with prescribed SST/SIC interannual variation for the periods prior to 1975. Since REF-C1-q-clim (Fig. 2.8c) does not reveal similar behavior for any period, we consider that this difference possibly stems from the underlying SST variability and its impact on the TLS region (see also green and blue lines in Fig. 2.3c).

The misattribution of the solar signal detected by the linear regression has an elegant statistical explanation. The amplitude of the signal of one regressor is related to the presence of another regressor, so that the signal extracted in one depends partly on the other. Let's consider a simplified case where only $F_{10.7}$ and SAD regressors are included, such that

$$\mathrm{SAD}(t) = a + b\,F_{10.7}(t), \tag{2.2}$$

and the regression equation (2.1) is limited to solar and volcanic proxies. Then:

$$Y(t) = \alpha^* + \gamma^*\,F_{10.7}(t) + e(t), \tag{2.3}$$

where $\alpha^* = (\alpha + a\beta)$ and $\gamma^* = (\gamma + b\beta)$. Finally, if $\beta > 0$, i.e. if there is a positive relationship between temperature and SAD, then there are three possibilities for b:

1. $b < 0$ represents a negative correlation between $F_{10.7}$ and SAD and $\gamma^* < \gamma$, i.e. the computed solar regression coefficient is underestimated;

2. $b > 0$ represents a positive correlation between $F_{10.7}$ and SAD and $\gamma^* > \gamma$, i.e. the computed solar regression coefficient is overestimated;

3. $b \sim 0$ represents no correlation between $F_{10.7}$ and SAD and $\gamma^* \sim \gamma$ (non-aliased regression coefficient).

Figure 2.6f shows the negative correlation ($b < 0$) for the periods after the Mt. Pinatubo eruption, which gives an underestimated regression coefficient; in REF-C1 (Fig. 2.7a) the mean value, although not negative, is at its lowest for the periods considered. On the other hand, in the periods between Mt. Agung and Mt. Pinatubo, we observe positive correlations ($b > 0$). This corresponds to the larger estimates of the temperature response (Fig.2.7) and, from above, this

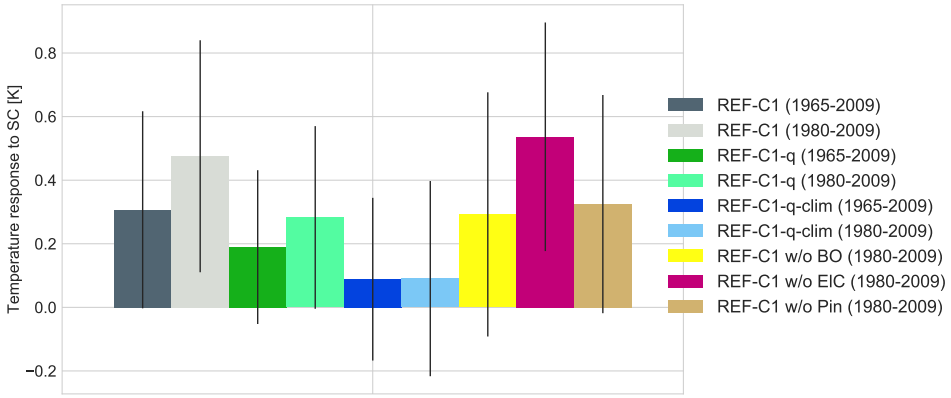

Figure 2.9: Tropical annual mean temperature response to the SC over the periods 1980–2009 and 1965–2009 at 30 hPa, where the tropical temperature response to volcanic eruptions maximizes (Fig. 2.2b), in REF-C1 (grey bars), REF-C1-q (green bars) and REF-C1-q-clim (blue bars). In addition, the temperature response in REF-C1 over the period 1980–2009 was analysed when years with particular volcanic eruptions, i.e. El Chichón (magenta bar; ElC) or Mt. Pinatubo (tan bar; Pin), were removed individually or both at same time (yellow bar, BO).

suggest that this would be an overestimate. Finally, if we consider periods in REF-C1 (Fig. 2.7a) prior to 1966, long enough to eliminate the correlation between solar and volcanic proxies ($b \sim 0$), i.e. when El Chichón and Mt. Pinatubo eruptions are aligned with solar maxima with the descending phase of solar maxima 21 and 22, the signal in temperature stabilizes and is in good agreement with REF-C1-q and REF-C1-q-clim (Figs. 2.7b and c) where no volcanoes are present.

Figure 2.9 illustrates how the tropical annual mean temperature response to the SC changes at 30 hPa when years with either (BO) both El Chichón and Mt. Pinatubo eruptions (yellow bar) or particular eruptions (magenta bar for El Chichón (ElC) or tan bar for Mt. Pinatubo (Pin)) only were removed. The temperature response at in REF-C1 over the period 1980–2009 (dark-gray bar) was reduced down to the temperature response over the period 1965–2009 (light-gray bar). Note that we reach a similar value (~ 0.3 K) in REF-C1-q over the period 1980-2009 (sea-green bar) in comparison to REF-C1 over the period 1965–2009 and REF-C1 over the period 1980–2009 when years covering either both or Mt. Pinatubo in particular eruptions were removed. However, the temperature response over the period 1965–2009 (green bar) is slightly lower. These results show that the aliasing with the volcanic signal can be avoided either by removing years mainly with Mt. Pinatubo or by analyzing a sufficiently long period to reach stable results. The temperature response is reduced further, down to ~ 0.1 K, in REF-C1-q-clim (blue and light blue bars). This suggests that one is not able to remove the aliasing coming from SST/SIC variability.

Further overestimation in REF-C1 may stem from Eq. 2.2, where we assumed that $F_{10.7}$ and SAD are independent of other regressors. Note that the multi-collinearity is rather a property of a set of regressors, not just a pair of them, i.e. that $F_{10.7}$ and SAD are also correlated with TREND and ENSO (as shown in Figs. 2.6a,g and b,j, respectively). The multicollinearity is projected into the solar signal through the volcanic aerosols and ENSO influence in the TLS, i.e. through volcanic and ENSO signatures operating in this region (Mitchell et al., 2015b). The same logic may be applied in the upper stratosphere where the long-term anthropogenic trend reveals even higher relative importance than the

11-year solar cycle variability (Ball et al., 2016).

The autocorrelation modeling has already been examined by Mitchell et al. (2015c), comparing MLR results obtained with two different methods that treat autocorrelation in residuals and one without any residual modeling (AR0). The first method, developed by Tiao et al. (1990), corresponds to our regression model, i.e. modeling residuals as an autoregressive process. However, first order autoregressive (AR1) modeling has been used in the study by Mitchell et al. (2015c), arguing that AR1 was sufficient and higher order autoregressive processes did not change the significance of the results. The second method, following the Box-Jenkins prewhitening procedure (Box, 2012), was used by Chiodo et al. (2014). The sensitivity test by Mitchell et al. (2015c) demonstrated that the Tiao method gives the most conservative estimate and shows that the Box-Jenkins method, as well as a setup without any residual modeling, may lead to an over-confident statistical significance.

In agreement with Mitchell et al. (2015c), we also found that the AR1 process occasionally sufficed to approximate the residual structure, but only in the upper stratosphere (not shown). The differences between our results with AR0 and AR2 (corresponding to the Tiao method with second order autoregressive modeling) in the lower stratosphere in Figs. 2.7 for REF-C1 (a), REF-C1-q (b) and MERRA2 (d) and others considering very short periods also demonstrate that the standard deviation of the solar regression coefficient is underestimated and the amplitude estimate may be biased as well. These findings are consistent with the statistical modeling literature (e.g. Neter et al., 2004; Thejll, 2005).

Figure 2.10a shows that AR1 removes most of the autocorrelation in residuals, but not completely. This finding is in agreement with the study by Ball et al. (2016) concluding that AR1 was necessary, but not sufficient. Furthermore, Figures 2.10a and 2.10b indicate that, for periods prior to approximately 1975, AR3 would be able to completely remove the autocorrelation. However, the partial autocorrelation function in Fig. 2.10c documents that the regression analysis with AR2 removes the autocorrelation from the residuals. While the radiative time scale in the lower stratosphere has been estimated to be between 30 to 100 days (Randel et al., 2002; Hood, 2016), the radiative relaxation time scale in the upper stratosphere is around 10 days (Mlynczak et al., 1999; Brasseur and Solomon, 2006). While we cannot provide a robust physical explanation, these radiative timescales could hint at the physical explanation as to why the lower tropical stratosphere should be treated with a higher order of AR process.

2.5 Conclusions

Using the SOCOLv3 model, and our own MLR-based tool called *X-regression* (Kuchar, 2016), we have characterized the tropical temperature variability to the 11-year SC. The upper stratospheric response in SOCOL reveals good agreement with SSU observations, but it is underestimated in comparison to the MERRA2 reanalysis. The origin of the systematic altitudinal difference of SC attribution in the TLS between SOCOL and MERRA2 reanalysis may be due to volcanic aerosol forcing data in the model. We discussed the sensitivity of our model to the prescribed aerosol boundary conditions compiled for CCMI and CMIP6 initiatives, and conclude that SOCOLv3 with the CCMI aerosol forcing gives a

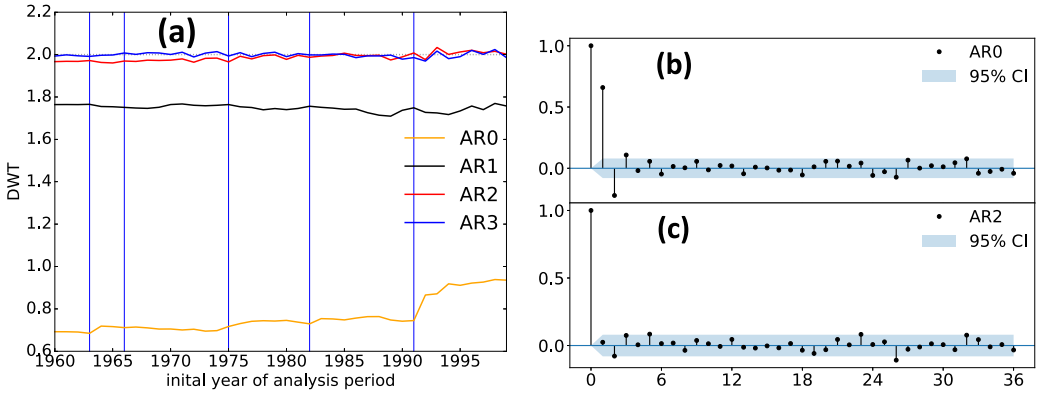

Figure 2.10: (**a**) Durbin-Watson test (DWT) (Durbin and Watson, 1950) of residuals from particular autoregressive residual models (AR) in regression analysis of REF-C1 tropical temperature time series at 50 hPa, for the analysis periods starting between 1960 and 1999 and ending at 2009 (minimal analysed period: 10 years). Dotted gray line represents DWT = 2 indicating no autocorrelation. (**b**) Partial autocorrelation function (PACF) of residuals modeled as (**b**) AR0 and (**c**) AR2 for regression analysis of REF-C1 [em] tropical temperature time series at 50 hPa over the period 1965–2009.

overestimated temperature response to volcanic aerosols and possibly leads to an overestimated volcanic aliasing of the solar response. On the contrary, utilization of the new CMIP6 volcanic forcing removed this overestimation due to the volcanic aerosol heating effect during the Mt. Agung and Pinatubo eruptions. Furthermore, the aliasing of the solar response was reduced in our short model experiments using the new CMIP6 volcanic forcing.

Using the SOCOL CCM sensitivity simulation REF-C1-q and statistical techniques such as wavelet analysis, in addition to MLR, we have shown that the fraction of the temperature response in the TLS attributable to the 11-year solar cycle is only about half of that found in previous studies analyzing model simulations (Hood et al., 2015; Mitchell et al., 2015c) or reanalyses (Mitchell et al., 2015b) based on the periods coinciding with satellite measurements. This reduction is a result of removing the volcanic forcing from the time series and confirms the results of Chiodo et al. (2014), where a different CCM to SOCOLv3 was used.

The use of climatological SSTs/SICs, in addition to background stratospheric aerosols, completely removes volcanic and ENSO signals and almost entirely eliminates the lower stratospheric solar cycle signal. This highlights the crucial role of SST/SIC interannual variability in simulating the secondary maximum in the TLS. Therefore, we hypothesize that the SC attribution in REF-C1-q-clim represents the UV-induced changes in the upper stratosphere propagating downward, i.e. a separation from the non-UV-induced or other decadal-like changes in the surface propagating upward. These results may contribute to the discussion about how stratospheric temperature perturbations implied by the 11-year solar cycle propagate to the troposphere (Mitchell et al., 2015c). The fact that the annual temperature response to the SC in the TLS was not detected in the REF-C1-q-clim simulation implies that the temperature response in the TLS may be induced only in winter (being masked in the annual mean) by a weaker BDC (Kodera and Kuroda, 2002) and that the solar signal propagates downwards via the equatorial route proposed by Simpson et al. (2009). Or, the signal may propagate via the polar route hypothesized by Kodera (2005), or through a combination of these

two routes (Kidston et al., 2015). These hypotheses need further investigation.

Using our simulations and regression-based attribution to the SC, we showed that it is possible to provide robust estimates either by removing the years following strong volcanic events (recommended for datasets limited for example by the satellite observational era) or analyzing a sufficiently long period, such as 1965–2009 (recommended for analyses of climate model simulations). However, the resulting estimates are still largely impacted by the aliasing with SST/SIC variability.

We explain how a misattribution of another regressor to the solar signal may occur as a result of their collinearity, leading to aliasing. This incorrect attribution, in essence, leads to incorrect conclusions. Therefore, when using MLR without supporting model simulations, one needs to be concerned about the aliasing of the regressors and, consequently, about the proper choice of time period used for the attribution.

Finally, residual modeling is essential to properly determine the statistical significance and amplitude of the signals of interest. We demonstrate that the first order autoregressive process (AR1) was necessary in our analyses, but not sufficient to completely account for the residuals' autocorrelation, especially in the lower stratosphere, which was better represented with AR3. These issues are crucial for correct trend analysis or model validation based on the regression approach.

3. Role of parametrized orographic gravity waves in the lower stratosphere

3.1 Theoretical background

Propagation of waves is one of the most important coupling mechanism between atmospheric layers. The restoring force acting on fluid particles displaced from their equilibrium states is supplied either by gravity (responsible for internal gravity waves (GWs)) or by the poleward gradient of the planetary vorticity (for planetary-scale Rossby waves (PWs)) (Andrews and McIntyre, 1987). Mixed modes such as Rossby-gravity waves may arise for GWs with horizontal scales from 1000 km. The planetary and gravity waves allow the transport of momentum and energy from their source regions. The dominant sources of gravity waves include topography (mountain or orographic gravity waves (oGWs)), convection (mainly in the tropics and subtropics), wind shear and other sources in the vicinity of jet streams and frontal systems (Fritts and Alexander, 2003). Gravity wave amplitudes grow exponentially as they propagate upward from their perturbation regions due to the decrease of the atmospheric density with increasing altitude. The breaking of vertically propagating GWs implies important consequences for the mean flow from the upper troposphere upward.

In the mesosphere gravity waves play a major role, causing complete zonal wind reversals and driving the mesospheric branch of meridional residual circulation. While their effects in the stratosphere have been seen as second-order behind planetary waves (Alexander, 2010), recent developments in observation (Ern et al., 2016) and modeling (Watanabe et al., 2008; Kalisch et al., 2016; Holt et al., 2017) of GWs have shown that the importance is region-dependent (Limpasuvan et al., 2012) and somewhat model-dependent (Butchart, 2014). In addition to mountain waves' forcing on the circulation, they trigger the formation of polar stratospheric clouds (PSCs) by temperature perturbations (e.g. Alexander et al., 2011). Thus these small-scale features are also important for polar ozone concentrations because of the chlorine activation.

In theory flow over topographic features can generate stationary oGWs (Eliassen, 1960) carrying westward momentum upward and breaking at the critical levels (Teixeira, 2014). For gravity waves with frequencies larger than the Coriolis parameter f but smaller than the buoyancy frequency N, we may relate the background wind and stability to the vertical wavelength (Limpasuvan et al., 2011)

$$c_h - \bar{U} = -\frac{N\lambda_z^{oGW}}{2\pi} \tag{3.1}$$

where $\bar{U}$ is the local horizontal wind speed, N is the buoyancy frequency, c represents the horizontal phase speed and λ_z is the vertical wavelength. The vertical wavelength is given for long mountain ($c_h = 0$) waves by (Eckermann and Preusse,

1999)

$$\lambda_z^{oGW} = 2\pi \frac{\bar{U}}{N} \tag{3.2}$$

The level where c_h matches $\bar{U}$ is called the critical level and is where the vertical wavelength goes to zero. In reality, due to instability and dissipation mechanisms, this is actually the convergence limit (Fritts and Alexander, 2003). The concept of critical levels has been used in the first parametrizations of GWs (e.g. Lindzen, 1981) in middle atmosphere models (e.g. Holton, 1982, 1983). Therefore, the critical level filtering only allows gravity waves with phase speeds out of the range of horizontal winds in the stratosphere to reach the mesosphere (Andrews and McIntyre, 1987).

Vertical or horizontal wavelengths are usually smaller than the resolution in the current general circulation models (GCMs), ans is especially valid for chemistry-climate models (CCMs) where the interactive chemistry needs to be taken into account. Therefore, these unresolved processes must be parameterized (McLandress, 1998).

To document the zonally averaged motion of air parcels, we have to take into account the effects of so-called eddies (fluctuations around the zonal mean). For understanding the middle-atmospheric circulation, a useful quantitative framework based on transformed Eulerian-mean (TEM) equations has been developed and is still abundantly used despite its limitations (Haynes, 2005), e.g. small-amplitude wave disturbances and zonally symmetric basic flows. The transformation leading to the TEM equations was introduced by Andrews and McIntyre (1976, 1978); Boyd (1976). Using TEM equations in spherical (φ), log-pressure[1] coordinates, we document how in the two-dimensional perspective wave forcing affects the mean flow ($\bar{u}$) as well as the meridional transport:

$$\bar{u}_t + \bar{v}^* \left[(\rho_0 a \cos\varphi)^{-1} (\bar{u} \cos\varphi)_\varphi - f \right] + \bar{w}^* \bar{u}_z = (\rho_0 a \cos\varphi)^{-1} \nabla \cdot \vec{F} + R \equiv \bar{\mathcal{F}} \tag{3.3}$$

where f is the Coriolis parameter[2], a is the earth's radius, ρ_0 is a standard reference density and $\bar{R}$ denotes the residual term representing sub-grid scale processes such as GWD and numerical diffusion. The vector $\vec{F}$ is known as the Eliassen-Palm (EP) flux:

$$F^{(\varphi)} = \rho_0 a \cos\varphi \left(\bar{u}_z \overline{v'\theta'} / \bar{\theta}_z - \overline{v'u'} \right), \tag{3.4a}$$

$$F^{(z)} = \rho_0 a \cos\varphi \left\{ \left[f - (\rho_0 a \cos\varphi)^{-1} (\bar{u} \cos\varphi)_\varphi \right] \overline{v'\theta'} / \bar{\theta}_z - \overline{w'u'} \right\} \tag{3.4b}$$

together used in the EP flux divergence (EPFD):

$$\nabla \cdot \vec{F} = (a \cos\varphi)^{-1} \left(F^{(\varphi)} \cos\varphi \right)_\varphi + F_z^{(z)} \tag{3.5}$$

The residual mean meridional circulation representing the Brewer-Dobson circulation (BDC) is defined by

$$\bar{v}^* = \bar{v} - \rho_0^{-1} (\rho_0 \overline{v'\theta'} / \bar{\theta}_z)_z, \tag{3.6a}$$

$$\bar{w}^* = \bar{w} + (a \cos\varphi)^{-1} (\cos\varphi \overline{v'\theta'} / \bar{\theta}_z)_\varphi \tag{3.6b}$$

[1] $z = -H \ln(p/p_s)$ where p_s is a standard reference pressure (usually $\approx 10^3$ hPa) and H is a mean scale height (usually ≈ 7 km) (Andrews and McIntyre, 1987).

[2] It equals to $2\Omega \sin\varphi$ where $\Omega \doteq 7.292 \cdot 10^{-5}\,\mathrm{s}^{-1}$ is the earth's rotation rate.

Overbars and primes denote zonal mean and anomalies from the zonal mean, respectively. The subscripts denote derivatives.

Another conservation equation exists named the generalized EP theorem by Andrews and McIntyre (1976) between the divergence of EP flux $\nabla \cdot \vec{F}$ and the time derivative of zonal-mean wave activity density known as wave transience A_t:

$$A_t + (a\cos\varphi)^{-1}\nabla \cdot \vec{F} = S \tag{3.7}$$

where S represents nonconservative sink or source of wave activity. Note that we show the relationship above with the quasigeostrophic (QG) finite-amplitude wave activity (FAWA) derived by Nakamura and Solomon (2010). Nakamura and Zhu (2010a) have introduced FAWA based on the areal displacement of QG potential vorticity from zonal symmetry. 2D representation of FAWA has recently been generalized longitudinally (Huang and Nakamura, 2016) representing *local* wave activity (LWA) to diagnose eddy-mean flow interaction on the regional scale. By combination of Eqs. 3.3 in the QG form and 3.7 we obtain

$$\bar{u}_t - f\bar{v}^* = -A_t + S + R \tag{3.8}$$

Hence for steady and conservative waves, the zonal mean flow (when the residual term R is neglected) neither the meridional residual circulation is accelerated. This is an example of the nonacceleration theorem firstly noted by Charney and Drazin (1961).

While 3D representation of stationary and transient planetary wave fluxes has been examined earlier (Plumb, 1985, 1986), the 3D structure of the BDC was first described by Callaghan and Salby (2002) and the research has been continuously advanced (Kinoshita et al., 2010; Kinoshita and Sato, 2013; Sato et al., 2013; Noda, 2014; Kinoshita et al., 2016). The 3D structure of the residual circulation has been linked with zonal asymmetries in ozone and water vapor in the northern hemisphere (Demirhan Bari et al., 2013) and temperature and ozone in the southern hemisphere (Hirano et al., 2016).

Using the 2D TEM formulation and continuity equation (not shown) under the steady state limit we obtain the downward control principle of Haynes et al. (1991) for the extratropical residual-mean vertical velocity

$$\bar{w}^*(\varphi, z) = (\rho_0 \cos\varphi)^{-1}\left[\int_z^\infty \left(\frac{\rho_0 a \bar{\mathcal{F}}\cos^2\varphi}{\bar{m}_\varphi}\right)_{\varphi=\varphi(z')} \mathrm{d}z'\right]_\varphi \tag{3.9}$$

where $\bar{m} = a\cos\varphi(\bar{u} + a\Omega\cos\varphi)$ is the angular momentum per unit mass. The integration is along a contour of constant $\bar{m}$. From $\pm 15°$ poleward contours of $\bar{m}$ are typically vertical, e.g. see Fig. 1 in Haynes et al. (1991) or Seviour et al. (2012). Wave drag $\bar{\mathcal{F}}$ (the sum of resolved and unresolved waves — although in principle they may be examined separately) acting above level z controls the vertical residual velocity $\bar{w}^*$. Seasonal average is considered as sufficient for the steady state limit (Rosenlof and Holton, 1993). By the downward control principle, i.e. by a redistribution of mass via induced upwelling and downwelling, stratospheric wave disturbances can extend to the troposphere and lead to surface (pressure) responses (Haynes and Shepherd, 1989). Another mechanism proposed to explain the stratosphere-troposphere coupling is by modification of wave breaking or reflection either by background flow change or wave property change (Martineau

and Son, 2015, and references therein), although the combination of the downward control principle and the latter is also possible (Song and Robinson, 2004). Although the underlying dynamical mechanisms may not be fully understood, a single unifying mechanism may act across different timescales ranging from daily to decadal variations (Garfinkel et al., 2015; Kidston et al., 2015).

While the downward control principle is appropriate when studying momentum transfers by large-scale waves for which the approximation by zonally symmetric torques is reasonable, studying atmospheric responses to momentum deposition associated with GWs may not be appropriate (Shaw and Boos, 2012; Boos and Shaw, 2013). Localized GW breaking regions considered as hotspots serves as an example of zonally asymmetric torques in the middle atmosphere. These hotpots associated with orographic GWs have been typically identified above well-known topographic structures such as the Andes and the Antarctic Peninsula in the SH, and the Rocky Mountains, the Scandinavian range and the Himalayas (Hoffmann et al., 2013). Since recent satellite observations indicated that oGWs's horizontal propagation can be detected several hundreds of kilometers from their source regions (e.g. Alexander and Teitelbaum, 2011; Ehard et al., 2017), the horizontal propagation should be taken into account in parametrization schemes of oGWs usually assuming only the vertical propagation (Xu et al., 2017).

A typical mid-winter example of strong stratosphere-troposphere coupling in the northern hemisphere are stratospheric sudden warming (SSW) events. SSWs, first observed by Scherhag (1952), are characterized by a significant and abrupt increase of polar temperature in the middle and upper stratosphere. These changes are associated with polar vortex (PV) disruption triggered by an anomalous wave activity either injected from the troposphere (Matsuno, 1970) or rather the state of the stratosphere itself is responsible for the upward wave activity propagating from below (Scott and Polvani, 2004; Hitchcock and Haynes, 2016, e.g.). However, Birner and Albers (2017) have recently showed that the latter mechanism is more important for the majority of SSW-like events. Furthermore, the stratospheric self-tuning resonance mechanism has been analyzed in an idealized model based on vortex geometry: either the PV is split into two smaller vortices (Matthewman and Esler, 2011) or the PV is displaced from the poles (Esler and Matthewman, 2011). Using the composite analysis, Albers and Birner (2014) have examined the evolution of the PV during both types of SSWs in the reanalysis data. When focused on split events they stated that planetary and/or gravity waves tune the vortex geometry toward its resonant excitation points.

In this study, we focus on the role of parametrized oGWs in the lower stratosphere and their possible links to SSW events. The validation of simulated GWD as well as the model itself (see Section 3.2) in comparison with most recent observational datasets (see Section 3.3) precedes all analyses. Furthermore, we introduce the motivation as to why the effects of small-scale GWs generated by topography matter to the study (see Section 3.4). In Section 3.5 we describe the methodology allowing to attribute the intermittency of parametrized oGWs, which leads to short (on a daily time-scale) and strong bursts of localized wave forcing in the lower stratosphere. In section 3.6.1 we describe the 2D and 3D structure of composite responses of standard variables such as temperature, zonal wind and ozone. The composite responses are examined for the three most apparent

hotspots of oGWs' breaking in the lower stratosphere. In section 3.6.2 we use EP flux and TEM equations supported by Plumb and the zonal mean of LWA (∼FAWA) or LWA diagnostics to explain responses in the former section. Finally in Section 3.6.3 we suggest possible links of these lower-stratospheric hotspots to SSW-like events. Conclusions are presented in Section 3.7.

3.2 Data

The study is based on composite analysis that has been applied to the Canadian Middle Atmosphere Model (CMAM, McLandress et al., 2013a). CMAM is chemistry climate model with 71 levels up to about 100 km with variable vertical resolution. These model levels were interpolated to 63 pressure levels extending up to $7 \cdot 10^{-4}$ hPa. This model version has a triangular spectral truncation of T47, corresponding to a 3.75° horizontal grid. Furthermore, this model version has been nudged on large spatial scales (<T21) to the 6-hourly horizontal wind and temperature time-series from ERA-Interim (Dee et al., 2011b) up to 1 hPa between 1979 and 2010 thus furthermore marked as CMAM30. More details about the nudging can be found in McLandress et al. (2014). Since the following analyses are focused on the troposphere-stratosphere-mesosphere coupling rather than the Mesosphere Lower-Thermosphere (MLT) region, we do not use the extended version of CMAM30 (Fomichev et al., 2002; Shepherd et al., 2014) with the lid at $2 \cdot 10^{-7}$ and sparser horizontal resolution (T32), which is also freely available for download[3]. The existence of discontinuities in 1979, 1985, and 1998 was removed from the model data using a procedure by McLandress et al. (2014).

Orographic GWD (oGWD) and non-orographic GWD (nGWD) are parameterized using the schemes of Scinocca and McFarlane (2000) and Scinocca (2003), respectively. The oGWD scheme employs two vertically propagating zero-phase-speed gravity waves (GWs) to transport the horizontal momentum into the half-space to the left and right of the resolved horizontal velocity vector at the launch layer, which extends from the surface to the height of the subgrid topography (McLandress et al., 2013b). The orientation and magnitude of the momentum flux carried by these two waves depends on the near-surface wind speed, its direction relative to the orientation of the subgrid topography (anisotropic effects), and the static stability in the launch layer. There are two tunable parameters: the integrated radial dependence of the pressure drag ($G(y) = 0.65$) scaling the total vertical flux of horizontal momentum and the inverse critical Froude number ($\mathrm{Fr}_{\mathrm{crit}} = 0.375$) determining the breaking height. These values have been tuned to reduce warm temperature biases in the SH climatology which were inadmissible for the proper modelling of the formation of polar stratospheric clouds and thus problematic for modelling the heterogeneous chemical reactions that drive polar ozone loss (Scinocca et al., 2008). The nGWD scheme considers a spectrum of nonzero-phase-speed GWs propagating horizontally into the four cardinal directions at the fixed launch level ($\sim$ 125 hPa) and with a typical launch flux ($\sim 10^{-4}$ Pa). These parameters are tuned to exert proper drag in the upper stratosphere and mesosphere. The requirement of nGWD is especially important to drive the residual circulation from the summer mesosphere.

[3] `http://climate-modelling.canada.ca/climatemodeldata/cmam/output/index.shtml`

CMAM30 has been extensively evaluated against observations (e.g. Shepherd et al., 2014) and it has been shown that CMAM30 is warmer by up to 5 K in the polar stratosphere, with a low bias in the mesosphere of ∼5-15 K (Pendlebury et al., 2015). Comparison of the regular and extended version of CMAM30 (CMAM30-ext) by Kuilman et al. (2017) has shown substantial differences in the winter and summer mesospheric temperature. These discrepancies were attributed to the different non-orographic GW parametrization, i.e. by Hines (1997a,b), used in CMAM30-ext. However, the orographic GW parametrization also differs since the CMAM30-ext uses the parametrization by McFarlane (1987, see further discussion in Section 3.4).

3.2.1 Datasets used for model evaluation

To evaluate CMAM30 representation of temperature, zonal wind and GWD, we utilize the most recent generation of NASA's reanalysis Molod et al. (2015): MERRA2 (Modern Era Reanalysis for Research and Applications-2) version of the Goddard Earth Observing System-5 (GEOS-5). In comparison with the previous generation, substantial improvements have been found in some key aspects of the mean circulation in MERRA2 attributed to specific changes in parametrizations or increased spatial resolution (Molod et al., 2012). For example, an increased intermittency factor from 0.125 to 0.3125 south of approximately 40°S in orographic gravity wave parametrization leads to a more delayed jet breakup in austral winter. The MERRA2 dataset is provided on a 3-hourly basis with the vertical range to 0.1 hPa; however, the model lid is at 0.01 hPa. The horizontal resolutions of the dataset were increased to 0.5°x0.5° from 1.25°x1.25° in MERRA.

We also compare CMAM30 with the independent (i.e. not assimilated in MERRA2) measurements represented by the SABER instrument on the NASA's TIMED (Thermosphere Ionosphere Mesosphere Energetics Dynamics) satellite. Temperature profiles are retrieved from infrared CO_2 emissions from the atmospheric limb. Here we use the retrieval version V2.0[4] over the continuous coverage for the latitudes of 52°S and 52°N only. The temperature outputs are available over altitudes $16 - 100$ km with a vertical resolution of 1.9 km (Remsberg et al., 2008). The estimated accuracy is 1.5 K between 15-80 km.

SABER together with HIRDLS (High Resolution Dynamics Limb sounder) aboard NASA's Aura satellite have been used to compile the gravity wave climatology dataset GRACILE[5] (Ern et al., 2018). The GRACILE data set is suitable for comparison with GW distributions in global models either with parametrized or resolved GWs. SABER and HIRDLS distributions have been previously compared with climate models and radiosonde observation by Geller et al. (2013); however, just the months of January and July of only a few years were compared.

Finally, we compare CMAM30 with other nudged CCMs simulated within the Chemistry-Climate Model Initiative (CCMI; Morgenstern et al., 2017b), i.e. REF-C1SD simulations: the CCMI version of CMAM (nudged with ERA-Interim up to 1 hPa), 4 different versions of EMAC (nudged with ERA-Interim up to 10 hPa), MRI-ESM1r1 (nudged with JRA-55 up to 1 hPa), CCSRNIES-MIROC3.2

[4]Available from `http://saber.gats-inc.com`

[5]The data set is available at `https://doi.org/10.1594/PANGAEA.879658`.

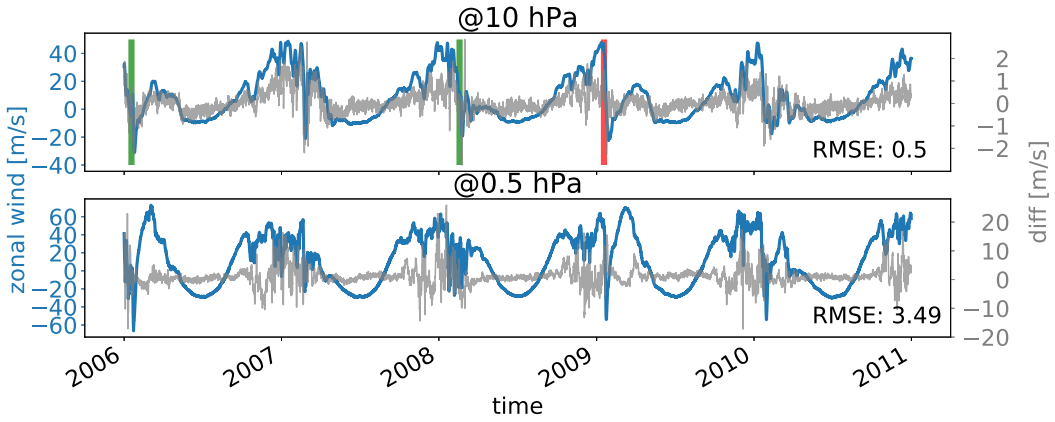

Figure 3.1: Polar-cap (60-90°N) area-average of 6-hourly zonal wind time-series in CMAM30 at 10 hPa (upper panel) and 0.5 hPa (lower panel) for the period 2006-2010 (blue lines). CMAM30 is compared with MERRA2 (gray lines to indicate difference between MERRA2 and CMAM30). The comparison is summarized by root-mean-square error (RMSE) in the lower-right corner of each panel. Red and green vertical lines represent split and displacement SSW events, respectively.

(nudged with ERA-Interim up to 1 hPa and with CIRA up to 0.01 hPa), CNRM-CM5-3 (nudged with ERA-Interim in all model levels) and CESM1-WACCM (nudged with MERRA up to 50 km). For all details on how nudging and gravity wave drags (orographic and non-orographic) were implemented in those models, we use here, see Table S30 and S3 in Morgenstern et al. (2017b), respectively. We use only monthly outputs available on pressure levels over the period 1990–2010[6] for orographic and non-orographic gravity wave drag in zonal direction (for all models) and EP flux divergence (except[7] CESM1-WACCM).

3.3 CMAM30 evaluation

Figure 3.1 shows how the CMAM30 model is closer to MERRA2 reanalysis from a deterministic point of view, i.e. through the polar-cap (60-90°N) area-average of the 6-hourly zonal wind time-series in CMAM30 at 10 hPa (upper panel) and 0.5 hPa (lower panel) in comparison with the MERRA2 dataset for the limited period of 2006-2010. As expected, CMAM30 is in good agreement with MERRA2 at 10 hPa, i.e. within the nudging region and at the pressure level usually used for the detection of sudden stratospheric warmings (SSWs, Butler et al., 2016). Outside this region differences between CMAM30 and MERRA2 grow. More pronounced differences can be observed during boreal winters, and zonal wind variability is enhanced during these periods.

From the climatological perspective, we compare CMAM30 temperature over the tropical and subtropical latitudes with SABER measurements and MERRA2 reanalysis. Figure 3.2 shows zonal mean of temperature climatology averages over the period 2006-2010 at 4 vertical levels, i.e. at 31, 51, 61 and 71 km, respectively. We observe that CMAM30 agrees very well with MERRA2 at 31 and 51 km. In

[6]While all REF-C1SD simulations available were provided for the period 1980-2010, EP divergence outputs of CNRM-CM5-3 were provided only for the period 1990–2010.

[7]Outputs for this variable were not provided via `https://www.earthsystemgrid.org/dataset/ucar.cgd.ccsm4.ccmi1.output.html`.

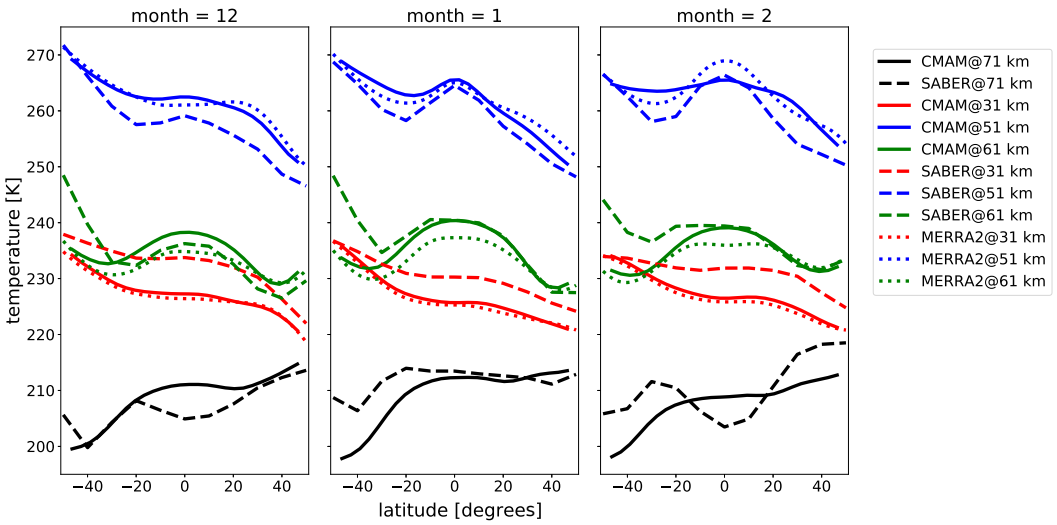

Figure 3.2: Zonal mean of temperature climatology over the period 2006-2010 in CMAM30 (solid lines), SABER (dashed lines) and MERRA2 reanalysis (dotted lines), respectively. Red, blue, green and black lines represent temperature climatology at 31, 51, 61 and 71 km, respectively.

comparison with SABER at 31 km, there is a bias ($\sim 4-5$ K) between SABER and CMAM30, and MERRA2 as well in all boreal months. In contrary to 31 km, at 51 km, we observe colder temperatures with SABER; another bias is apparent especially in December. These biases are in agreement with the evaluation by Remsberg et al. (2008) indicating excessively high temperature profiles in the lower stratosphere by 2-4 K and then excessively low by 1-3 K in comparison with lidar measurement. While at 31 km, the bias is apparent mainly in the tropics, at 61 km, we observe more significant temperature differences between SABER and CMAM30 in the subtropics of the southern hemisphere in all boreal months. These biases are also apparent in January and February at 71 km.

Next, we provide a comparison between absolute GW momentum fluxes estimated from HIRDLS and SABER measurement and produced by orographic and nonorographic parametrizations in CMAM30. In the figure 3.3 we focus only on boreal winter months and latitudes of the northern hemisphere in the lower stratosphere (at 30 km) where most of the GWD in CMAM30 is represented by oGWD. Although we observe that latitudinal variation is very similar between our model and the observations, i.e. being largest around 50°N, the climatological absolute GW momentum fluxes in CMAM30 overestimate quite significantly the climatology of absolute GW momentum fluxes from HIRDLS and SABER between 30 and 60°N in November, December and January. In February and March, there is a significant drop in the modelled GWD to more comparable amplitudes; however, the modelled peaky structure in February still overestimates HIRDLS and SABER fluxes by a factor of 2. At lower latitudes, where nonorographic GW fluxes contribute mostly, HIRDLS and SABER fluxes overestimate the values produced in CMAM30's parametrization. Comparing CMAM30 momentum fluxes with other models in Fig. 2 in Geller et al. (2013), we find a good agreement in terms of amplitude and latitudinal variation on both hemispheres. Geller et al. (2013) also documented in their Fig. 1 that absolute gravity wave momentum fluxes from HIRDLS or SABER are larger for the southern-hemispheric

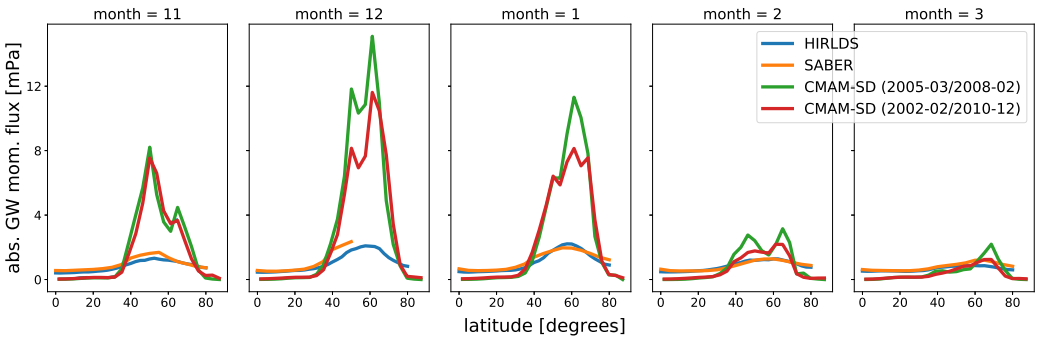

Figure 3.3: Climatologies for the absolute gravity wave momentum fluxes [mPa] at 30 km from CMAM30 averaged over the HIRDLS-like period, i.e. from March 2005 until February 2008, and over the longer period, i.e. from February 2002 to December 2010, respectively, compared with HIRDLS and SABER estimates from GRACILE.

winter than for the northern-hemispheric winter. Furthermore, they show similar overestimation for January 2006 in the northern hemisphere while for July 2006 in the southern hemisphere, models perform much better. Using this finding we compare austral climatology of CMAM30 momentum fluxes with observation in the southern hemisphere and we also find much better agreement, especially up to 60°S (not shown). This comparison between CMAM30 and HIRDLS or SABER estimates of absolute GW momentum fluxes indicates that the parametrization of oGW in CMAM30 is instead tuned to represent a missing drag in the southern hemisphere (McLandress et al., 2012) which results in the overestimation of the absolute GW momentum fluxes in the northern hemisphere as mentioned above (Garcia et al., 2017). Furthermore, Xu et al. (2017) and Xu et al. (2018) suggested that including the horizontal propagation and directional absorption of mountain waves in the parameterization of oGWD, respectively, reduce the excessively large mountain wave drag in the lower stratosphere of climate models.

These results indicate that CMAM30 provides a convenient dataset to study climate characteristics of zonal wind and temperature in the stratosphere since it is consistent with MERRA2 reanalysis mainly in the stratosphere, although there are biases identified in comparison with the measurements. While climatology GW momentum fluxes are not very aligned with the observation, the overall atmospheric variability due to orographic GWs in CMAM30 may vary in reality. In summary, we assume that CMAM30 is a reasonable tool providing freely-available outputs to study PW and GW characteristics in the 3D perspective on the lower stratosphere, in particular where the model nudging should ensure being close to reality because of assimilated-data density in respect to the upper levels.

3.4 Motivation

In this section we highlight the importance of orographic GWs, particularly in the lower stratosphere across state-of-the-art CCMs, which have dynamics specified by the reanalyses. Furthermore, we show the strong imporatance of oGWD in the lower stratosphere across all models. This facilitated the motivation of our study to investigate oGWD hotpots in the lower stratosphere, where the dynamics specified by the reanalyses do not show as substantial uncertainties as in the upper

stratosphere (Martineau et al., 2018).

Figure 3.4 shows the percentage contribution of the oGWD to the total wave drag (EPFD representing waves resolved by the model and total GWD) climatology in the northern hemisphere (NH) since we will investigate possible importance of oGWs and their hotspots in the context of NH SSWs (see Section 3.6.3). In the lower mesosphere, oGWD controls most of the total drag between 40 and 75°N in all months with the exception of the boreal summer months. Interestingly, oGWD constitutes another majority in the lower stratosphere between 25 and 50°N during boreal winter and its adjacent spring and autumn months. While it is also apparent in boreal summer, it is not constituted by oGWD in the majority. The similar constitution of GWs was partly discussed by Abalos et al. (2015) and also identified by Albers and Birner (2014) in their Fig. 2 using JRA-25 reanalysis when the contribution was composited with regard to split or displacement SSWs.

The contribution of orographic GWs to the total wave forcing may be sensitive to the model configuration, type of oGWD parametrization, its tunable parameters and simulated wind speed related to model resolution (Kruse et al., 2016). To document this sensitivity, we compare CMAM30 with other nudged models available from the CCMI-1 framework and with CMAM30-ext. We see that the majority of oGWD contribution to the total wave forcing in the lower stratosphere is strong across all models available (see Appendix A with Fig. A.1 showing two versions of EMAC-L90MA and EMAC-L47MA, respectively; CMAMs (CMAM-CCMI, CMAM30, CMAM30-ext); CCSRNIES-MIROC3.2, CNRM-CM5-3 and MRI-ESM1r1). On the other hand, the majority of oGWD in the upper stratosphere and lower mesosphere is robust during the whole boreal winter in the following models: CMAM (both non-extended versions), CCSRNIES-MIROC3.2 and CNRM-CM5-3. All EMAC model versions reveal this pattern only in the beginning of the boreal winter. MRI-ESM1r1 and CMAM30-ext consider the oGWD majority in the upper stratosphere only to a minimal extent in comparison to other models.

Figure 3.5 provides a comparison of the total GWD (oGWD+nGWD) of all models mentioned above with MERRA and MERRA2 at 70 hPa. All models overestimate total GWD by a factor greater than two from 30 to 70°N, i.e. at latitudes where oGWD almost entirely constitutes total GWD in all models available (not shown). It may correspond to the fact that the two-wave representation of momentum flux used in CMAM30 allows 30-50% more gravity-wave momentum flux up into the middle stratosphere than the single-wave representation (used in MERRA reanalysis, McFarlane, 1987), depending on the pressure level and season (Scinocca and McFarlane, 2000). The results by McLandress et al. (2013b) also suggest that the use of two waves to represent the full spectrum of orographic GWs has brought observations of mesospheric temperature, carbon monoxide and zonal winds into better agreement with Aura Microwave Limb Sounder (MLS) observations. Also, Kruse et al. (2016) have recently highlighted a smaller oGWD in the $12-27$ km layer of the Southern hemisphere in both MERRA datasets in comparison with 6-km-resolution WRF simulation. However, as shown in Fig. 3.5, the oGWD discrepancy is more significant in MERRA due to a lower intermittency factor south of approximately 40°S within the McFarlane (1987) parametrization. Furthermore, Scheffler and Pulido (2015) when analyzing MERRA analysis in-

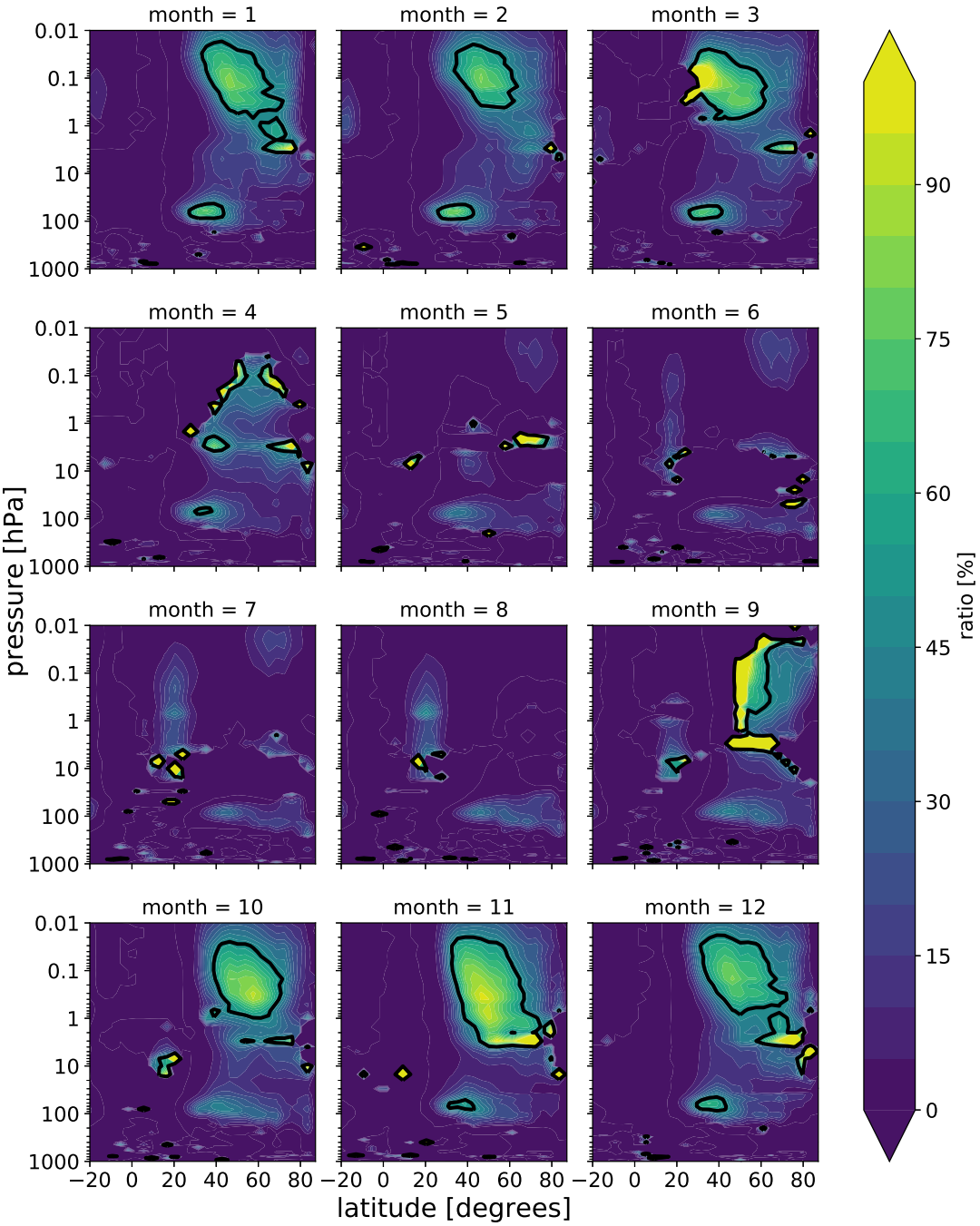

Figure 3.4: Percentage that orographic zonally averaged GWD (oGWD) in zonal direction contributes to the total wave forcing (resolved waves represented by EPFD + oGWD + nGWD) for the climatological average of the period 1979-2010. Black contour represents 50% contribution of oGWD. The latitudes are limited from 20°S to 90°N.

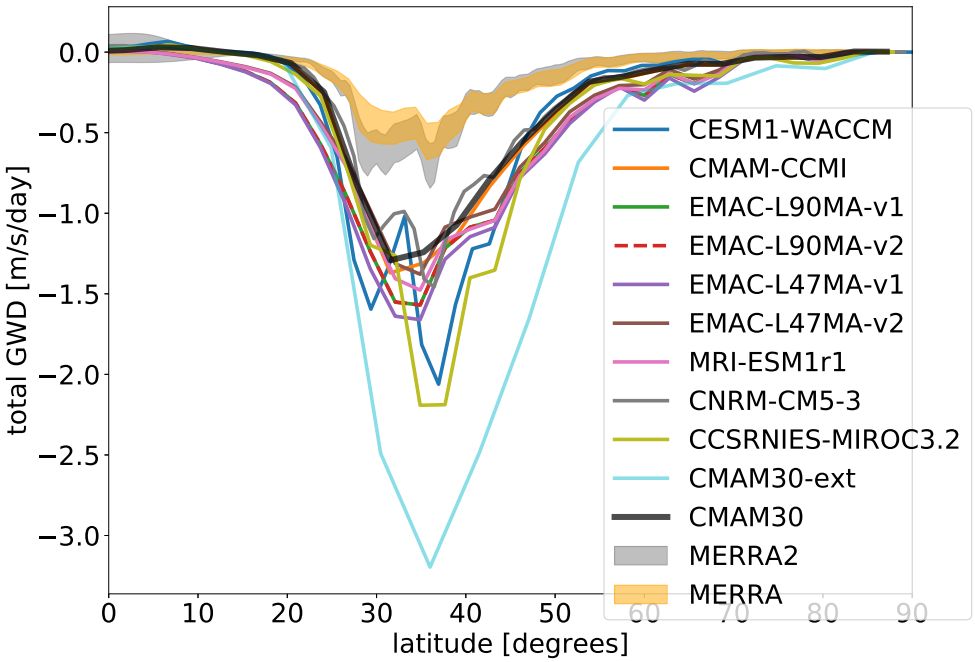

Figure 3.5: Climatology of total parametrized GWD [m/s/day] at 70 hPa in January averaged over the period 1990-2010. Gray and orange shading represent $\pm 1\sigma$ in MERRA and MERRA2 datasets. The latitudes are limited from 0°S to 90°N.

crements pointed out that the GEOS-5 GWD parametrizations do not produce enough deceleration in high latitudes of the southern hemisphere.

While CMAM30 and CMAM-CCMI reveal similar latitudinal GWD variation at 70 hPa as other models, the difference is apparent in terms of amplitude, with most of the other models overestimating these CMAM versions. In particular, CMAM30-ext reaches almost a tripled amplitude of GWD in non-extended CMAM versions. Although GWD in CMAM30 and CMAM-CCMI peak ~ 30°N, other models peak more northward (EMACs, MRI-ESM1r1 and CMAM30-ext) or reveal double-peaked behavior (CCSRNIES-MIROC3.2, CNRM-CM5-3 and CESM1-WACCM). Unfortunately, the findings above based on Fig. 3.5 do not allow remarks to be made about similarities in configurations of CCMI models.

From the zonal average perspective, total physics zonal wind tendency climatology in CMAM30 also reveals a hotspot in terms of a negative tendency in the lower stratosphere between 25 and 50°N. The zonal wind in this area is dragged down due to orographic gravity waves which constitute $\sim 100\%$ of zonally averaged zonal wind tendency climatology during the boreal winter in terms of the area highlighted above (not shown), i.e. in the lower stratosphere and in particular latitudes north of 20°N except for 80°N. These identified lower-stratospheric hotspots (in the zonal average so far) are located in the area of weak winds between the tropospheric and stratospheric jets. According to the theory (Teixeira, 2014) or lidar observation (Ehard et al., 2017), these areas, known as the valve layers (e.g., Kruse et al., 2016; Bramberger et al., 2017), with weak or zero horizontal winds provide critical levels to the stationary mountain waves where they break and therefore deposit horizontal momentum.

These areas reveal discrepancies between parameterized GWD and residual drag R from Eqs. 3.3 and 3.8 accounted from the zonal-mean momentum bud-

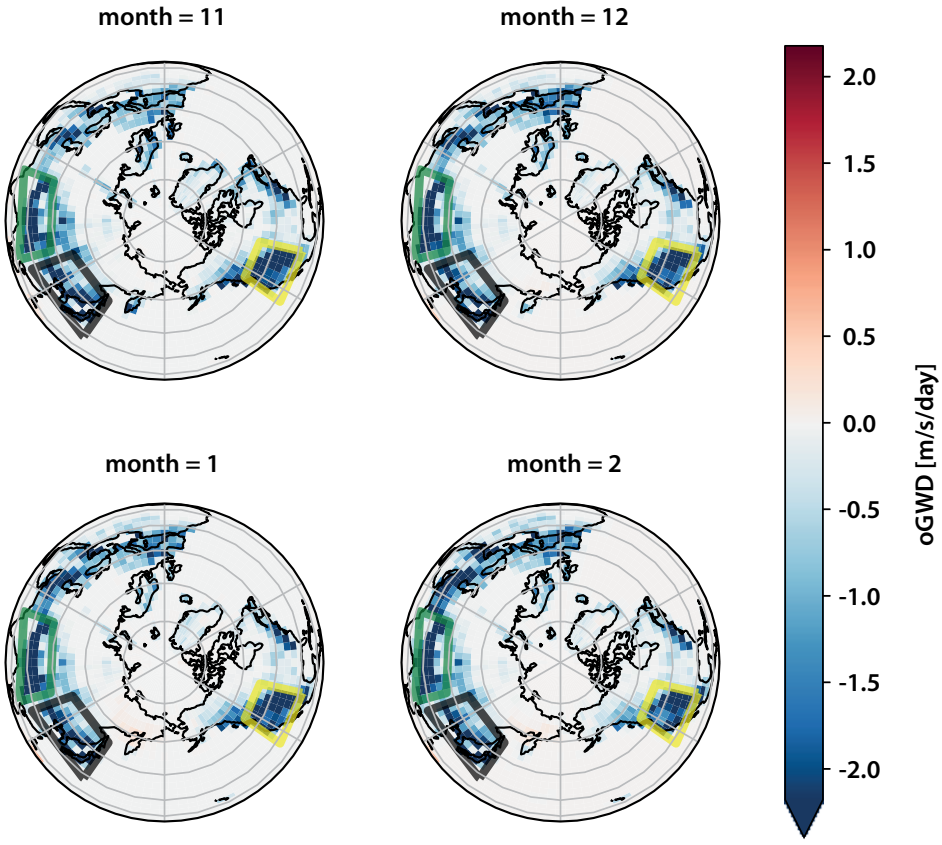

Figure 3.6: Climatological average maps of oGWD [m/s/day] at 70 hPa. We have placed colored boxed around GW hotspots contributing to high GW activity events. The green, black and yellow boxes represent the Himalayas, East Asia and West American hotspots, respectively.

get (for ERA-Interim; Seviour et al., 2012) and, e.g. for JRA-55 (see Fig. 2 in Martineau et al. (2016)). The orographic gravity wave drag parametrization included only in ERA-Interim perhaps underestimates the momentum deposited, particularly above 70 hPa. This discrepancy was partly attributed to a missing non-orographic gravity wave drag from convective sources (Kalisch et al., 2016). This discrepancy and its explanation is also valid for CMAM30 where, similarly to ERA-Interim, non-orographic GWD is almost zero in the lower stratosphere.

Horizontal distribution of the lower-stratospheric (70 hPa) oGWD climatology in Fig. 3.6, i.e. situated in the region where oGWD represents majority of the total drag in Fig. 3.4, demonstrates hotspots' behavior in the areas of the most apparent orographic features such as the Himalayas, the Mongolian plateau and the Rocky Mountains, respectively. The climatological dominance of these hotspots highlighted in Fig. 3.6 in the lower stratosphere has also been documented by Sacha et al. (2018). These orographically-induced GW drags may have their origin in high-wind speeds forcing so strong at the surface that the waves likely become unstable in the lower stratosphere (Kaifler et al., 2015).

Several studies have reported the importance of the East Asian region as a "vertical communicator" from the troposphere into the stratosphere (e.g. Naka-

mura et al., 2013; Cohen and Boos, 2017). The gravity-wave hotspot constituted by Eastern Asian orography or other possible sources (Šácha et al., 2015), e.g. a convective activity connected with the Kuroshio current, can generate zonally asymmetric GW breaking in the lower stratosphere (Šácha et al., 2016) and can play an important role in the PV stability. The presence of mountains can also change the wave propagation pathways through changes in the upper-tropospheric flow and consequently influence the frequency of SSWs (White et al., 2018, for the Tibetian and Mongolian plateaus). Furthermore, a detailed understanding of gravity-wave hotspots in observations (e.g. Hoffmann et al., 2013) or in models (e.g. Pisoft et al., 2018) can help to validate GW parametrizations in current or future CCMs.

3.5 Methodology

Motivated by the studies mentioned above, we will focus on the hotspots highlighted in the colored boxes in Fig. 3.6 and their influence on the PV geometry in respect to SSW and its impact on stratospheric ozone. Green, black and yellow boxes represent the Himalayans (80-102.5°E and 20-40°N), East Asian (110-145°E and 30-48°N) and West American (235-257.5°E and 27.5-52°N) hotspots, respectively. The area-weighted average of grid points within these areas resulted in time-series of oGWD representing the particular hotspots. These time-series were further resampled from 6-hourly model outputs to daily outputs.

In Fig. 3.7 we see that oGWD is generally small during the summer and large during the winter, since the westward gravity wave drag is mainly determined by the near-surface wind speed and its direction relative to the orientation of the subgrid topography (McLandress et al., 2013a; Sacha et al., 2018). During the winter, a peaky structure is apparent in all hotspots' time-series. Therefore, to characterize these peaky events, we apply a peak-detection algorithm with a minimum distance of 20 or 30 days and a normalized threshold of 0.55. The normalized threshold accounting for the time-series range is different for each GW hotspot, i.e. it is 6.66 m/s/day for the Himalayas, 5.07 m/s/day for East Asia and 7.13 m/s/day for West America, respectively. However, higher-order values can be seen in particular grids; the threshold values shown above represent the area-weighted average. The 20- and 30-day time-scale was selected to be consistent with the definition of a simplified version of the World Meteorological Organization (WMO) criteria for SSW detection proposed by Charlton and Polvani (2007) and split and displacement SSW events employed in Seviour et al. (2013), respectively. The number of days with detected events for both time-scales is 45 and 38 for the Himalayas, 74 and 66 for East Asia, and 36 and 35 for West America. Since the differences between these two timescales in the resulting composites are negligible, we will further discuss only composites regarding the 20-day timescale. The identified threshold contributed to the composite's construction when the relative change of the particular variable was averaged according to the days preceding the identified peak events (averaged over lags -10 to -1) and the days following the identified peak events (averaged over lags +1 to +10).

All outputs produced (i.e. time-series used for compositing, lists of detected peak events and files consisting composite averages for a particular model or calculated variable) are provided via the Mendeley Data portal (Kuchar, 2018).

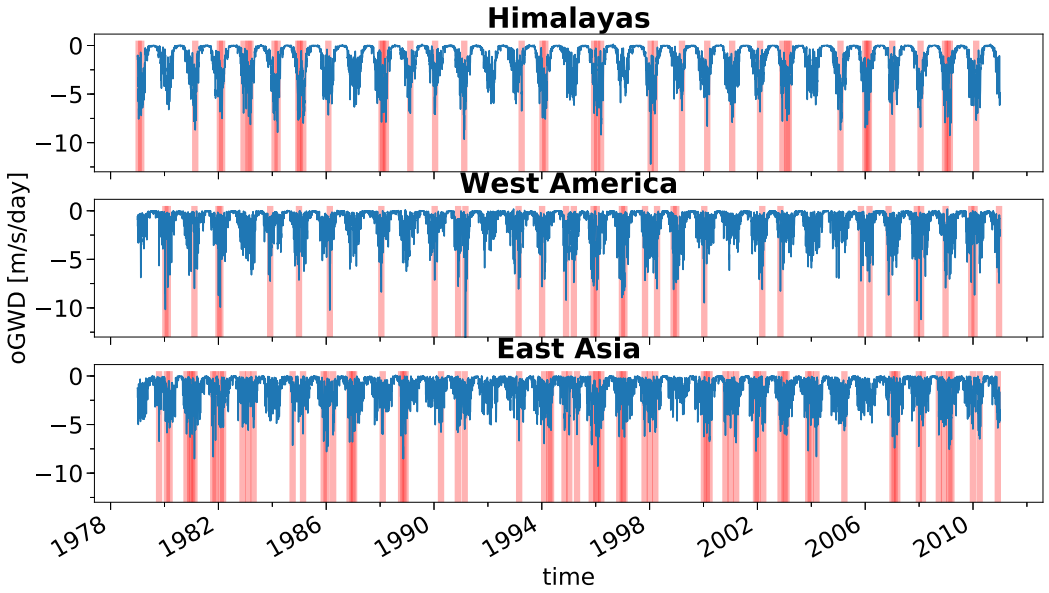

Figure 3.7: Area-weighted average of daily oGWD within areas representing the Himalayas (upper panel), West America (middle panel) and East Asia (lower panel). Peak events with 20-day time-scale are highlighted by pink bars. See the interactive figures folder in Kuchar (2018) for interactive plots.

3.6 Results

In the following section we examine the composite responses of temperature, zonal wind and ozone to oGW forcing in the lower stratosphere. Since oGW breaking is localized from the nature of the matter, we highlight the localized response of these standard variables in addition to zonal-mean plots. These responses will be put into context with dynamical diagnostics particularly in section 3.6.2.

3.6.1 Temperature, zonal wind and ozone response

Figure 3.8 shows the zonal mean of temperature anomalies composite average at lag=0 for all hotspot regions in the lower stratosphere. While negative temperature anomalies in the lower mesosphere ($> 3\,\mathrm{K}$) and upper stratosphere extended north of 50°N are common for all composites, below 10 hPa a positive temperature up to 3 K is only apparent in the composite representing the Himalayan region. The composites representing the East Asian and West American regions do not reveal such a significant positive anomaly in these stratospheric layers. However, in the composites representing the East Asian and West American region, the positive response is shifted to the troposphere; however, in the case of the West American region there is a more pronounced positive anomaly in the polar troposphere up to 300 hPa.

These temperature anomalies are consistent with the composited zonal wind field through thermal wind balance. In Fig. 3.9, we can see zonal wind strengthening in the lower mesosphere with a maximum around 50°N in all regions in contrary to the stratosphere, where the weakening prevails especially in the composites representing the Himalayas and West American regions, respectively. Another common feature for all composites is the zonal-wind enhancement in the troposphere just below the oGWD hotspot area at 70 hPa. As regards strictly

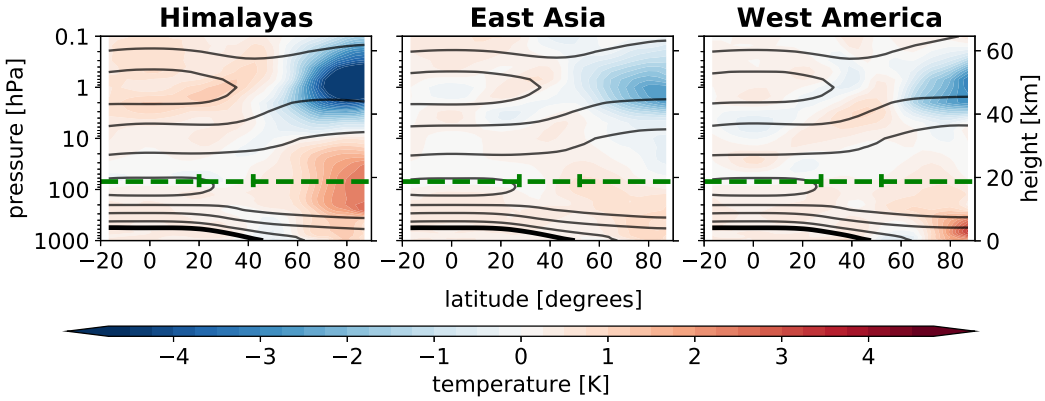

Figure 3.8: Zonal mean of temperature anomalies (shading; units: K) and absolute (contour levels: $200, 220, 240, 260, \mathbf{273.15}$ K) composite average at lag=0 representing the Himalayas (left panel), East Asian (middle panel) and West America (right panel). Green horizontal and vertical lines represent regions with a particular GW hotspot.

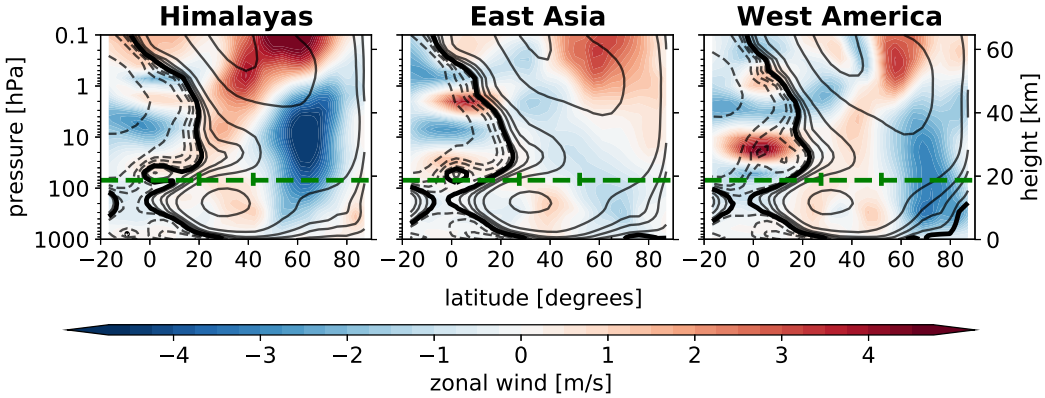

Figure 3.9: Zonal mean of zonal wind anomalies (shading; units: m/s) and absolute (contour levels: $\mathbf{0}, \pm1, \pm3, \pm5, \pm10, \pm30, \pm50, \pm80$ m/s) composite average at lag=0 representing the Himalayas (left panel), East Asia (middle panel) and West America (right panel). Green horizontal and vertical lines represent regions with a particular GW hotspot.

vertical fluxes from the oGW parametrization, the strengthening of zonal wind in the troposphere may be preconditioning the oGWD events, while zonal winds above or poleward of a hotspot area can not directly influence this preconditioning.

Figure 3.10 shows that the temperature response at 70 hPa is localized above all regions, i.e. we observe positive temperature anomalies poleward from the GW forcing averaged within particular area (see green boxes in Fig. 3.10) to higher latitudes, with the exception of the West American composite, where the positive temperature response is highly localized on the northwest of America, and negative temperature anomalies southward from the forcing areas.

Zonal wind strengthening (around lag=0, see red shading in Fig. 3.11) above a complete or partial composited area is prevalent throughout all pressure levels up to the lower mesosphere for the Himalayas and North American regions (see Figs. B.1 and B.3). For the East Asian region (see Fig. B.2), we instead observe zonal wind weakening throughout the stratosphere. This zonal wind strengthening is associated with enhanced westward propagating GWs in the lower stratosphere within all our composited regions (see oGWD profiles across all lags in Fig. 3.12

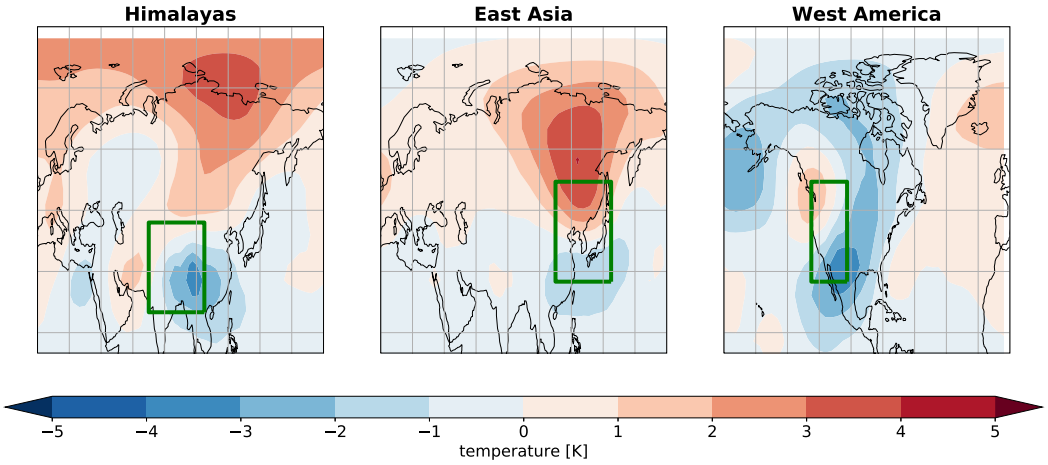

Figure 3.10: Temperature anomalies [K] composite average at lag=0 and 70 hPa representing the Himalayas (left panel), East Asia (middle panel) and West America (right panel). Green boxes represent regions with a particular GW hotspot.

or additionally maps for particular pressure levels in Figs. B.4, B.5 and B.6 in the Appendix). The enhanced westward propagating orographic GWs repeat in the lower mesosphere except for East Asia, where the propagation of orographic GWs is suppressed due to zonal wind filtering. The amplitude of negative oGWD anomalies around lag=0 in Fig. 3.12 is strongest above West America at 70 hPa ($\sim$ 7 m/s/day) as well as in the lower mesosphere ($\sim$ 17 m/s/day). These findings that gravity wave propagation is associated with strong zonal wind are in agreement with Albers and Birner's 2014 analysis of oGW propagation in JRA-25 and ERA-Interim reanalyses. Under these conditions, GWs with westward or zero ground-based phase speeds can propagate this whole-altitude range without encountering any critical level and consequently can be Doppler-shifted to large amplitudes as observed based on satellite instruments HIRDLS and SABER by Ern et al. (2016). The zonal wind strengthening in Fig. 3.11 is associated with negative anomalies of LWA (dashed contours in Fig. 3.11), particularly for the Himalayan and West-American composites. On the other hand, the deceleration of local zonal wind is correlated with positive anomalies of LWA (solid contours in Fig. 3.11). Overall, this may indicate local negative feedback between large-scale waves represented by LWA and in this case oGWs which are enhanced due to the zonal wind acceleration at the expense of LWA.

Figure 3.13 shows zonally averaged ozone anomalies in percents during the peak event, i.e. at lag = 0, for all regions composited. All regions reveal a positive ozone anomaly around the polar stratopause, i.e. around 1 hPa poleward from 50°N. In the middle and lower stratosphere, we observe a pronounced positive ozone anomaly poleward from 60°N in the Himalayas composite. The East Asian ozone composite results in the opposite anomaly extending from 2 hPa to 300 hPa. In the West American composite, we find a less pronounced positive response from 10 hPa to 100 hPa changing in the negative ozone anomaly between 100 hPa and 400 hPa in the zonal average. In comparison with the temperature response, in the lower stratosphere the ozone responds with the same sign in the case of the Himalayas and East Asia. In the case of the West American region, the temperature and ozone response, albeit with smaller amplitudes, is the opposite.

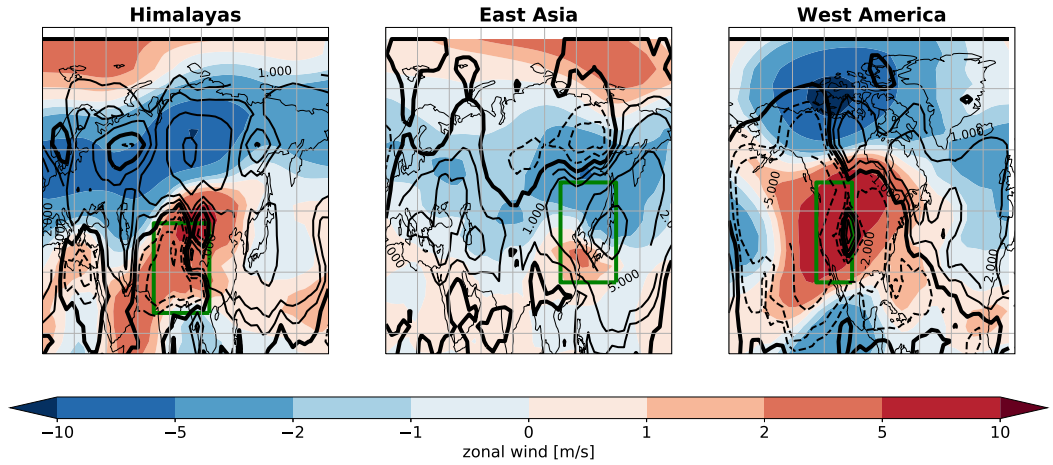

Figure 3.11: Zonal wind anomalies (shading; units: m/s) composite average and 70 hPa and LWA (contours; units: m/s) at 18 km both at lag=0 representing the Himalayas (left panel), East Asia (middle panel) and West America (right panel). Green boxes represent regions with a particular GW hotspot.

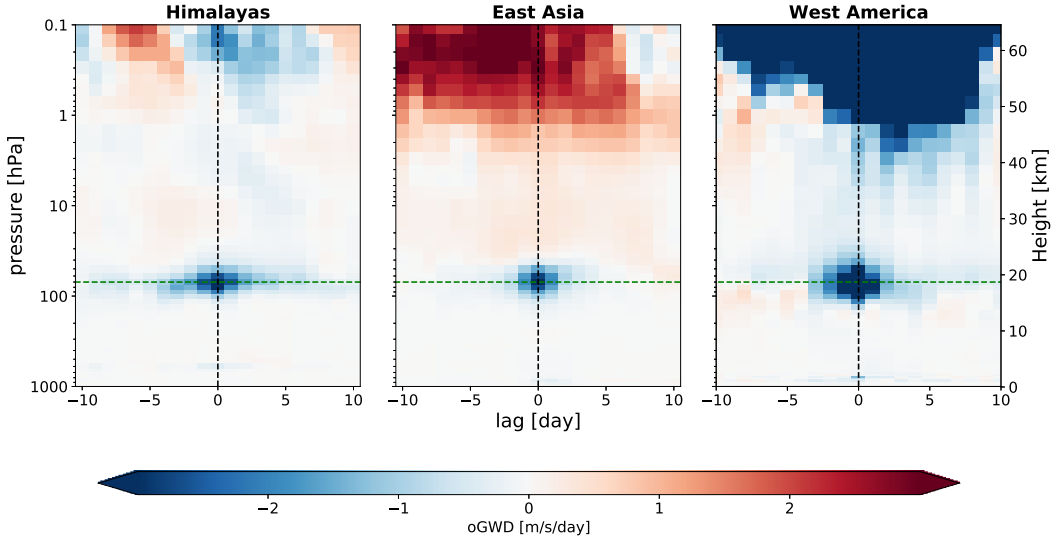

Figure 3.12: oGWD anomalies [m/s/day] composite average at all lags up to 0.1 hPa averaged within lat-lon boxes representing the Himalayas (left panel), East Asia (middle panel) and West America (right panel). Green lines represent the composite level, i.e. 70 hPa.

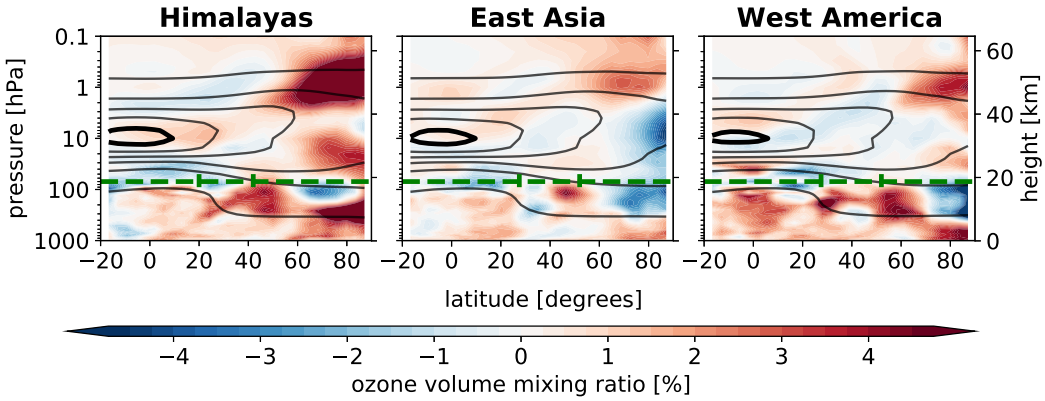

Figure 3.13: Ozone anomalies (shading; units: %) and absolute (contour levels: $1 \cdot 10^{-7}, 2 \cdot 10^{-6}, 4 \cdot 10^{-6}, 6 \cdot 10^{-6}, 8 \cdot 10^{-6}, \mathbf{1 \cdot 10^{-5}}$ mole/mole) composite average at lag=0 representing the Himalayas (left panel), East Asia (middle panel) and West America (right panel). Green horizontal and vertical lines represent regions with a particular GW hotspot.

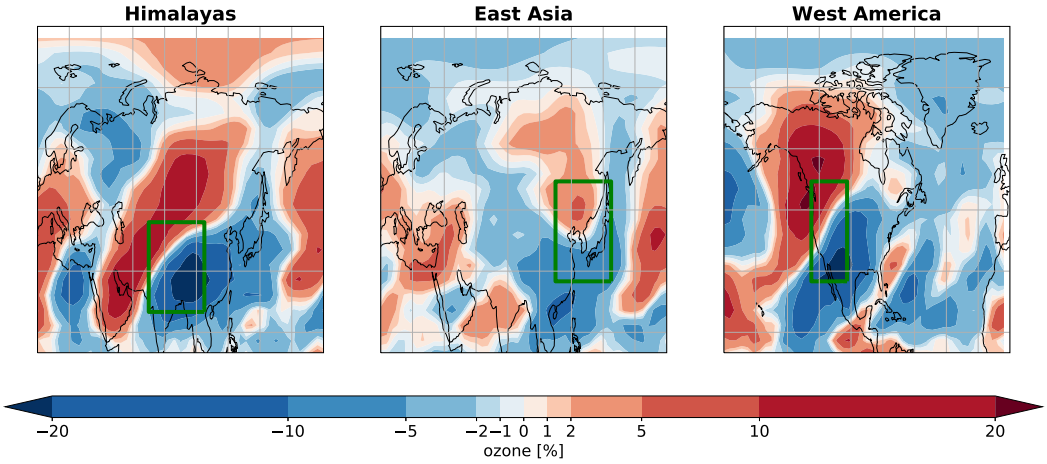

Figure 3.14: Ozone anomalies [%] composite average at lag=0 and 70 hPa representing the Himalayas (left panel), East Asia (middle panel) and West America (right panel). Green boxes represent regions with a particular GW hotspot.

Since zonal averaging may mask the localized response, as already shown in the case of temperature and zonal wind, in terms of ozone, this fact is valid as well. The ozone response correlates quite strongly with the temperature response at 70 hPa (see Fig. 3.14), i.e positive and negative ozone anomalies on the north and south edges of the composite region, respectively. Note that the positive ozone anomaly north of the East Asian bounding box is really masked in the zonal average. This correlation in the dynamically controlled lower stratosphere may be attributed to the enhanced residual mass transport poleward with an enhanced upwelling and downwelling in lower and higher latitudes, respectively (see Section 3.6.2 for further discussion).

3.6.2 Dynamical effects discussion

To diagnose the residual mass transport (Brewer-Dobson circulation), we use transformed Eulerian-mean (TEM) momentum equations (Andrews and McIntyre, 1987). Furthermore, we use the Eliassen-Palm flux framework to analyze the

resolved wave's forcing and its potential impact on the residual circulation (Andrews and McIntyre, 1987). Figure 3.15 shows the Eliassen-Palm flux divergence (EPFD; color shading), vertical and meridional components of residual circulation (arrows) and zonally averaged oGWD (gray contours) for all composited regions at lag=0. While in the lower mesosphere, we observe positive anomalies of EPFD and oGWD in all composites, and therefore suppressed meridional transport from lower latitudes to higher latitudes due to both resolved and gravity waves, in the stratosphere we observe opposite signals only in EPFD especially between the Himalayan and West American composites. The negative EPFD anomaly in the composite representing the Himalayan region induces the enhanced meridional transport via the downward control principle (Haynes et al., 1991). By the continuity equation, the enhanced meridional transport is associated with the enhanced upward motion at around 40°N and consequently with the downward motion in polar latitudes. These enhanced vertical motions are tied to positive temperature changes in the lower stratosphere in Fig. 3.8 via the thermodynamic equation. On the other hand, the positive EPFD anomaly in the composite representing the East-Asian region induces weaker residual circulation in higher latitudes. The residual circulation has a similar response in the West-America composite, however, the weakening of the residual circulation is more significant in higher latitudes of the whole stratosphere and lower mesosphere. To summarize, at higher latitudes in the stratosphere the residual response more significantly copies the anomalous resolved wave forcing than oGWD in the zonal average.

The temperature response has the same sign as the ozone in the lower stratosphere — especially apparent for the Himalayan composite. Contrary to the lower stratosphere, in the lower mesosphere the temperature and ozone response is opposite. It is possible that the negative temperature transport-induced anomaly in the lower mesosphere influence has the temperature feedback effect on ozone photochemistry in these pressure levels where the ozone cannot be controlled dynamically due to the ozone chemical lifetime. Furthermore, similar dynamically induced changes in the lower-mesosphere, where ozone chemistry by HO_x-driven catalytic cycles dominates (Brasseur and Solomon, 2006), may be seen in the HO_x volume mixing ratio. HO_x anomalies correlate with temperature and ozone in the lower stratosphere when changed to the anticorrelation with ozone in the upper stratosphere and lower mesosphere (not shown).

The negative EPFD anomaly for the Himalayas composite at lag=0, i.e. enhanced breaking of the resolved waves, is due to the enhanced vertical wave propagation represented by the positive anomalies in the vertical EP flux component (see Fig. 3.16). These positive anomalies extend from 25°N to 75°N in the lower stratosphere; however, the highest amplitudes can be seen north of the composite bounding box, i.e. north of 40°N. The EP fluxes exhibit bifurcation and polar focusing — see arrows split into two separate branches in the lower stratosphere, one going equatorward and one continuing more vertically (cf. with Fig. 13 in Matsuno (1970)). The enhanced wave breaking, i.e. negative anomalies of $\nabla \cdot \vec{F}$ (blue shading in Fig. 3.15) and the positive values of the zonal mean of LWA tendency A_t (solid contours in Fig. 3.16), have an impact on the zonal wind circulation as well, see negative anomaly in the left panel of Fig. 3.9. Note that from 8 to 2 days preceding the peak event, we detect the suppressed ver-

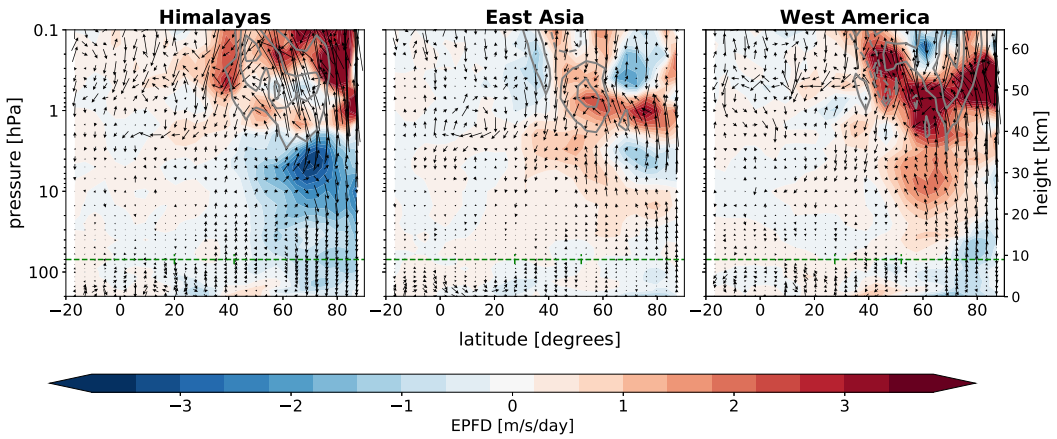

Figure 3.15: Zonal plot of Eliassen-Palm flux divergence $\nabla \cdot \vec{F}$ (shading; units: m/s/day), zonally averaged oGWD (gray solid contours for positive anomalies and gray dashed contours for negative anomalies; units: m/s/day) and $\{\bar{v}^*, \bar{w}^*\}$ velocities (arrows; units: m/s for meridional and 10^{-3} m/s for vertical velocity) composite average at lag=0 representing the Himalayas (left panel), East Asia (middle panel) and West America (right panel). Green horizontal and vertical lines represent regions with a particular GW hotspot.

tical propagation and poleward reflection of resolved waves. The same EP flux response is actually valid at lags around 0 for the East Asian and West American composites. Positive anomalies of $\nabla \cdot \vec{F}$ (red shading in Fig. 3.15) and negative values of zonal mean of LWA tendency A_t (dashed contours in Fig. 3.16), instead influence the residual circulation since the stratospheric zonal wind also reveals negative response.

Using zonally averaged LWA, we gain finite-amplitude wave activity (Nakamura and Solomon, 2010; Huang and Nakamura, 2016). The tendency of this variable in addition to EP flux divergence is related to the nonconservative sources-sinks of wave activity (see Eq. 3.7). The changes in the source-sink term can be attributed to the changes in effective diffusivity of the irreversible mixing of PV across its own contour (Nakamura, 1996) and changes in the source-sink of wave activity as a result of diabatic heating/cooling averaged over the azonal area of PV (Nakamura and Zhu, 2010b; Lubis et al., 2018). As reported by Martineau and Son (2015) and Lubis et al. (2018) the anomalous sink of wave activity in the stratosphere tends to slow down the vortex recovery (strengthening or positive wind tendency) after SSW-like events[8], in accordance with what we observe in the Himalayan composite (see positive anomalies of wind tendency in the left column of Fig. 3.16 pronounced in the upper stratosphere) while East Asian and West American composites instead reveal positive anomalies, i.e. sourcing of wave activity in the stratosphere (not shown) and consequently positive feedback on the polar vortex (see positive anomalies of wind tendency in the middle and right columns of Fig. 3.16).

As mentioned in Section 3.6.1 the temperature, zonal wind and ozone response is zonally asymmetric. Therefore, as a proxy for the vertical wave propagation we use the three-dimensional expansion of the two-dimensional EP flux derived by Plumb (1985). Figure 3.17 shows the vertical component of anoma-

[8]Note that events (-NAM SVW (stratospheric vortex weakening)) introduced by Martineau and Son (2015) are essentially the same as classical SSWs just with different temporal alignments.

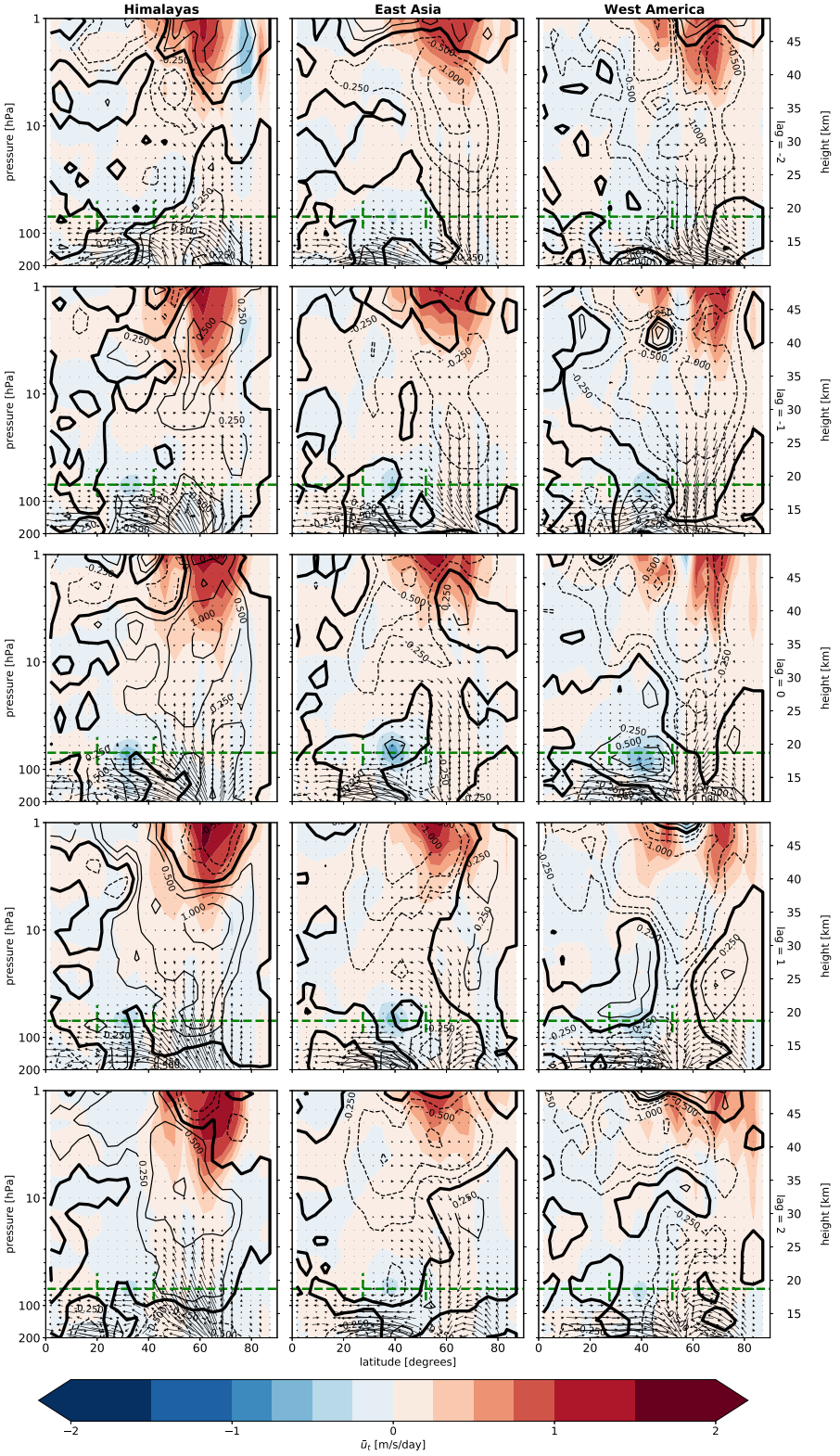

Figure 3.16: Eliassen-Palm flux $\vec{F}$ (arrows; units: $(1;10^{-2})$ kg/s/s), total physics zonal wind tendency $\bar{u}_t$ (shading; units: m/s/day) and zonal mean of local wave activity tendency A_t (contours; units: m/s/day) composite averages at lags=$\{-2;2\}$ days representing the Himalayas (left panels), East Asia (middle panels) and West America (right panels). Green horizontal and vertical lines represent regions with a particular GW hotspot.

lous (shading) and absolute[9] (black contours) Plumb flux composite averages at lag=0 representing the Himalayas (left panels), East Asia (middle panels) and West America (lower panels). Absolute composite values including climatology of the vertical Plumb flux highlight that resolved waves propagate almost entirely upward and mainly over Eurasia with an enhancement over East Asia and the western North Pacific (EANP), i.e. over the region where the orographic forcing is particularly strong and land-sea heating contrast is also strong (Nakamura et al., 2013). The wave-1 pattern including the upward wave propagation over the EANP and downward wave flux over North America and the North Atlantic, although with smaller amplitudes in comparison with upward fluxes, may constitute important features in the troposphere-stratosphere and stratosphere-troposphere coupling, respectively (Zyulyaeva and Zhadin, 2009; Ke and Wen, 2012). Vertical Plumb flux is anomalously enhanced in the EANP during the events composited above West America changing to a negative anomaly over Alaska. On the orther hand, for the Himalayan and East Asian composites, the vertical Plumb flux in the EANP is anomalously weaker. This may be considered as an emerging mechanism of compensation between resolved and unresolved drag in terms of their sourcing in the troposphere. Note that for the Himalaya,s the enhancement is located over central Siberia for all pressure levels displayed in Fig. 3.17.

3.6.3 Possible links to SSWs

Cohen et al. (2014) suggested that the importance of GWD is primarily in how they help shape the width and depth of the surf zone. Furthermore, they highlighted the importance of GW perturbation outside of the surf zone causing non-local interactions with the resolved waves through the polar vortex weakening. This enhances upward planetary wave propagation according to the Charney-Drazin criterion (Charney and Drazin, 1961) and this consequently leads to an enhancement of resolved wave breaking represented by the negative EPFD response. This mechanism's features resemble the Himalayan peak events composite — the changes in the resolved waves amplifies the residual circulation (see left panel in Fig. 3.15) and consequently leads to a warming in the polar latitudes of the lower stratosphere. This mechanism is not necessarily compensating since oGWD up to $-1\,\mathrm{m/s/day}$ at 70 hPa and lag=0 is compensated by EPFD up to $0.25\,\mathrm{m/s/day}$, which is approximately in agreement with the compensation measure $C = 0.21 \pm 0.04$ in Cohen et al. (2014).

Many studies have shown that SSW events are associated with deceleration of the polar vortex and enhanced residual circulation caused by the wave forcing in the stratosphere (e.g. Martineau and Son, 2015). Pfeffer (1992) suggested that while changes in the shape and intensity of the zonal wind are positively correlated with the divergence of the horizontal component of the EP flux, negative changes in the divergence of the vertical component of the EP flux imply positive changes in the residual circulation. It has been further documented that the forcing by resolved waves represented by the EP flux divergence plays a primary role in the stratosphere (e.g. Alexander, 2010, and references therein); however, GWD produces a smaller contribution to the residual circulation than EPFD (e.g. Song

[9]These values represent composite average when climatology was not subtracted as in case of anomalous values.

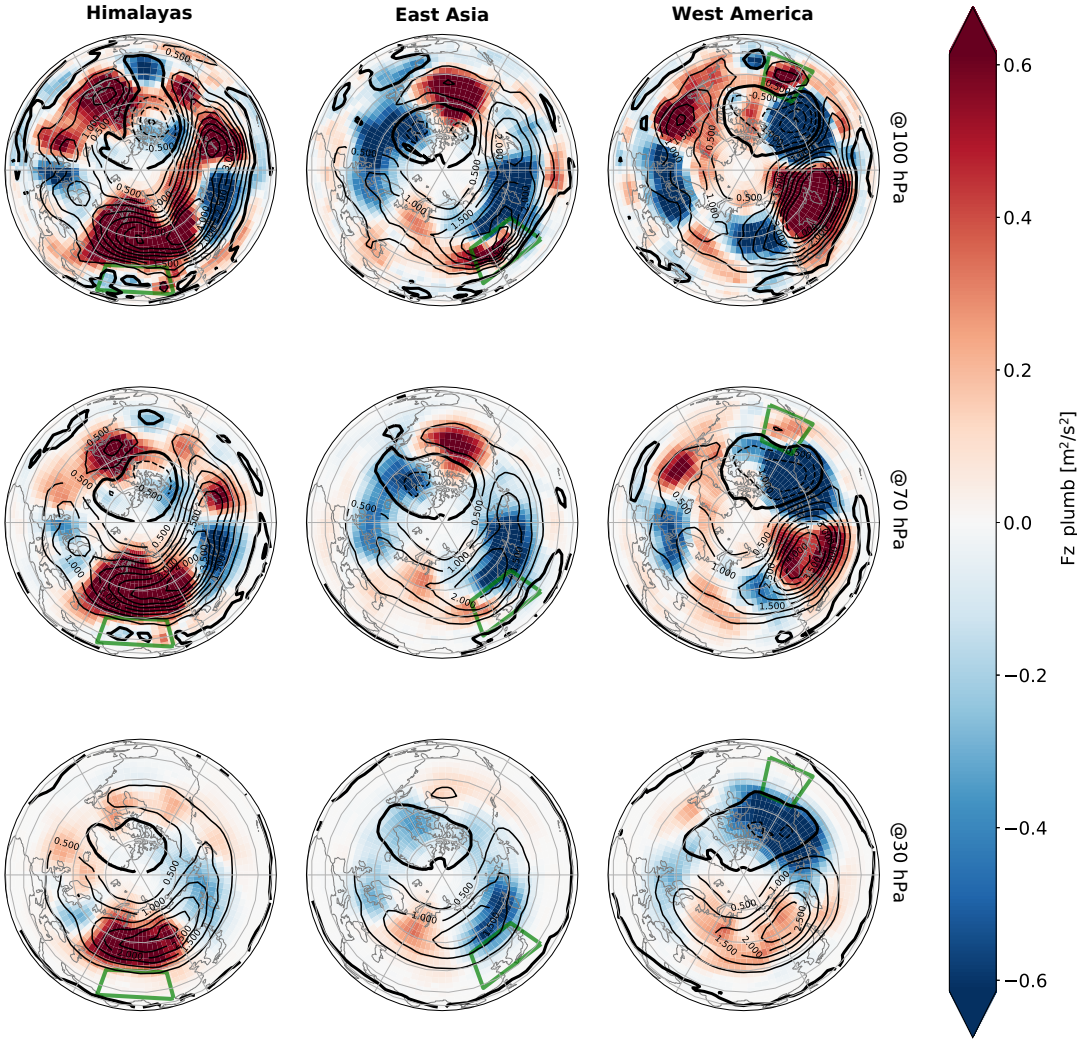

Figure 3.17: Vertical component of anomalous (shading; units: m^2/s^2) and absolute (black contours, solid contours for positive values and dashed for negative values when zero contour is shown by bold contour; units: m^2/s^2) Plumb flux composite averages at lag=0 representing the Himalayas (left panels), East Asia (middle panels) and West America (lower panels). Maps in Orthographic projection show vertical Plumb flux at $\{100; 70; 30\}$ hPa. Green boxes represent the Himalayan (left column), East Asian (middle column) and West American hotspots (right column), respectively.

and Chun, 2016). Based on our findings and findings by Albers and Birner (2014) that in addition to breaking PWs in the surf zone, GWs also play an important role in vortex preconditioning (i.e. triggering an SSW) we hypothesize that an imposed drag in the lower-stratosphere by an orographic hotspot (although much weaker in comparison with the mesospheric drag) located on the edge of the surf zone may be influential in the heat and ozone transport to higher latitudes as mainly documented during SSWs. However, for a causality confirmation, it is necessary to use a model with similar complexity (White et al., 2018) or mechanistic GCM (Šácha et al., 2016).

Another possibility how Himalayan peak events in terms of parametrized oGWs can be linked to SSWs is a synoptic situation leading to oGWs generation on the Himalayan range and simultaneously to anomalous upward wave propagation over Siberia identified as a precursor of SSW and negative surface AO, e.g. in Cohen and Jones (2011) (cf. their Fig. 3 with left panels in Fig. 3.17). This precursor is associated with a strengthened Siberian high and with a deepened Aleutian low in the case of vortex displacements only. Both pressure anomalies can be detected for the Himalayan composite in our case as well (not shown). The amplification of the cold Siberian high is associated with meridional heat transport which is projected into the upward wave propagation (Takaya and Nakamura, 2005).

3.7 Conclusions

This study focuses on the role of orographic gravity waves parametrized in the lower stratosphere in the CMAM30 model. Firstly, we compare absolute gravity wave momentum fluxes from CMAM30 with the novel dataset GRACILE and show that these fluxes are overestimated during the boreal winter in the middle latitudes. We suggest that these differences may be explained by the fact that the parametrization of oGWs is tuned instread to represent the GWD in the southern hemisphere resulting in the overestimation in the northern hemisphere. In addition, using horizontal propagation and directional absorption of mountain waves in the parametrization may bring the GWD in the middle latitudes closer to the observation (Xu et al., 2017, 2018). These findings moderated by an underestimation of the GW momentum fluxes from the satellite observation (Ern et al., 2018), may document possible deficiencies of current GCMs not resolving GWs explicitly.

Despite this possible discrepancy, the parametrization of oGWs in CMAM30 deposits horizontal momentum in the lower stratosphere between the tropospheric and stratospheric jets in agreement with the theory of mountain wave breaking (Teixeira, 2014) and lidar observation (Ehard et al., 2017). Climatological dominance of oGWs in these areas known as the valve layers (Kruse et al., 2016) were examined across all REF-C1SD simulations within the CCMI framework. We have shown that CMAM30 reveals a conservative behavior in terms of: latitudinal variation peaking around 30°N in contrast to a double-peaked variation in CESM1-WACCM, for instance, and amplitude in contrast to other models mostly producing higher values of total parametrized GWD between 30–40°N during the boreal winter.

Using the locally identified time-series within these "valve" areas (at 70 hPa)

and a peak-detection algorithm to composite an averaged climate state during the oGW breaking above the Himalayas, East Asia and West America, we discussed basic climate characteristics such as temperature, zonal wind and ozone mixing ratio. In addition to fundamental 2D frameworks for discussion of planetary waves and Brewer-Dobson circulation such as the EP flux diagnostic and components of residual circulation, we used other variables allowing the discussion of dynamical effects in more detail, i.e. LWA and 3D Plumb flux diagnostics. These diagnostics were helpful to reveal common features of the Himalayan composite with the SSW events when the residual circulation is amplified by an enhanced resolved wave breaking, leading to a warming and ozone enrichment in the polar latitudes of the lower stratosphere. This enhanced resolved wave breaking is a response of the polar vortex weakening allowing more upward planetary wave propagation. This anomalous resolved-wave propagation is concentrated over Siberia, and was previously identified as the SSW precursor in Cohen and Jones (2011) associated with the Siberian-high strengthening. Furthermore, the identified anomalous sink of wave activity in the stratosphere tends to slow down the PV recovery after SSW-like events as reported previously by Martineau and Son (2015) and Lubis et al. (2018). These findings suggest that an orographic hotspot with highly localized gravity wave forcing on the edge of the surf zone such as the one above the Himalayas may be influential in heat and ozone transport to the higher latitudes.

The impact of the imposed oGWD above the Himalayas was instead explained using the theory based on zonal means. After all, compensation mechanisms are discussed in Cohen et al. (2014) in the same way. This approach may be reasonable for the momentum deposition by large-scale waves as observed in case of the Himalayan composite. However, in general this approach is not appropriate when studying the response to momentum deposition associated with oGWs (Shaw and Boos, 2012) since these forcings are inherently zonally asymmetric (Šácha et al., 2016). Therefore, it is possible that this explains why the East Asian and West American composites do not reveal such responses compliant with the classical paradigms assuming zonally symmetric torques and do not allow the discovery of common features with SSW events, however, they reveal zonally asymmetric response in temperature and ozone.

In future work, we shall prove the causality link from Section 3.6.3 hypothesizing that an imposed drag in the lower stratosphere by an orographic hotspot located on the edge of the surf zone may influence the polar night jet and consequently the heat and ozone transport in the stratosphere and even in the lower mesosphere. For the causality confirmation, we plan to use a mechanistic GCM similar to Šácha et al. (2016).

Conclusion

This chapter provides a brief summary of each chapter and suggestions for extension and continuation of out research.

The nonlinear character of the climate system highlighted in the Chapter 1 suggests potential benefits from the application of fully nonlinear attribution techniques to study interactions in the atmosphere. We attributed the variability of temperature, ozone and circulation patterns in the stratosphere and lower mesosphere with regard to the 11-year solar cycle using multiple nonlinear techniques (support vector regression and neural networks) besides the multiple linear regression approach. The results obtained by standard multiple linear regression were confirmed by the nonlinear approaches in all reanalyzed data sets on monthly timescale, suggesting that the linear regression is a relevant tool to sufficiently resolve the solar signal in the middle atmosphere. However, it needs to be used with caution and its limitations need to be properly discussed in the scientific literature. Incorrect attribution could, in essence, lead to incorrect conclusions about top-down mechanisms of the stratosphere-troposphere coupling. The seasonal evolution of the solar response was also discussed in terms of dynamical links in the winter hemispheres. The hypothetical mechanism of a weaker Brewer-Dobson circulation at solar maxima was reviewed in the MERRA reanalysis together with a discussion of polar vortex behaviour.

The Chapter 2 discusses the double-peaked response of the tropical stratospheric temperature profile to the 11-year solar cycle that has been described in the Chapter 1. There have been concerns about the origin of the lower peak due to potential aliasing with volcanic eruptions or the ENSO. By using the SOCOL CCM sensitivity simulations, we explain and quantify how the solar signal in the tropical lower stratosphere (TLS) was affected by volcanic eruptions and ENSO events during the past 50 years. The fact that the annual temperature response to the SC in the TLS was not detected implies that the temperature response in the TLS may be induced only in winter by a weaker BDC (Kodera and Kuroda, 2002); the solar signal propagates downward via the equatorial route (Simpson et al., 2009), or via the polar route (Kodera, 2005), or through a combination of these two (Kidston et al., 2015). These hypotheses need further investigation using longer CCM simulations with a sufficient number of ensemble members to minimize the internal variability component (Sukhodolov et al., 2017).

The Chapter 3 examines the role of parametrized oGWs in the lower stratosphere in the CMAM30 model with dynamics specified by ERA-Interim reanalysis. To inspect if CMAM30 suits for studies of dynamical forcing by planetary or gravity waves, the model was evaluated against the new observation dataset GRACILE in terms of absolute gravity wave momentum flux in the boreal winter, besides the standard variables. However, using novel approaches how to parametrize oGWs may bring the GWD closer to the observations (Xu et al., 2017, 2018). We examined possible links to SSWs with the climatologically averaged states during the oGW breaking above three selected hotspots: Himalayas, East Asia and West America. Highlighting an importance of GW perturbation outside of the surf zone as in compensation-mechanism studies (e.g. Cohen et al., 2014), we found out that the Himalayas hotspot reveals common features of this

mechanism and may be associated with SSWs. However, for a causality confirmation which hotspot characteristic, i.e. meridional, zonal or even vertical position, temporal variability regarding atmospheric modes (QBO, ENSO), possibly synchronization with other hotspots, is most contributing, it is necessary of usage of a model with similar complexity (White et al., 2018) or mechanistic GCM (Šácha et al., 2016).

The aim of this thesis is to fill in the pieces of puzzle regarding the top-down and bottom-up coupling mechanisms of various timescales in the middle atmosphere. Longer and shorter timescales are represented here by 11-year solar cycle and orographic GWs considered on the intraseasonal timescale, respectively. Nonetheless, there is a belief about the single unifying mechanism acting across different timescales (Kidston et al., 2015) similarly to the *theory of everything* explaining all physical aspects of the universe (Ellis, 1986). As stated above many questions remain for the middle atmosphere research to answer, but they are out of the scope of this thesis.

Bibliography

Abalos, M., Legras, B., Ploeger, F., and Randel, W. J.: Evaluating the advective Brewer-Dobson circulation in three reanalyses for the period 1979-2012, Journal of Geophysical Research: Atmospheres, 120, 7534–7554, doi:10.1002/2015JD023182, URL http://doi.wiley.com/10.1002/2015JD023182, 2015.

Albers, J. R. and Birner, T.: Vortex Preconditioning due to Planetary and Gravity Waves prior to Sudden Stratospheric Warmings, Journal of the Atmospheric Sciences, 71, 4028–4054, doi:10.1175/JAS-D-14-0026.1, URL http://journals.ametsoc.org/doi/abs/10.1175/JAS-D-14-0026.1, 2014.

Alexander, M. J.: Gravity waves in the stratosphere, in: The Stratosphere: Dynamics, Transport, and Chemistry, pp. 109–121, American Geophysical Union, doi:10.1029/2009GM000864, URL http://doi.wiley.com/10.1029/2009GM000864, 2010.

Alexander, M. J. and Teitelbaum, H.: Three-dimensional properties of Andes mountain waves observed by satellite: A case study, Journal of Geophysical Research: Atmospheres, 116, 2011.

Alexander, S., Klekociuk, A., Pitts, M., McDonald, A., and Arevalo-Torres, A.: The effect of orographic gravity waves on Antarctic polar stratospheric cloud occurrence and composition, Journal of Geophysical Research: Atmospheres, 116, 2011.

Andrews, D. and McIntyre, M.: Generalized Eliassen-Palm and Charney-Drazin theorems for waves on axismmetric mean flows in compressible atmospheres, Journal of the Atmospheric Sciences, 35, 175–185, 1978.

Andrews, D. and McIntyre, M. E.: Planetary waves in horizontal and vertical shear: The generalized Eliassen-Palm relation and the mean zonal acceleration, Journal of the Atmospheric Sciences, 33, 2031–2048, 1976.

Andrews, D. G. and McIntyre, M. E.: JR Holton, and CB Leovy, 1987: Middle Atmosphere Dynamics, 1987.

Arfeuille, F., Luo, B. P., Heckendorn, P., Weisenstein, D., Sheng, J. X., Rozanov, E., Schraner, M., Brönnimann, S., Thomason, L. W., and Peter, T.: Modeling the stratospheric warming following the Mt. Pinatubo eruption: uncertainties in aerosol extinctions, Atmospheric Chemistry and Physics, 13, 11 221–11 234, doi:10.5194/acp-13-11221-2013, URL http://www.atmos-chem-phys.net/13/11221/2013/, 2013.

Austin, J., Tourpali, K., Rozanov, E., Akiyoshi, H., Bekki, S., Bodeker, G., Brühl, C., Butchart, N., Chipperfield, M., Deushi, M., Fomichev, V. I., Giorgetta, M. A., Gray, L., Kodera, K., Lott, F., Manzini, E., Marsh, D., Matthes, K., Nagashima, T., Shibata, K., Stolarski, R. S., Struthers, H., and Tian, W.: Coupled chemistry climate model simulations of the solar cycle in ozone and temperature, Journal of Geophysical Research, 113, D11 306, doi:10.1029/2007JD009391, URL http://doi.wiley.com/10.1029/2007JD009391, 2008.

Baldwin, M. P. and Dunkerton, T. J.: Propagation of the Arctic Oscillation from the stratosphere to the troposphere, Journal of Geophysical Research: Atmospheres, 104, 30 937–30 946, 1999.

Ball, W. T., Krivova, N. A., Unruh, Y. C., Haigh, J. D., and Solanki, S. K.: A New SATIRE-S Spectral Solar Irradiance Reconstruction for Solar Cycles 21-23 and Its Implications for Stratospheric Ozone, Journal of the Atmospheric Sciences, 71, 4086–4101, doi:10.1175/JAS-D-13-0241.1, URL http://journals.ametsoc.org/doi/abs/10.1175/JAS-D-13-0241.1, 2014a.

Ball, W. T., Krivova, N. A., Unruh, Y. C., Haigh, J. D., and Solanki, S. K.: A new SATIRE-S spectral solar irradiance reconstruction for solar cycles 21–23 and its implications for stratospheric ozone, arXiv preprint arXiv:1408.0365, 2014b.

Ball, W. T., Kuchař, A., Rozanov, E. V., Staehelin, J., Tummon, F., Smith, A. K., Sukhodolov, T., Stenke, A., Revell, L., Coulon, A., Schmutz, W., and Peter, T.: An Upper-branch Brewer Dobson Circulation index for attribution of stratospheric variability and improved ozone and temperature trend analysis, Atmospheric Chemistry and Physics, 2016, 1–20, doi:10.5194/acp-2016-449, URL http://www.atmos-chem-phys-discuss.net/acp-2016-449/, 2016.

Birner, T. and Albers, J. R.: Sudden Stratospheric Warmings and Anomalous Upward Wave Activity Flux, SOLA, 13A, 8–12, doi:10.2151/sola.13A-002, URL https://www.jstage.jst.go.jp/article/sola/13A/Special{_}Edition/13A{_}13A-002/{_}article, 2017.

Blume, C. and Matthes, K.: Understanding and forecasting polar stratospheric variability with statistical models, Atmos. Chem. Phys, 12, 5691–5701, 2012.

Boos, W. R. and Shaw, T. A.: The effect of moist convection on the tropospheric response to tropical and subtropical zonally asymmetric torques, Journal of the Atmospheric Sciences, 70, 4089–4111, 2013.

Box, G.: Box and Jenkins: time series analysis, forecasting and control, A Very British Affair: Six Britons and the Development of Time Series Analysis During the 20th Century, 161, 2012.

Boyd, J. P.: The noninteraction of waves with the zonally averaged flow on a spherical earth and the interrelationships on eddy fluxes of energy, heat and momentum, Journal of the Atmospheric Sciences, 33, 2285–2291, 1976.

Bramberger, M., Dörnbrack, A., Bossert, K., Ehard, B., Fritts, D. C., Kaifler, B., Mallaun, C., Orr, A., Pautet, P.-D., Rapp, M., Taylor, M. J., Vosper, S., Williams, B. P., and Witschas, B.: Does Strong Tropospheric Forcing Cause Large-Amplitude Mesospheric Gravity Waves? A DEEPWAVE Case Study, Journal of Geophysical Research: Atmospheres, 122, 11,422–11,443, doi:10.1002/2017JD027371, URL http://doi.wiley.com/10.1002/2017JD027371, 2017.

Brasseur, G. P. and Solomon, S.: Aeronomy of the middle atmosphere: chemistry and physics of the stratosphere and mesosphere, vol. 32, Springer Science & Business Media, 2006.

Bretherton, C. S., Widmann, M., Dymnikov, V. P., Wallace, J. M., and Bladé, I.: The effective number of spatial degrees of freedom of a time-varying field, Journal of climate, 12, 1990–2009, 1999.

Butchart, N.: The Brewer-Dobson circulation, Reviews of Geophysics, 52, 157–184, doi:10.1002/2013RG000448, URL http://doi.wiley.com/10.1002/2013RG000448, 2014.

Butler, A. H., Sjoberg, J. P., Seidel, D. J., and Rosenlof, K. H.: A Sudden Stratospheric Warming Compendium, Earth System Science Data Discussions, pp. 1–27, doi:10.5194/essd-2016-49, URL http://www.earth-syst-sci-data-discuss.net/essd-2016-49/, 2016.

Callaghan, P. F. and Salby, M. L.: Three-Dimensionality and Forcing of the Brewer-Dobson Circulation, Journal of the Atmospheric Sciences, 59, 976–991, doi:10.1175/1520-0469(2002)059⟨0976:TDAFOT⟩2.0.CO;2, URL http://journals.ametsoc.org/doi/abs/10.1175/1520-0469{%}282002{%}29059{%}3C0976{%}3ATDAFOT{%}3E2.0.CO{%}3B2, 2002.

Camp, C. D. and Tung, K.: The influence of the solar cycle and QBO on the late-winter stratospheric polar vortex, Journal of the atmospheric sciences, 64, 1267–1283, 2007.

CCMVal, S.: SPARC Report on the Evaluation of Chemistry-Climate Models, edited by: Eyring, V., Shepherd, TG, and Waugh, DW, Tech. rep., SPARC Report, 2010.

Charlton, A. J. and Polvani, L. M.: A New Look at Stratospheric Sudden Warmings. Part I: Climatology and Modeling Benchmarks, Journal of Climate, 20, 449–469, doi:10.1175/JCLI3996.1, URL http://journals.ametsoc.org/doi/abs/10.1175/JCLI3996.1, 2007.

Charney, J. G. and Drazin, P. G.: Propagation of planetary-scale disturbances from the lower into the upper atmosphere, Journal of Geophysical Research, 66, 83–109, doi:10.1029/JZ066i001p00083, URL http://doi.wiley.com/10.1029/JZ066i001p00083, 1961.

Chen, Y., Han, Y., Liu, Q., Van Delst, P., and Weng, F.: Community radiative transfer model for Stratospheric Sounding Unit, Journal of Atmospheric and Oceanic Technology, 28, 767–778, 2011.

Chiodo, G., Calvo, N., Marsh, D., and Garcia-Herrera, R.: The 11 year solar cycle signal in transient simulations from the Whole Atmosphere Community Climate Model, Journal of Geophysical Research: Atmospheres, 117, 2012.

Chiodo, G., Marsh, D., Garcia-Herrera, R., Calvo, N., and García, J.: On the detection of the solar signal in the tropical stratosphere, Atmospheric Chemistry and Physics, 14, 5251–5269, 2014.

Cnossen, I., Lu, H., Bell, C. J., Gray, L. J., and Joshi, M. M.: Solar signal propagation: The role of gravity waves and stratospheric sudden warmings, Journal of Geophysical Research, 116, D02 118, doi:10.1029/2010JD014535, URL http://doi.wiley.com/10.1029/2010JD014535, 2011.

Cohen, J. and Jones, J.: Tropospheric precursors and stratospheric warmings, Journal of climate, 24, 6562–6572, 2011.

Cohen, N. Y. and Boos, W. R.: The influence of orographic Rossby and gravity waves on rainfall, Quarterly Journal of the Royal Meteorological Society, 143, 845–851, doi:10.1002/qj.2969, 2017.

Cohen, N. Y., Gerber, E. P., and Bühler, O.: What Drives the Brewer-Dobson Circulation?, Journal of the Atmospheric Sciences, 71, 3837–3855, doi:10.1175/JAS-D-14-0021.1, URL http://journals.ametsoc.org/doi/abs/10.1175/JAS-D-14-0021.1, 2014.

Compo, G. P., Whitaker, J. S., Sardeshmukh, P. D., Matsui, N., Allan, R. J., Yin, X., Gleason, B. E., Vose, R. S., Rutledge, G., Bessemoulin, P., Brönnimann, S., Brunet, M., Crouthamel, R. I., Grant, A. N., Groisman, P. Y., Jones, P. D., Kruk, M. C., Kruger, A. C., Marshall, G. J., Maugeri, M., Mok, H. Y., Nordli, ., Ross, T. F., Trigo, R. M., Wang, X. L., Woodruff, S. D., and Worley, S. J.: The Twentieth Century Reanalysis Project, Quarterly Journal of the Royal Meteorological Society, 137, 1–28, doi:10.1002/qj.776, URL http://dx.doi.org/10.1002/qj.776, 2011.

Cortes, C. and Vapnik, V.: Support-vector networks, Machine Learning, 20, 273–297, doi:10.1007/BF00994018, URL http://link.springer.com/10.1007/BF00994018, 1995.

Coughlin, K. and Tung, K.-K.: Eleven-year solar cycle signal throughout the lower atmosphere, Journal of Geophysical Research: Atmospheres, 109, 2156–2202, doi:10.1029/2004JD004873, 2004.

Crooks, S. A. and Gray, L. J.: Characterization of the 11-year solar signal using a multiple regression analysis of the ERA-40 dataset, Journal of climate, 18, 996–1015, 2005.

Cullens, C. Y., England, S. L., and Garcia, R. R.: The 11 year solar cycle signature on wave-driven dynamics in WACCM, Journal of Geophysical Research: Space Physics, 121, 3484–3496, doi:10.1002/2016JA022455, URL http://doi.wiley.com/10.1002/2016JA022455, 2016.

Dee, D. P., Uppala, S. M., Simmons, A. J., Berrisford, P., Poli, P., Kobayashi, S., Andrae, U., Balmaseda, M., Balsamo, G., Bauer, P., Bechtold, P., Beljaars, A. C. M., van de Berg, L., Bidlot, J., Bormann, N., Delsol, C., Dragani, R., Fuentes, M., Geer, A. J., Haimberger, L., Healy, S. B., Hersbach, H., Hólm, E. V., Isaksen, L., Kållberg, P., Köhler, M., Matricardi, M., McNally, A. P., Monge-Sanz, B. M., Morcrette, J.-J., Park, B.-K., Peubey, C., de Rosnay, P., Tavolato, C., Thépaut, J.-N., and Vitart, F.: The ERA-Interim reanalysis: Configuration and performance of the data assimilation system, Quarterly Journal of the Royal Meteorological Society, 137, 553–597, 2011a.

Dee, D. P., Uppala, S. M., Simmons, A. J., Berrisford, P., Poli, P., Kobayashi, S., Andrae, U., Balmaseda, M. A., Balsamo, G., Bauer, P., Bechtold, P., Beljaars, A. C. M., van de Berg, L., Bidlot, J., Bormann, N., Delsol, C., Dragani, R., Fuentes, M., Geer, A. J., Haimberger, L., Healy, S. B., Hersbach, H., Hólm, E. V., Isaksen, L., Kållberg, P., Köhler, M., Matricardi, M., McNally, A. P., Monge-Sanz, B. M., Morcrette, J.-J., Park, B.-K., Peubey, C., de Rosnay, P., Tavolato, C., Thépaut, J.-N., and Vitart, F.: The ERA-Interim reanalysis: configuration and performance of the data assimilation system, Quarterly Journal of the Royal Meteorological Society, 137, 553–597, doi:10.1002/qj.828, URL http://doi.wiley.com/10.1002/qj.828, 2011b.

Demirhan Bari, D., Gabriel, A., Körnich, H., and Peters, D. W. H.: The effect of zonal asymmetries in the Brewer-Dobson circulation on ozone and water vapor distributions in the northern middle atmosphere, Journal of Geophysical Research: Atmospheres, 118, 3447–3466, doi:10.1029/2012JD017709, URL http://doi.wiley.com/10.1029/2012JD017709, 2013.

Dhomse, S., Chipperfield, M. P., Feng, W., and Haigh, J. D.: Solar response in tropical stratospheric ozone: a 3-D chemical transport model study using ERA reanalyses, Atmospheric Chemistry and Physics, 11, 12 773–12 786, doi:10.5194/acp-11-12773-2011, URL http://www.atmos-chem-phys.net/11/12773/2011/, 2011.

Durbin, J. and Watson, G. S.: Testing for serial correlation in least squares regression: I, Biometrika, pp. 409–428, 1950.

Ebita, A., Kobayashi, S., Ota, Y., Moriya, M., Kumabe, R., Onogi, K., Harada, Y., Yasui, S., Miyaoka, K., Takahashi, K., Kamahori, H., Kobayashi, C., Endo, H., Soma, M., Oikawa, Y., and Ishimizu, T.: The Japanese 55-year Reanalysis (JRA-55): an interim report, Sola, 7, 149–152, 2011.

Eckermann, S. D. and Preusse, P.: Global measurements of stratospheric mountain waves from space, Science, 286, 1534–1537, 1999.

Edmon Jr, H., Hoskins, B., and McIntyre, M.: Eliassen-Palm cross sections for the troposphere, Journal of the Atmospheric Sciences, 37, 2600–2616, 1980.

Egorova, T., Rozanov, E., Zubov, V., and Karol, I.: Model for investigating ozone trends (MEZON), Izvestiya Atmospheric and Oceanic Physics, 39, 277–292, 2003.

Egorova, T., Rozanov, E., Manzini, E., Haberreiter, M., Schmutz, W., Zubov, V., and Peter, T.: Chemical and dynamical response to the 11-year variability of the solar irradiance simulated with a chemistry-climate model, Geophysical Research Letters, 31, n/a–n/a, doi:10.1029/2003GL019294, URL http://dx.doi.org/10.1029/2003GL019294, l06119, 2004.

Ehard, B., Kaifler, B., Dörnbrack, A., Preusse, P., Eckermann, S. D., Bramberger, M., Gisinger, S., Kaifler, N., Liley, B., Wagner, J., and Rapp, M.: Horizontal propagation of large-amplitude mountain waves into the polar night jet, Journal of Geophysical Research, 122, 1423–1436, doi:10.1002/2016JD025621, 2017.

Eliassen, A.: On the transfer of energy in stationary mountain waves, Geophy. Publ., 22, 1–23, 1960.

Ellis, J.: The superstring: theory of everything, or of nothing?, Nature, 323, 595, 1986.

Ermolli, I., Matthes, K., Dudok de Wit, T., Krivova, N. A., Tourpali, K., Weber, M., Unruh, Y. C., Gray, L., Langematz, U., Pilewskie, P., Rozanov, E., Schmutz, W., Shapiro, A., Solanki, S. K., and Woods, T. N.: Recent variability of the solar spectral irradiance and its impact on climate modelling, Atmospheric Chemistry and Physics, 13, 3945–3977, doi:10.5194/acp-13-3945-2013, URL http://www.atmos-chem-phys.net/13/3945/2013/, 2013.

Ern, M., Trinh, Q. T., Kaufmann, M., Krisch, I., Preusse, P., Ungermann, J., Zhu, Y., Gille, J. C., Mlynczak, M. G., Russell III, J. M., Schwartz, M. J., and Riese, M.: Satellite observations of middle atmosphere gravity wave absolute momentum flux and of its vertical gradient during recent stratospheric warmings, Atmospheric Chemistry and Physics, 16, 9983–10 019, doi:10.5194/acp-16-9983-2016, URL http://www.atmos-chem-phys.net/16/9983/2016/, 2016.

Ern, M., Trinh, Q. T., Preusse, P., Gille, J. C., Mlynczak, M. G., Russell III, J. M., and Riese, M.: GRACILE: a comprehensive climatology of atmospheric gravity wave parameters based on satellite limb soundings, Earth System Science Data, 10, 857–892, doi:10.5194/essd-10-857-2018, URL https://www.earth-syst-sci-data.net/10/857/2018/, 2018.

Esler, J. G. and Matthewman, N. J.: Stratospheric Sudden Warmings as Self-Tuning Resonances. Part II: Vortex Displacement Events, Journal of the Atmospheric Sciences, 68, 2505–2523, doi:10.1175/JAS-D-11-08.1, URL http://journals.ametsoc.org/doi/abs/10.1175/JAS-D-11-08.1, 2011.

Eyring, V., Lamarque, J.-F., Cionni, I., Duncan, B., Fiore, A., Gettelman, A., Hegglin, M., Hess, P., Nagashima, T., Ryerson, T., et al.: Report on the IGAC/SPARC Chemistry-Climate Model Initiative (CCMI) 2013 Science Workshop, Report on the 34th Session of the Joint Scientific Committee of the World Climate Research Programme, p. 23, URL http://www.met.reading.ac.uk/~qr903932/CCMI-website/Wordpress_PDFs/CCMI2013_WorkshopSummary_SPARCnewsletterJuly2013_onlinefirst.pdf, 2014.

Fomichev, V. I., Ward, W. E., Beagley, S. R., McLandress, C., McConnell, J. C., McFarlane, N. A., and Shepherd, T. G.: Extended Canadian Middle Atmosphere Model: Zonal-mean climatology and physical parameterizations, Journal of Geophysical Research: Atmospheres, 107, ACL 9–1–ACL 9–14, doi:10.1029/2001JD000479, URL http://doi.wiley.com/10.1029/2001JD000479, 2002.

Frame, T. H. A. and Gray, L. J.: The 11-Yr Solar Cycle in ERA-40 Data: An Update to 2008, Journal of Climate, 23, 2213–2222, doi:10.1175/2009JCLI3150.1, 2010.

Fritts, D. C. and Alexander, M. J.: Gravity wave dynamics and effects in the middle atmosphere, Reviews of geophysics, 41, 2003.

Fujiwara, M., Polavarapu, S., and Jackson, D.: A proposal of the SPARC reanalysis/analysis intercomparison project, SPARC Newsletter, 38, 14–17, 2012.

Fujiwara, M., Hibino, T., Mehta, S. K., Gray, L., Mitchell, D., and Anstey, J.: Global temperature response to the major volcanic eruptions in multiple reanalysis datasets, Atmospheric Chemistry and Physics Discussions, 15, 13 315–13 346, doi:10.5194/acpd-15-13315-2015, URL http://www.atmos-chem-phys-discuss.net/15/13315/2015/, 2015.

Garcia, R. R., Smith, A. K., Kinnison, D. E., de la Cámara, Á., and Murphy, D. J.: Modification of the Gravity Wave Parameterization in the Whole Atmosphere Community Climate Model: Motivation and Results, Journal of the Atmospheric Sciences, 74, 275–291, doi:10.1175/JAS-D-16-0104.1, URL http://journals.ametsoc.org/doi/10.1175/JAS-D-16-0104.1, 2017.

Garfinkel, C. I., Silverman, V., Harnik, N., Haspel, C., and Riz, Y.: Stratospheric response to intraseasonal changes in incoming solar radiation, Journal of Geophysical Research: Atmospheres, pp. n/a–n/a, doi:10.1002/2015JD023244, URL http://doi.wiley.com/10.1002/2015JD023244, 2015.

Geller, M. A., Alexander, M. J., Love, P. T., Bacmeister, J., Ern, M., Hertzog, A., Manzini, E., Preusse, P., Sato, K., Scaife, A. A., and Zhou, T.: A Comparison between Gravity Wave Momentum Fluxes in Observations and Climate Models, Journal of Climate, 26, 6383–6405, doi:10.1175/JCLI-D-12-00545.1, URL http://journals.ametsoc.org/doi/abs/10.1175/JCLI-D-12-00545.1, 2013.

Gerber, E. P., Butler, A., Calvo, N., Charlton-Perez, A., Giorgetta, M., Manzini, E., Perlwitz, J., Polvani, L. M., Sassi, F., Scaife, A. A., Shaw, T. A., Son, S.-W., and Watanabe, S.: Assessing and Understanding the Impact of Stratospheric Dynamics and Variability on the Earth System., Bulletin of the American Meteorological Society, 93, 845–859, doi:10.1175/BAMS-D-11-00145.1, 2012.

Gevrey, M., Dimopoulos, I., and Lek, S.: Review and comparison of methods to study the contribution of variables in artificial neural network models, Ecological Modelling, 160, 249–264, 2003.

Gewin, V.: Data sharing: An open mind on open data, Nature, 529, 117–119, 2016.

Giorgetta, M. A., Manzini, E., Roeckner, E., Esch, M., and Bengtsson, L.: Climatology and Forcing of the Quasi-Biennial Oscillation in the MAECHAM5 Model, Journal of Climate, 19, 3882–3901, doi:10.1175/JCLI3830.1, URL http://journals.ametsoc.org/doi/abs/10.1175/JCLI3830.1, 2006.

Graf, H.-F., Li, Q., and Giorgetta, M.: Volcanic effects on climate: revisiting the mechanisms, Atmospheric Chemistry and Physics, 7, 4503–4511, 2007.

Gray, L. J., Crooks, S., Pascoe, C., Sparrow, S., and Palmer, M.: Solar and QBO influences on the timing of stratospheric sudden warmings, Journal of the atmospheric sciences, 61, 2777–2796, 2004.

Gray, L. J., Rumbold, S., and Shine, K. P.: Stratospheric temperature and radiative forcing response to 11-year solar cycle changes in irradiance and ozone, Journal of the Atmospheric Sciences, 66, 2402–2417, 2009.

Gray, L. J., Beer, J., Geller, M., Haigh, J. D., Lockwood, M., Matthes, K., Cubasch, U., Fleitmann, D., Harrison, G., Hood, L., Luterbacher, J., Meehl, G. A., Shindell, D., van Geel, B., and White, W.: Solar influences on climate, Reviews of Geophysics, 48, RG4001, doi:10.1029/2009RG000282, 2010.

Gray, L. J., Scaife, A. A., Mitchell, D. M., Osprey, S., Ineson, S., Hardiman, S., Butchart, N., Knight, J., Sutton, R., and Kodera, K.: A lagged response to the 11 year solar cycle in observed winter Atlantic/European weather patterns, Journal of Geophysical Research: Atmospheres, 118, 13,405–13,420, doi:10.1002/2013JD020062, URL http://dx.doi.org/10.1002/2013JD020062, 2013.

Haigh, J. D.: The role of stratospheric ozone in modulating the solar radiative forcing of climate, Nature, 370, 544–546, 1994.

Harder, J. W., Fontenla, J. M., Pilewskie, P., Richard, E. C., and Woods, T. N.: Trends in solar spectral irradiance variability in the visible and infrared, Geophysical Research Letters, 36, 1944–8007, doi:10.1029/2008GL036797, 2009.

Haykin, S. S.: Neural networks and learning machines, vol. 3, Pearson Education Upper Saddle River, 2009.

Haynes, P.: Stratospheric Dynamics, Annual Review of Fluid Mechanics, 37, 263–293, doi:10.1146/annurev.fluid.37.061903.175710, URL http://www.annualreviews.org/doi/abs/10.1146/annurev.fluid.37.061903.175710, 2005.

Haynes, P. and Shepherd, T.: The importance of surface pressure changes in the response of the atmosphere to zonally-symmetric thermal and mechanical forcing, Quarterly Journal of the Royal Meteorological Society, 115, 1181–1208, 1989.

Haynes, P. H., McIntyre, M. E., Shepherd, T. G., Marks, C. J., and Shine, K. P.: On the "Downward Control" of Extratropical Diabatic Circulations by Eddy-Induced Mean Zonal Forces, Journal of the Atmospheric Sciences, 48, 651–678, doi:10.1175/1520-0469(1991)048⟨0651:OTCOED⟩2.0.CO;2, URL http://journals.ametsoc.org/doi/abs/10.1175/1520-0469{%}281991{%}29048{%}3C0651{%}3AOTCOED{%}3E2.0.CO{%}3B2, 1991.

Hines, C. O.: Doppler-spread parameterization of gravity-wave momentum deposition in the middle atmosphere. Part 1: Basic formulation, Journal of Atmospheric and Solar-Terrestrial Physics, 59, 371–386, 1997a.

Hines, C. O.: Doppler-spread parameterization of gravity-wave momentum deposition in the middle atmosphere. Part 2: Broad and quasi monochromatic spectra, and implementation, Journal of Atmospheric and Solar-Terrestrial Physics, 59, 387–400, 1997b.

Hirano, S., Kohma, M., and Sato, K.: A three-dimensional analysis on the role of atmospheric waves in the climatology and interannual variability of stratospheric final warming in the Southern Hemisphere, Journal of Geophysical Research: Atmospheres, 121, 8429–8443, doi:10.1002/2015JD024481, URL http://doi.wiley.com/10.1002/2015JD024481, 2016.

Hitchcock, P. and Haynes, P. H.: Stratospheric control of planetary waves, Geophysical Research Letters, 43, 11,884–11,892, doi:10.1002/2016GL071372, URL http://doi.wiley.com/10.1002/2016GL071372, 2016.

Hoffmann, L., Xue, X., and Alexander, M. J.: A global view of stratospheric gravity wave hotspots located with Atmospheric Infrared Sounder observations, Journal of Geophysical Research: Atmospheres, 118, 416–434, doi:10.1029/2012JD018658, URL http://doi.wiley.com/10.1029/2012JD018658, 2013.

Holt, L., Alexander, M., Coy, L., Liu, C., Molod, A., Putman, W., and Pawson, S.: An evaluation of gravity waves and gravity wave sources in the Southern Hemisphere in a 7-km global climate simulation, Quarterly Journal of the Royal Meteorological Society, 2017.

Holton, J. R.: The role of gravity wave induced drag and diffusion in the momentum budget of the mesosphere, Journal of the Atmospheric Sciences, 39, 791–799, 1982.

Holton, J. R.: The influence of gravity wave breaking on the general circulation of the middle atmosphere, Journal of the Atmospheric Sciences, 40, 2497–2507, 1983.

Holton, J. R. and Tan, H.-C.: The influence of the equatorial quasi-biennial oscillation on the global circulation at 50 mb, Journal of the Atmospheric Sciences, 37, 2200–2208, 1980.

Hood, L.: Lagged response of tropical tropospheric temperature to solar ultraviolet variations on intraseasonal time scales, Geophysical Research Letters, 43, 4066–4075, 2016.

Hood, L., Schimanke, S., Spangehl, T., Bal, S., and Cubasch, U.: The Surface Climate Response to 11-Yr Solar Forcing during Northern Winter: Observational Analyses and Comparisons with GCM Simulations, Journal of Climate, 26, 7489–7506, doi:10.1175/JCLI-D-12-00843.1, URL http://dx.doi.org/10.1175/JCLI-D-12-00843.1, 2013.

Hood, L. L. and Soukharev, B. E.: The Lower-Stratospheric Response to 11-Yr Solar Forcing: Coupling to the Troposphere-Ocean Response, Journal of the Atmospheric Sciences, 69, 1841–1864, doi:10.1175/JAS-D-11-086.1, URL http://dx.doi.org/10.1175/JAS-D-11-086.1, 2012.

Hood, L. L., Soukharev, B. E., and McCormack, J. P.: Decadal variability of the tropical stratosphere: Secondary influence of the El Niño–Southern Oscillation, Journal of Geophysical Research, 115, D11 113, 2010.

Hood, L. L., Misios, S., Mitchell, D. M., Rozanov, E., Gray, L. J., Tourpali, K., Matthes, K., Schmidt, H., Chiodo, G., Thiéblemont, R., Shindell, D., and Krivolutsky, A.: Solar Signals in CMIP-5 Simulations: The Ozone Response, Quarterly Journal of the Royal Meteorological Society, pp. n/a–n/a, doi:10.1002/qj.2553, URL http://dx.doi.org/10.1002/qj.2553, 2015.

Hoyer, S., Fitzgerald, C., Hamman, J., akleeman, Kluyver, T., Roos, M., Helmus, J. J., Markel, Cable, P., Maussion, F., Miles, A., Kanmae, T., Wolfram, P., Sinclair, S., Bovy, B., ebrevdo, Guedes, R., Abernathey, R., Filipe, Hill, S., Richards, N., Lee, A., Koldunov, N., Graham, M., maciekswat, Gerard, J., Babuschkin, I., Deil, C., Welch, E., and Hilboll, A.: xarray: v0.8.0, doi:10.5281/zenodo.59499, URL http://dx.doi.org/10.5281/zenodo.59499, 2016.

Huang, C. S. Y. and Nakamura, N.: Local Finite-Amplitude Wave Activity as a Diagnostic of Anomalous Weather Events, Journal of the Atmospheric Sciences, 73, 211–229, doi:10.1175/JAS-D-15-0194.1, URL http://journals.ametsoc.org/doi/10.1175/JAS-D-15-0194.1https://github.com/csyhuang/hn2016{_}falwa, 2016.

Ineson, S., Scaife, A. A., Knight, J. R., Manners, J. C., Dunstone, N. J., Gray, L. J., and Haigh, J. D.: Solar forcing of winter climate variability in the Northern Hemisphere, Nature Geoscience, 4, 753–757, 2011.

Kaifler, B., Kaifler, N., Ehard, B., Dörnbrack, A., Rapp, M., and Fritts, D. C.: Influences of source conditions on mountain wave penetration into the stratosphere and mesosphere, Geophysical Research Letters, 42, 9488–9494, doi:10.1002/2015GL066465, URL http://doi.wiley.com/10.1002/2015GL066465, 2015.

Kalisch, S., Chun, H. Y., Ern, M., Preusse, P., Trinh, Q. T., Eckermann, S. D., and Riese, M.: Comparison of simulated and observed convective gravity waves, Journal of Geophysical Research: Atmospheres, 121, 13,474–13,492, doi:10.1002/2016JD025235, URL https://agupubs.onlinelibrary.wiley.com/doi/abs/10.1002/2016JD025235, 2016.

Kalnay, E., Kanamitsu, M., Kistler, R., Collins, W., Deaven, D., Gandin, L., Iredell, M., Saha, S., White, G., Woollen, J., Zhu, Y., Leetmaa, A., Reynolds, R., Chelliah, M., Ebisuzaki, W., Higgins, W., Janowiak, J., Mo, K. C., Ropelewski, C., Wang, J., Jenne, R., and Joseph, D.: The NCEP/NCAR 40-year reanalysis project, Bulletin of the American Meteorological Society, 77, 437–471, doi:10.1175/1520-0477(1996)077⟨0437:TNYRP⟩2.0.CO;2, URL http://www.mendeley.com/research/declining-mountain-snowpack-in-western-north-america/, 1996.

Ke, W. and Wen, C.: Northern Hemisphere Stratospheric Polar Vortex Extremes in February under the Control of Downward Wave Flux in the Lower Stratosphere, Atmospheric and Oceanic Science Letters, 5, 183–188, 2012.

Kidston, J., Scaife, A. A., Hardiman, S. C., Mitchell, D. M., Butchart, N., Baldwin, M. P., and Gray, L. J.: Stratospheric influence on tropospheric jet streams, storm tracks and surface weather, Nature Geoscience, doi:10.1038/ngeo2424, URL http://www.nature.com/doifinder/10.1038/ngeo2424, 2015.

Kinoshita, T. and Sato, K.: A formulation of unified three-dimensional wave activity flux of inertia–gravity waves and Rossby waves, Journal of the Atmospheric Sciences, 70, 1603–1615, 2013.

Kinoshita, T., Tomikawa, Y., and Sato, K.: On the three-dimensional residual mean circulation and wave activity flux of the primitive equations, Journal of the Meteorological Society of Japan. Ser. II, 88, 373–394, 2010.

Kinoshita, T., Iwasaki, T., and Sato, K.: A formulation of three dimensional wave activity flux describing wave propagation on the mass-weighted isentropic time mean equation, SOLA, 12, 198–202, 2016.

Kodera, K.: A possible mechanism of solar modulation of the spatial structure of the North Atlantic Oscillation, Journal of Geophysical Research, 110, D02 111, doi:10.1029/2004JD005258, URL http://doi.wiley.com/10.1029/2004JD005258, 2005.

Kodera, K. and Kuroda, Y.: Dynamical response to the solar cycle, Journal of Geophysical Research: Atmospheres, 107, ACL 5–1–ACL 5–12, doi:10.1029/2002JD002224, URL http://dx.doi.org/10.1029/2002JD002224, 2002.

Kohavi, R.: A study of cross-validation and bootstrap for accuracy estimation and model selection, in: IJCAI, vol. 14, pp. 1137–1145, 1995.

Koster, R. D., Bosilovich, M. G., Akella, S., Lawrence, C., Cullather, R., Draper, C., Gelaro, R., Kovach, R., Liu, Q., Molod, A., et al.: Technical Report Series on Global Modeling and Data Assimilation, Volume 43. MERRA-2; Initial Evaluation of the Climate, 2015.

Kren, A., Marsh, D., Smith, A., and Pilewskie, P.: Examining the stratospheric response to the solar cycle in a coupled WACCM simulation with an internally generated QBO, Atmospheric Chemistry and Physics, 14, 4843–4856, 2014.

Krivova, N. A., Vieira, L. E. A., and Solanki, S. K.: Reconstruction of solar spectral irradiance since the Maunder minimum, Journal of Geophysical Research: Space Physics, 115, n/a–n/a, doi:10.1029/2010JA015431, URL http://dx.doi.org/10.1029/2010JA015431, a12112, 2010.

Kruse, C. G., Smith, R. B., and Eckermann, S. D.: The Midlatitude Lower-Stratospheric Mountain Wave "Valve Layer", Journal of the Atmospheric Sciences, 73, 5081–5100, doi:10.1175/JAS-D-16-0173.1, URL https://doi.org/10.1175/JAS-D-16-0173.1, 2016.

Kuchar, A.: EPFD: Second release of EPFD python script, doi:10.5281/zenodo.16339, URL http://dx.doi.org/10.5281/zenodo.16339, 2015.

Kuchar, A.: kuchaale/X-regression: X-regression: First release kuchaale/X-regression: X-regression: First release, doi:10.5281/zenodo.159817, URL https://doi.org/10.5281/zenodo.159817, 2016.

Kuchar, A.: Accompanying data to "Role of parametrized orographic gravity waves in the lower stratosphere", Mendeley Data, doi:10.17632/gd3jsy3xmz.1, URL http://dx.doi.org/10.17632/gd3jsy3xmz.1, 2018.

Kuchar, A. and Revell, L.: Model simulations data to "On the aliasing of the solar cycle in the lower-stratospheric tropical temperature", Mendeley Data, doi:10.17632/khrhbw6wn5.1, URL http://dx.doi.org/10.17632/khrhbw6wn5.1, 2017.

Kuchar, A., Sacha, P., Miksovsky, J., and Pisoft, P.: The 11-year solar cycle in current reanalyses: a (non)linear attribution study of the middle atmosphere, Atmospheric Chemistry and Physics, 15, 6879–6895, doi:10.5194/acp-15-6879-2015, URL http://www.atmos-chem-phys.net/15/6879/2015/, 2015.

Kuchar, A., Ball, W. T., Rozanov, E. V., Stenke, A., Revell, L., Miksovsky, J., Pisoft, P., and Peter, T.: On the aliasing of the solar cycle in the lower stratospheric tropical temperature, Journal of Geophysical Research: Atmospheres, doi:10.1002/2017JD026948, URL http://doi.wiley.com/10.1002/2017JD026948, 2017.

Kuchar, A., Sacha, P., and Pisoft, P.: Role of parametrized orographic gravity waves in the lower stratosphere, in prep.

Kuilman, M., Karlsson, B., Benze, S., and Megner, L.: Exploring noctilucent cloud variability using the nudged and extended version of the Canadian Middle Atmosphere Model, Journal of Atmospheric and Solar-Terrestrial Physics, 164, 276–288, doi:10.1016/j.jastp.2017.08.019, URL https://doi.org/10.1016/j.jastp.2017.08.019http://linkinghub.elsevier.com/retrieve/pii/S1364682617301529, 2017.

Kuroda, Y. and Kodera, K.: Variability of the polar night jet in the Northern and Southern Hemispheres, Journal of Geophysical Research: Atmospheres, 106, 20 703–20 713, 2001.

Labitzke, K.: Sunspots, the QBO, and the stratospheric temperature in the north polar region, Geophysical Research Letters, 14, 535–537, doi:10.1029/GL014i005p00535, URL http://dx.doi.org/10.1029/GL014i005p00535, 1987.

Labitzke, K., Kunze, M., and Bronnimann, S.: Sunspots, the QBO and the stratosphere in the North Polar Region 20 years later, Meteorologische Zeitschrift, 15, 355–363, 2006.

Lean, J.: Short term, direct indices of solar variability, Solar Variability and Climate, 94, 39–51, 2001.

Lean, J., Rottman, G., Harder, J., and Kopp, G.: SORCE Contributions to New Understanding of Global Change and Solar Variability, pp. 27–53, doi:10.1007/0-387-37625-9_3, URL http://dx.doi.org/10.1007/0-387-37625-9_3, 2005.

Lee, H. and Smith, A. K.: Simulation of the combined effects of solar cycle, quasi-biennial oscillation, and volcanic forcing on stratospheric ozone changes in recent decades, Journal of Geophysical Research: Atmospheres, 108, n/a–n/a, doi:10.1029/2001JD001503, URL http://dx.doi.org/10.1029/2001JD001503, 2003.

Limpasuvan, V., Alexander, M. J., Orsolini, Y. J., Wu, D. L., Xue, M., Richter, J. H., and Yamashita, C.: Mesoscale simulations of gravity waves during the 2008-2009 major stratospheric sudden warming, Journal of Geophysical Research, 116, D17 104, doi:10.1029/2010JD015190, URL http://doi.wiley.com/10.1029/2010JD015190, 2011.

Limpasuvan, V., Richter, J. H., Orsolini, Y. J., Stordal, F., and Kvissel, O.-K.: The roles of planetary and gravity waves during a major stratospheric sudden warming as characterized in WACCM, Journal of Atmospheric and Solar-Terrestrial Physics, 78-79, 84–98, doi:10.1016/j.jastp.2011.03.004, URL http://linkinghub.elsevier.com/retrieve/pii/S1364682611000733, 2012.

Lindzen, R. S.: Turbulence and stress owing to gravity wave and tidal breakdown, Journal of Geophysical Research: Oceans, 86, 9707–9714, 1981.

Lu, H., Gray, L. J., Baldwin, M. P., and Jarvis, M. J.: Life cycle of the QBO-modulated 11-year solar cycle signals in the Northern Hemispheric winter, Quarterly Journal of the Royal Meteorological Society, 135, 1030–1043, doi:10.1002/qj.419, URL http://doi.wiley.com/10.1002/qj.419, 2009.

Lubis, S. W., Huang, C. S., Nakamura, N., Omrani, N.-E., and Jucker, M.: Role of Finite-Amplitude Rossby Waves and Nonconservative Processes in Downward Migration of Extratropical Flow Anomalies, Journal of the Atmospheric Sciences, 2018.

Luo, B. P.: CCMI Aerosol Data Set, ftp://iacftp.ethz.ch/pub_read/luo/ccmi/, last accessed 1 Nov 2015, 2013.

Luo, B. P.: CMIP6 Aerosol Data Set, ftp://iacftp.ethz.ch/pub_read/luo/CMIP6/, last accessed 1 Nov 2016, 2016.

Manzini, E., Giorgetta, M., Esch, M., Kornblueh, L., and Roeckner, E.: The influence of sea surface temperatures on the northern winter stratosphere: Ensemble simulations with the MAECHAM5 model, Journal of climate, 19, 3863–3881, 2006.

Marsh, D. R. and Garcia, R. R.: Attribution of decadal variability in lower-stratospheric tropical ozone, Geophysical Research Letters, 34, doi:10.1029/2007GL030935, 2007.

Marsh, D. R., Garcia, R. R., Kinnison, D. E., Boville, B. A., Sassi, F., Solomon, S. C., and Matthes, K.: Modeling the whole atmosphere response to solar cycle changes in radiative and geomagnetic forcing, Journal of Geophysical Research: Atmospheres, 112, n/a–n/a, doi:10.1029/2006JD008306, URL http://dx.doi.org/10.1029/2006JD008306, d23306, 2007.

Martineau, P. and Son, S.-W.: Onset of Circulation Anomalies during Stratospheric Vortex Weakening Events: The Role of Planetary-Scale Waves, Journal of Climate, 28, 7347–7370, doi:10.1175/JCLI-D-14-00478.1, URL http://journals.ametsoc.org/doi/10.1175/JCLI-D-14-00478.1, 2015.

Martineau, P., Son, S.-W., and Taguchi, M.: Dynamical Consistency of Reanalysis Datasets in the Extratropical Stratosphere, Journal of Climate, 29, 3057–3074, doi:10.1175/JCLI-D-15-0469.1, URL http://journals.ametsoc.org/doi/10.1175/JCLI-D-15-0469.1, 2016.

Martineau, P., Son, S.-W., Taguchi, M., and Butler, A. H.: A comparison of the momentum budget in reanalysis datasets during sudden stratospheric warming events, Atmospheric Chemistry and Physics, 18, 7169–7187, doi:10.5194/acp-18-7169-2018, URL https://www.atmos-chem-phys.net/18/7169/2018/, 2018.

Matsuno, T.: Vertical Propagation of Stationary Planetary Waves in the Winter Northern Hemisphere, Journal of the Atmospheric Sciences, 27, 871–883, doi:10.1175/1520-0469(1970)027⟨0871:VPOSPW⟩2.0.CO;2, URL http://journals.ametsoc.org/doi/abs/10.1175/1520-0469{%}281970{%}29027{%}3C0871{%}3AVPOSPW{%}3E2.0.CO{%}3B2, 1970.

Matthes, K., Langematz, U., Gray, L. L., Kodera, K., and Labitzke, K.: Improved 11-year solar signal in the Freie Universität Berlin climate middle atmosphere model (FUB-CMAM), Journal of Geophysical Research: Atmospheres, 109, doi:10.1029/2003JD004012, 2004.

Matthes, K., Kuroda, Y., Kodera, K., and Langematz, U.: Transfer of the solar signal from the stratosphere to the troposphere: Northern winter, Journal of geophysical research, 111, D06 108, 2006.

Matthes, K., Marsh, D. R., Garcia, R. R., Kinnison, D. E., Sassi, F., and Walters, S.: Role of the QBO in modulating the influence of the 11 year solar cycle on the atmosphere using constant forcings, Journal of Geophysical Research: Atmospheres, 115, doi:10.1029/2009JD013020, 2010.

Matthes, K., Kodera, K., Garcia, R. R., Kuroda, Y., Marsh, D. R., and Labitzke, K.: The importance of time-varying forcing for QBO modulation of the atmospheric 11 year solar cycle signal, Journal of Geophysical Research: Atmospheres, 118, 4435–4447, doi:10.1002/jgrd.50424, URL http://doi.wiley.com/10.1002/jgrd.50424, 2013.

Matthes, K., Funke, B., Anderson, M. E., Barnard, L., Beer, J., Charbonneau, P., Clilverd, M. A., Dudok de Wit, T., Haberreiter, M., Hendry, A., Jackman,

C. H., Kretschmar, M., Kruschke, T., Kunze, M., Langematz, U., Marsh, D. R., Maycock, A., Misios, S., Rodger, C. J., Scaife, A. A., Seppälä, A., Shangguan, M., Sinnhuber, M., Tourpali, K., Usoskin, I., van de Kamp, M., Verronen, P. T., and Versick, S.: Solar Forcing for CMIP6 (v3.1), Geoscientific Model Development Discussions, pp. 1–82, doi:10.5194/gmd-2016-91, URL http://www.geosci-model-dev-discuss.net/gmd-2016-91/, 2016.

Matthewman, N. J. and Esler, J. G.: Stratospheric Sudden Warmings as Self-Tuning Resonances. Part I: Vortex Splitting Events, Journal of the Atmospheric Sciences, 68, 2481–2504, doi:10.1175/JAS-D-11-07.1, URL http://journals.ametsoc.org/doi/abs/10.1175/JAS-D-11-07.1, 2011.

McFarlane, N. A.: The Effect of Orographically Excited Gravity Wave Drag on the General Circulation of the Lower Stratosphere and Troposphere, Journal of the Atmospheric Sciences, 44, 1775–1800, doi:10.1175/1520-0469(1987)044⟨1775:TEOOEG⟩2.0.CO;2, URL http://journals.ametsoc.org/doi/abs/10.1175/1520-0469{%}281987{%}29044{%}3C1775{%}3ATEOOEG{%}3E2.0.CO{%}3B2, 1987.

McLandress, C.: On the importance of gravity waves in the middle atmosphere and their parameterization in general circulation models, Journal of Atmospheric and Solar-Terrestrial Physics, 60, 1357–1383, 1998.

McLandress, C., Shepherd, T. G., Polavarapu, S., and Beagley, S. R.: Is Missing Orographic Gravity Wave Drag near 60°S the Cause of the Stratospheric Zonal Wind Biases in Chemistry-Climate Models?, Journal of the Atmospheric Sciences, 69, 802–818, doi:10.1175/JAS-D-11-0159.1, URL http://journals.ametsoc.org/doi/abs/10.1175/JAS-D-11-0159.1, 2012.

McLandress, C., Scinocca, J. F., Shepherd, T. G., Reader, M. C., and Manney, G. L.: Dynamical Control of the Mesosphere by Orographic and Nonorographic Gravity Wave Drag during the Extended Northern Winters of 2006 and 2009, Journal of the Atmospheric Sciences, 70, 2152–2169, doi:10.1175/JAS-D-12-0297.1, URL http://journals.ametsoc.org/doi/abs/10.1175/JAS-D-12-0297.1, 2013a.

McLandress, C., Scinocca, J. F., Shepherd, T. G., Reader, M. C., and Manney, G. L.: Dynamical Control of the Mesosphere by Orographic and Nonorographic Gravity Wave Drag during the Extended Northern Winters of 2006 and 2009, Journal of the Atmospheric Sciences, 70, 2152–2169, doi:10.1175/JAS-D-12-0297.1, URL http://journals.ametsoc.org/doi/abs/10.1175/JAS-D-12-0297.1, 2013b.

McLandress, C., Plummer, D. A., and Shepherd, T. G.: Technical Note: A simple procedure for removing temporal discontinuities in ERA-Interim upper stratospheric temperatures for use in nudged chemistry-climate model simulations, Atmospheric Chemistry and Physics, 14, 1547–1555, doi:10.5194/acp-14-1547-2014, URL http://www.atmos-chem-phys.net/14/1547/2014/, 2014.

Mears, C. A. and Wentz, F. J.: Construction of the Remote Sensing Systems V3. 2 atmospheric temperature records from the MSU and AMSU microwave sounders, Journal of Atmospheric and Oceanic Technology, 26, 1040–1056, 2009.

Meehl, G. A., Arblaster, J. M., Matthes, K., Sassi, F., and van Loon, H.: Amplifying the Pacific climate system response to a small 11-year solar cycle forcing, Science, 325, 1114–1118, 2009.

Mitchell, D., Montabone, L., Thomson, S., and Read, P.: Polar vortices on Earth and Mars: A comparative study of the climatology and variability from reanalyses, Quarterly Journal of the Royal Meteorological Society, 141, 550–562, doi:10.1002/qj.2376, 2015a.

Mitchell, D. M., Gray, L. J., Fujiwara, M., Hibino, T., Anstey, J. A., Ebisuzaki, W., Harada, Y., Long, C., Misios, S., Stott, P. A., and Tan, D.: Signatures of naturally induced variability in the atmosphere using multiple reanalysis datasets, Quarterly Journal of the Royal Meteorological Society, 141, 2011–2031, doi:10.1002/qj.2492, URL http://dx.doi.org/10.1002/qj.2492, 2015b.

Mitchell, D. M., Misios, S., Gray, L. J., Tourpali, K., Matthes, K., Hood, L., Schmidt, H., Chiodo, G., Thiéblemont, R., Rozanov, E., Shindell, D., and Krivolutsky, A.: Solar Signals in CMIP-5 Simulations: The Stratospheric Pathway, Quarterly Journal of the Royal Meteorological Society, pp. n/a–n/a, doi:10.1002/qj.2530, URL http://doi.wiley.com/10.1002/qj.2530, 2015c.

Mlynczak, M. G., Mertens, C. J., Garcia, R. R., and Portmann, R. W.: A detailed evaluation of the stratospheric heat budget: 2. Global radiation balance and diabatic circulations, Journal of Geophysical Research: Atmospheres, 104, 6039–6066, doi:10.1029/1998JD200099, URL http://doi.wiley.com/10.1029/1998JD200099, 1999.

Molod, A., Takacs, L., Suarez, M., Bacmeister, J., Song, I.-S., and Eichmann, A.: The GEOS-5 atmospheric general circulation model: Mean climate and development from MERRA to Fortuna, 2012.

Molod, A., Takacs, L., Suarez, M., and Bacmeister, J.: Development of the GEOS-5 atmospheric general circulation model: evolution from MERRA to MERRA2, Geoscientific Model Development, 8, 1339–1356, doi:10.5194/gmd-8-1339-2015, URL http://www.geosci-model-dev.net/8/1339/2015/ https://disc.sci.gsfc.nasa.gov/daac-bin/FTPSubset2.pl, 2015.

Morgenstern, O., Hegglin, M. I., Rozanov, E., O'Connor, F. M., Abraham, N. L., Akiyoshi, H., Archibald, A. T., Bekki, S., Butchart, N., Chipperfield, M. P., Deushi, M., Dhomse, S. S., Garcia, R. R., Hardiman, S. C., Horowitz, L. W., Jöckel, P., Josse, B., Kinnison, D., Lin, M., Mancini, E., Manyin, M. E., Marchand, M., Marécal, V., Michou, M., Oman, L. D., Pitari, G., Plummer, D. A., Revell, L. E., Saint-Martin, D., Schofield, R., Stenke, A., Stone, K., Sudo, K., Tanaka, T. Y., Tilmes, S., Yamashita, Y., Yoshida, K., and Zeng, G.: Review of the global models used within phase 1 of the Chemistry–Climate Model Initiative (CCMI), Geoscientific Model Development, 10, 639–671, doi:10.5194/gmd-10-639-2017, URL http://www.geosci-model-dev.net/10/639/2017/, 2017a.

Morgenstern, O., Hegglin, M. I., Rozanov, E., O'Connor, F. M., Abraham, N. L., Akiyoshi, H., Archibald, A. T., Bekki, S., Butchart, N., Chipperfield, M. P., Deushi, M., Dhomse, S. S., Garcia, R. R., Hardiman, S. C., Horowitz, L. W., Jöckel, P., Josse, B., Kinnison, D., Lin, M., Mancini, E., Manyin, M. E., Marchand, M., Marécal, V., Michou, M., Oman, L. D., Pitari, G., Plummer, D. A., Revell, L. E., Saint-Martin, D., Schofield, R., Stenke, A., Stone, K., Sudo, K., Tanaka, T. Y., Tilmes, S., Yamashita, Y., Yoshida, K., and Zeng, G.: Review of the global models used within phase 1 of the Chemistry–Climate Model Initiative (CCMI), Geoscientific Model Development, 10, 639–671, doi:10.5194/gmd-10-639-2017, URL https://www.geosci-model-dev.net/10/639/2017/, 2017b.

Muthers, S., Kuchar, A., Stenke, A., Schmitt, J., Anet, J. G., Raible, C. C., and Stocker, T. F.: Stratospheric age of air variations between 1600-2100, Geophysical Research Letters, doi:10.1002/2016GL068734, URL http://doi.wiley.com/10.1002/2016GL068734, 2016.

Nakamura, H., Miyasaka, T., Kosaka, Y., Takaya, K., and Honda, M.: Northern Hemisphere Extratropical Tropospheric Planetary Waves and their Low-Frequency Variability: Their Vertical Structure and Interaction with Transient Eddies and Surface Thermal Contrasts, Climate Dynamics: Why Does Climate Vary, pp. 149–179, doi:10.1029/2008GM000789, 2013.

Nakamura, N.: Two-dimensional mixing, edge formation, and permeability diagnosed in an area coordinate, Journal of the atmospheric sciences, 53, 1524–1537, 1996.

Nakamura, N. and Solomon, A.: Finite-Amplitude Wave Activity and Mean Flow Adjustments in the Atmospheric General Circulation. Part I: Quasigeostrophic Theory and Analysis, Journal of the Atmospheric Sciences, 67, 3967–3983, doi:10.1175/2010JAS3503.1, URL http://journals.ametsoc.org/doi/abs/10.1175/2010JAS3503.1, 2010.

Nakamura, N. and Zhu, D.: Finite-Amplitude Wave Activity and Diffusive Flux of Potential Vorticity in Eddy-Mean Flow Interaction, Journal of the Atmospheric Sciences, 67, 2701–2716, doi:10.1175/2010JAS3432.1, URL http://journals.ametsoc.org/doi/abs/10.1175/2010JAS3432.1, 2010a.

Nakamura, N. and Zhu, D.: Finite-amplitude wave activity and diffusive flux of potential vorticity in eddy–mean flow interaction, Journal of the Atmospheric Sciences, 67, 2701–2716, 2010b.

NCAR: The Climate Data Guide: Multivariate ENSO Index, Retrieved from https://climatedataguide.ucar.edu/climate-data/multivariate-enso-index, 2013.

Neter, J., Kutner, M., Wasserman, W., and Nachtsheim, C.: Applied Linear Statistical Models, McGraw-Hill/Irwin, 2004.

NOAA: Northern Atlantic Oscillation index, Retrieved from http://www.cpc.ncep.noaa.gov/products/precip/CWlink/pna/nao.shtml, 2013.

Noda, A.: Generalized transformed Eulerian mean (GTEM) description for Boussinesq fluids, Journal of the Meteorological Society of Japan. Ser. II, 92, 411–431, 2014.

Olden, J. D. and Jackson, D. A.: Illuminating the "black box": a randomization approach for understanding variable contributions in artificial neural networks, Ecological Modelling, 154, 135–150, doi:10.1016/S0304-3800(02)00064-9, URL http://linkinghub.elsevier.com/retrieve/pii/S0304380002000649, 2002.

Pasini, A., Lorè, M., and Ameli, F.: Neural network modelling for the analysis of forcings/temperatures relationships at different scales in the climate system, Ecological Modelling, 191, 58–67, doi:10.1016/j.ecolmodel.2005.08.012, URL http://linkinghub.elsevier.com/retrieve/pii/S0304380005003492, 2006.

Pendlebury, D., Plummer, D., Scinocca, J., Sheese, P., Strong, K., Walker, K., and Degenstein, D.: Comparison of the CMAM30 data set with ACE-FTS and OSIRIS: polar regions, Atmospheric Chemistry and Physics, 15, 12 465–12 485, doi:10.5194/acp-15-12465-2015, URL http://www.atmos-chem-phys.net/15/12465/2015/, 2015.

Pfeffer, R. L.: A Study of Eddy-induced Fluctuations of the Zonal-Mean Wind Using Conventional and Transformed Eulerian Diagnostics, Journal of the Atmospheric Sciences, 49, 1036–1050, doi:10.1175/1520-0469(1992)049⟨1036:ASOEIF⟩2.0.CO;2, URL http://journals.ametsoc.org/doi/abs/10.1175/1520-0469{%}281992{%}29049{%}3C1036{%}3AASOEIF{%}3E2.0.CO{%}3B2, 1992.

Pisoft, P., Holtanova, E., Huszar, P., Miksovsky, J., and Zak, M.: Imprint of the 11-year solar cycle in reanalyzed and radiosonde datasets: a spatial frequency analysis approach, Climatic Change, 110, 85–99, doi:10.1007/s10584-011-0147-0, URL http://dx.doi.org/10.1007/s10584-011-0147-0, 2012.

Pisoft, P., Holtanova, E., Huszar, P., Kalvova, J., Miksovsky, J., Raidl, A., Zemankova, K., and Zak, M.: Manifestation of reanalyzed QBO and SSC signals, Theoretical and Applied Climatology, pp. 1–10, 2013.

Pisoft, P., Sacha, P., Miksovsky, J., Huszar, P., Scherllin-Pirscher, B., and Foelsche, U.: Revisiting internal gravity waves analysis using GPS RO density profiles: comparison with temperature profiles and application for wave field stability study, Atmospheric Measurement Techniques, 11, 515–527, doi:10.5194/amt-11-515-2018, URL https://www.atmos-meas-tech.net/11/515/2018/, 2018.

Plumb, R. A.: On the Three-Dimensional Propagation of Stationary Waves, Journal of the Atmospheric Sciences, 42, 217–229, doi:10.1175/1520-0469(1985)042⟨0217:OTTDPO⟩2.0.CO;2, URL http://journals.ametsoc.org/doi/abs/10.1175/1520-0469{%}281985{%}29042{%}3C0217{%}3AOTTDPO{%}3E2.0.CO{%}3B2, 1985.

Plumb, R. A.: Three-dimensional propagation of transient quasi-geostrophic eddies and its relationship with the eddy forcing of the time-mean flow, Journal of the atmospheric sciences, 43, 1657–1678, 1986.

Randel, W. J. and Wu, F.: A stratospheric ozone profile data set for 1979–2005: Variability, trends, and comparisons with column ozone data, Journal of Geophysical Research: Atmospheres, 112, 2156–2202, doi:10.1029/2006JD007339, 2007.

Randel, W. J., Garcia, R. R., and Wu, F.: Time-Dependent Upwelling in the Tropical Lower Stratosphere Estimated from the Zonal-Mean Momentum Budget, Journal of the Atmospheric Sciences, 59, 2141–2152, doi:10.1175/1520-0469(2002)059⟨2141:TDUITT⟩2.0.CO;2, URL http://journals.ametsoc.org/doi/abs/10.1175/1520-0469{%}282002{%}29059{%}3C2141{%}3ATDUITT{%}3E2.0.CO{%}3B2, 2002.

Randel, W. J., Shine, K. P., Austin, J., Barnett, J., Claud, C., Gillett, N. P., Keckhut, P., Langematz, U., Lin, R., Long, C., Mears, C., Miller, A., Nash, J., Seidel, D. J., Thompson, D. W. J., Wu, F., and Yoden, S.: An update of observed stratospheric temperature trends, Journal of Geophysical Research, 114, D02 107, doi:10.1029/2008JD010421, URL http://doi.wiley.com/10.1029/2008JD010421, 2009.

Rayner, N., Parker, D. E., Horton, E., Folland, C., Alexander, L., Rowell, D., Kent, E., and Kaplan, A.: Global analyses of sea surface temperature, sea ice, and night marine air temperature since the late nineteenth century, Journal of Geophysical Research: Atmospheres (1984–2012), 108, 2003.

Remsberg, E. E., Marshall, B. T., Garcia-Comas, M., Krueger, D., Lingenfelser, G. S., Martin-Torres, J., Mlynczak, M. G., Russell, J. M., Smith, A. K., Zhao, Y., Brown, C., Gordley, L. L., Lopez-Gonzalez, M. J., Lopez-Puertas, M., She, C.-Y., Taylor, M. J., and Thompson, R. E.: Assessment of the quality of the Version 1.07 temperature-versus-pressure profiles of the middle atmosphere from TIMED/SABER, Journal of Geophysical Research, 113, D17 101, doi:10.1029/2008JD010013, URL http://doi.wiley.com/10.1029/2008JD010013, 2008.

Revell, L. E., Tummon, F., Stenke, A., Sukhodolov, T., Coulon, A., Rozanov, E., Garny, H., Grewe, V., and Peter, T.: Drivers of the tropospheric ozone budget throughout the 21st century under the medium-high climate scenario RCP 6.0, Atmospheric Chemistry and Physics, 15, 5887–5902, doi:10.5194/acp-15-5887-2015, URL http://www.atmos-chem-phys.net/15/5887/2015/, 2015.

Revell, L. E., Stenke, A., Luo, B., Kremser, S., Rozanov, E., Sukhodolov, T., and Peter, T.: Impacts of Mt Pinatubo volcanic aerosol on the tropical stratosphere in chemistry–climate model simulations using CCMI and CMIP6 stratospheric aerosol data, Atmospheric Chemistry and Physics, 17, 13 139–13 150, doi:10.5194/acp-17-13139-2017, URL https://www.atmos-chem-phys.net/17/13139/2017/, 2017.

Rienecker, M. M., Suarez, M. J., Gelaro, R., Todling, R., Bacmeister, J., Liu, E., Bosilovich, M. G., Schubert, S. D., Takacs, L., Kim, G. K., Bloom, S., Chen, J., Collins, D., Conaty, A., da Silva, A., Gu, W., Joiner, J., Koster, R. D., Lucchesi, R., Molod, A., Owens, T., Pawson, S., Pegion, P., Redder, C. R., Reichle, R., Robertson, F. R., Ruddick, A. G., Sienkiewicz, M., and Woollen, J.: MERRA: NASA's modern-era retrospective analysis for research and applications, Journal of Climate, 24, 3624–3648, 2011.

Robock, A.: Volcanic eruptions and climate, Reviews of Geophysics, 38, 191–219, 2000.

Rosenlof, K. H. and Holton, J. R.: Estimates of the stratospheric residual circulation using the downward control principle, Journal of Geophysical Research: Atmospheres, 98, 10 465–10 479, 1993.

Rozanov, E., Callis, L., Schlesinger, M., Yang, F., Andronova, N., and Zubov, V.: Atmospheric response to NOy source due to energetic electron precipitation, Geophysical Research Letters, 32, 2005.

Šácha, P., Kuchar, A., Jacobi, C., and Pišoft, P.: Enhanced internal gravity wave activity and breaking over the northeastern Pacific-eastern Asian region, Atmospheric Chemistry and Physics, 15, 13 097–13 112, doi:10.5194/acp-15-13097-2015, URL `http://www.atmos-chem-phys.net/15/13097/2015/`, 2015.

Šácha, P., Lilienthal, F., Jacobi, C., and Pišoft, P.: Influence of the spatial distribution of gravity wave activity on the middle atmospheric dynamics, Atmospheric Chemistry and Physics, 16, 15 755–15 775, doi:10.5194/acp-16-15755-2016, 2016.

Sacha, P., Miksovsky, J., and Pisoft, P.: Interannual variability of the gravity wave drag – vertical coupling and possible climate links, Earth System Dynamics Discussions, 2018, 1–23, doi:10.5194/esd-2018-1, URL `https://www.earth-syst-dynam-discuss.net/esd-2018-1/`, 2018.

Sato, K., Kinoshita, T., and Okamoto, K.: A New Method to Estimate Three-Dimensional Residual-Mean Circulation in the Middle Atmosphere and Its Application to Gravity Wave-Resolving General Circulation Model Data, Journal of the Atmospheric Sciences, 70, 3756–3779, doi:10.1175/JAS-D-12-0352.1, URL `http://journals.ametsoc.org/doi/abs/10.1175/JAS-D-12-0352.1`, 2013.

Sato, M., Hansen, J. E., McCormick, M. P., and Pollack, J. B.: Stratospheric aerosol optical depths, 1850-1990, Journal of Geophysical Research: Atmospheres, 98, 22 987–22 994, doi:10.1029/93JD02553, URL `http://dx.doi.org/10.1029/93JD02553`, 1993.

Scaife, A. A., Ineson, S., Knight, J. R., Gray, L., Kodera, K., and Smith, D. M.: A mechanism for lagged North Atlantic climate response to solar variability, Geophysical Research Letters, 40, 434–439, 2013.

Scheffler, G. and Pulido, M.: Compensation between Resolved and Unresolved Wave Drag in the Stratospheric Final Warmings of the Southern Hemisphere, Journal of the Atmospheric Sciences, 72, 4393–4411, doi:10.1175/JAS-D-14-0270.1, URL http://journals.ametsoc.org/doi/10.1175/JAS-D-14-0270.1, 2015.

Scherhag, R.: Die explosionsartigen Stratospharenerwarmungen des Spatwinters 1951-1952, Ber. Deut. Wetterd., 6, 51–63, URL http://ci.nii.ac.jp/naid/10025673833/en/, 1952.

Schmidt, H., Brasseur, G. P., and Giorgetta, M. A.: Solar cycle signal in a general circulation and chemistry model with internally generated quasi-biennial oscillation, Journal of Geophysical Research: Atmospheres, 115, doi:10.1029/2009JD012542, 2010.

Scinocca, J. F.: An Accurate Spectral Nonorographic Gravity Wave Drag Parameterization for General Circulation Models, Journal of the Atmospheric Sciences, 60, 667–682, doi:10.1175/1520-0469(2003)060⟨0667:AASNGW⟩2.0.CO;2, URL http://journals.ametsoc.org/doi/abs/10.1175/1520-0469{%}282003{%}29060{%}3C0667{%}3AAASNGW{%}3E2.0.CO{%}3B2, 2003.

Scinocca, J. F. and McFarlane, N. A.: The parametrization of drag induced by stratified flow over anisotropic orography, Quarterly Journal of the Royal Meteorological Society, 126, 2353–2393, doi:10.1002/qj.49712656802, URL http://doi.wiley.com/10.1002/qj.49712656802, 2000.

Scinocca, J. F., McFarlane, N. A., Lazare, M., Li, J., and Plummer, D.: Technical Note: The CCCma third generation AGCM and its extension into the middle atmosphere, Atmospheric Chemistry and Physics, 8, 7055–7074, doi:10.5194/acp-8-7055-2008, URL http://www.atmos-chem-phys.net/8/7055/2008/, 2008.

Scott, R. K. and Polvani, L. M.: Stratospheric control of upward wave flux near the tropopause, Geophysical Research Letters, 31, doi:10.1029/2003GL017965, URL http://doi.wiley.com/10.1029/2003GL017965, 2004.

Seabold, S. and Perktold, J.: Statsmodels: Econometric and statistical modeling with python, in: Proceedings of the 9th Python in Science Conference, 2010.

Seppälä, A., Lu, H., Clilverd, M. A., and Rodger, C. J.: Geomagnetic activity signatures in wintertime stratosphere wind, temperature, and wave response, Journal of Geophysical Research: Atmospheres, 118, 2169–2183, doi:10.1002/jgrd.50236, URL http://doi.wiley.com/10.1002/jgrd.50236, 2013.

Seppälä, A., Matthes, K., Randall, C., and Mironova, I.: What is the solar influence on climate? Overview of activities during CAWSES-II, European Journal of Nuclear Medicine and Molecular Imaging, 1, 1–12, 2014.

Seviour, W. J., Butchart, N., and Hardiman, S. C.: The Brewer–Dobson circulation inferred from ERA-Interim, Quarterly Journal of the Royal Meteorological Society, 138, 878–888, 2012.

Seviour, W. J. M., Mitchell, D. M., and Gray, L. J.: A practical method to identify displaced and split stratospheric polar vortex events, Geophysical Research Letters, 40, 5268–5273, doi:10.1002/grl.50927, URL http://doi.wiley.com/10.1002/grl.50927, 2013.

Shaw, T. A. and Boos, W. R.: The Tropospheric Response to Tropical and Subtropical Zonally Asymmetric Torques: Analytical and Idealized Numerical Model Results, Journal of the Atmospheric Sciences, 69, 214–235, doi:10.1175/JAS-D-11-0139.1, URL http://journals.ametsoc.org/doi/abs/10.1175/JAS-D-11-0139.1, 2012.

Shepherd, T. G., Plummer, D. A., Scinocca, J. F., Hegglin, M. I., Fioletov, V. E., Reader, M. C., Remsberg, E., Von Clarmann, T., and Wang, H. J.: Reconciliation of halogen-induced ozone loss with the total-column ozone record, Nature Geoscience, 7, 443–449, doi:10.1038/ngeo2155, 2014.

Simpson, I. R., Blackburn, M., and Haigh, J. D.: The role of eddies in driving the tropospheric response to stratospheric heating perturbations, Journal of the Atmospheric Sciences, 66, 1347–1365, 2009.

Smith, A. K. and Matthes, K.: Decadal-scale periodicities in the stratosphere associated with the solar cycle and the QBO, Journal of Geophysical Research: Atmospheres, 113, n/a–n/a, doi:10.1029/2007JD009051, URL http://doi.wiley.com/10.1029/2007JD009051, 2008.

Solomon, S., Portmann, R. W., Garcia, R. R., Thomason, L. W., Poole, L. R., and McCormick, M. P.: The role of aerosol variations in anthropogenic ozone depletion at northern midlatitudes, Journal of Geophysical Research: Atmospheres, 101, 6713–6727, doi:10.1029/95JD03353, URL http://dx.doi.org/10.1029/95JD03353, 1996.

Song, B.-G. and Chun, H.-Y.: Residual Mean Circulation and Temperature Changes during the Evolution of Stratospheric Sudden Warming Revealed in MERRA, Atmospheric Chemistry and Physics Discussions, 2016, 1–26, doi:10.5194/acp-2016-729, URL https://www.atmos-chem-phys-discuss.net/acp-2016-729/, 2016.

Song, Y. and Robinson, W. A.: Dynamical mechanisms for stratospheric influences on the troposphere, Journal of the atmospheric sciences, 61, 1711–1725, 2004.

Soukharev, B. E. and Hood, L. L.: Solar cycle variation of stratospheric ozone: Multiple regression analysis of long-term satellite data sets and comparisons with models, Journal of Geophysical Research: Atmospheres, 111, 20 314, 2006.

Standard atmosphere: URL http://www.sworld.com.au/steven/space/atmosphere/, date of last access: 2018-06, 1976.

Stenke, A., Schraner, M., Rozanov, E., Egorova, T., Luo, B., and Peter, T.: The SOCOL version 3.0 chemistry climate model: description, evaluation, and implications from an advanced transport algorithm, Geoscientific Model Development, 6, 1407–1427, doi:10.5194/gmd-6-1407-2013, URL http://www.geosci-model-dev.net/6/1407/2013/, 2013.

Sukhodolov, T., Rozanov, E., Ball, W. T., Peter, T., and Schmutz, W.: Modeling of the middle atmosphere response to 27-day solar irradiance variability, Journal of Atmospheric and Solar-Terrestrial Physics, 152-153, 50–61, doi:10.1016/j.jastp.2016.12.004, URL http://linkinghub.elsevier.com/retrieve/pii/S136468261630428X, 2017.

Takaya, K. and Nakamura, H.: Mechanisms of intraseasonal amplification of the cold Siberian high, Journal of the Atmospheric Sciences, 62, 4423–4440, 2005.

Teixeira, M. A.: The physics of orographic gravity wave drag, Frontiers in Physics, 2, 43, 2014.

Thejll, P.and Schmith, T.: Limitations on regression analysis due to serially correlated residuals: Application to climate reconstruction from proxies, Journal of geophysical research, 110, D18 103, 2005.

Thiéblemont, R., Matthes, K., Omrani, N.-E., Kodera, K., and Hansen, F.: Solar forcing synchronizes decadal North Atlantic climate variability, Nature Communications, 6, 8268, doi:10.1038/ncomms9268, URL http://www.nature.com/doifinder/10.1038/ncomms9268, 2015.

Thorne, P. W., Parker, D. E., Tett, S. F., Jones, P. D., McCarthy, M., Coleman, H., and Brohan, P.: Revisiting radiosonde upper air temperatures from 1958 to 2002, Journal of Geophysical Research: Atmospheres, 110, 2005.

Tiao, G. C., Reinsel, G. C., Xu, D., Pedrick, J. H., Zhu, X., Miller, A. J., DeLuisi, J. J., Mateer, C. L., and Wuebbles, D. J.: Effects of autocorrelation and temporal sampling schemes on estimates of trend and spatial correlation, Journal of Geophysical Research: Atmospheres, 95, 20 507–20 517, doi:10.1029/JD095iD12p20507, URL http://dx.doi.org/10.1029/JD095iD12p20507, 1990.

Torrence, C. and Compo, G. P.: A practical guide to wavelet analysis, Bulletin of the American Meteorological society, 79, 61–78, 1998.

van Loon, H. and Labitzke, K.: The Influence of the 11-year Solar Cycle on the Stratosphere Below 30 km: a Review, Space Science Reviews, 94, 259–278, doi:10.1023/A:1026731625713, URL http://dx.doi.org/10.1023/A%3A1026731625713, 2000.

van Loon, H. and Meehl, G. A.: The response in the Pacific to the Sun's decadal peaks and contrasts to cold events in the Southern Oscillation, Journal of Atmospheric and Solar-Terrestrial Physics, 70, 1046–1055, 2008.

van Loon, H., Meehl, G., and Shea, D.: The effect of the decadal solar oscillation in the Pacific troposphere in northern winter, J. Geophys. Res, 112, D02 108, 2007.

Vernier, J.-P., Thomason, L. W., Pommereau, J.-P., Bourassa, A., Pelon, J., Garnier, A., Hauchecorne, A., Blanot, L., Trepte, C., Degenstein, D., and Vargas, F.: Major influence of tropical volcanic eruptions on the stratospheric aerosol

layer during the last decade, Geophysical Research Letters, 38, n/a–n/a, doi:10.1029/2011GL047563, URL http://dx.doi.org/10.1029/2011GL047563, l12807, 2011.

Walter, A. and Schönwiese, C. D.: Nonlinear statistical attribution and detection of anthropogenic climate change using a simulated annealing algorithm, Theoretical and Applied Climatology, 76, 1–12, doi:10.1007/s00704-003-0008-5, URL http://link.springer.com/10.1007/s00704-003-0008-5, 2003.

Wang, W., Matthes, K., Omrani, N.-E., and Latif, M.: Decadal variability of tropical tropopause temperature and its relationship to the Pacific Decadal Oscillation, Scientific Reports, 6, 29 537, doi:10.1038/srep29537, URL http://www.nature.com/articles/srep29537, 2016.

Watanabe, S., Kawatani, Y., Tomikawa, Y., Miyazaki, K., Takahashi, M., and Sato, K.: General aspects of a T213L256 middle atmosphere general circulation model, Journal of Geophysical Research, 113, D12 110, doi:10.1029/2008JD010026, URL http://doi.wiley.com/10.1029/2008JD010026, 2008.

White, R. H., Battisti, D. S., and Sheshadri, A.: Orography and the Boreal Winter Stratosphere: The Importance of the Mongolian Mountains, Geophysical Research Letters, 45, 2088–2096, doi:10.1002/2018GL077098, URL http://doi.wiley.com/10.1002/2018GL077098, 2018.

Xu, X., Wang, Y., Xue, M., and Zhu, K.: Impacts of Horizontal Propagation of Orographic Gravity Waves on the Wave Drag in the Stratosphere and Lower Mesosphere, Journal of Geophysical Research: Atmospheres, 122, 11,301–11,312, doi:10.1002/2017JD027528, URL http://doi.wiley.com/10.1002/2017JD027528, 2017.

Xu, X., Tang, Y., Wang, Y., and Xue, M.: Directional Absorption of Parameterized Mountain Waves and Its Influence on the Wave Momentum Transport in the Northern Hemisphere, Journal of Geophysical Research: Atmospheres, pp. 1–15, doi:10.1002/2017JD027968, URL http://doi.wiley.com/10.1002/2017JD027968, 2018.

Yeo, K. L., Krivova, N. A., Solanki, S. K., and Glassmeier, K. H.: Reconstruction of total and spectral solar irradiance from 1974 to 2013 based on KPVT, SoHO/MDI, and SDO/HMI observations, A&A, 570, A85, doi:10.1051/0004-6361/201423628, URL https://doi.org/10.1051/0004-6361/201423628, 2014.

Zou, C.-Z. and Qian, H.: Stratospheric Temperature Climate Data Record from Merged SSU and AMSU-A Observations, Journal of Atmospheric and Oceanic Technology, pp. JTECH–D–16–0018.1, doi:10.1175/JTECH-D-16-0018.1, URL http://journals.ametsoc.org/doi/10.1175/JTECH-D-16-0018.1http://www.star.nesdis.noaa.gov/star/smcdTeam{_}StratosTemp.phphttp://www.star.nesdis.noaa.gov/smcd/emb/mscat/, 2016.

Zyulyaeva, Y. A. and Zhadin, E.: Analysis of three-dimensional Eliassen-Palm fluxes in the lower stratosphere, Russian Meteorology and Hydrology, 34, 483, 2009.

List of Figures

List of Tables

List of publications

Sacha, P., **Kuchar, A.**, Jacobi, C. and Pisoft, P. (2015). Enhanced internal gravity wave activity and breaking over the northeastern Pacific-eastern Asian region. *Atmospheric Chemistry and Physics*, 15(22), 13097–13112. http://doi.org/10.5194/acp-15-13097-2015

Kuchar, A., Sacha, P., Miksovsky, J. and Pisoft, P. (2015). The 11-year solar cycle in current reanalyses: a (non)linear attribution study of the middle atmosphere. *Atmospheric Chemistry and Physics*, 15(12), 6879–6895. http://doi.org/10.5194/acp-15-6879-2015

Ball, W. T., **Kuchar, A.**, Rozanov, E. V., Staehelin, J., Tummon, F., Smith, A. K., Sukhodolov, T., Stenke, A., Revell, L., Coulon, A., Schmutz, W. and Peter, T. (2016). An upper-branch Brewer-Dobson circulation index for attribution of stratospheric variability and improved ozone and temperature trend analysis. *Atmospheric Chemistry and Physics*, 16(24), 15485–15500. http://doi.org/10.5194/acp-16-15485-2016

Muthers, S., **Kuchar, A.**, Stenke, A., Schmitt, J., Anet, J. G., Raible, C. C. and Stocker, T. F. (2016). Stratospheric age of air variations between 1600-2100. Geophysical Research Letters. http://doi.org/10.1002/2016GL068734

Ball, W. T., Haigh, J. D., Rozanov, E. V., **Kuchar, A.**, Sukhodolov, T., Tummon, F., Shapiro, A. V. and Schmutz, W. (2016). High solar cycle spectral variations inconsistent with stratospheric ozone observations. *Nature Geoscience*, 9(3), 206–209. http://doi.org/10.1038/ngeo2640

Kuchar, A., Ball, W. T., Rozanov, E. V., Stenke, A., Revell, L., Miksovsky, J., Pisoft, P. and Peter, T. (2017). On the aliasing of the solar cycle in the lower stratospheric tropical temperature. *Journal of Geophysical Research: Atmospheres*, 122(17), 9076–9093. http://doi.org/10.1002/2017JD026948

Appendices

A. oGWD contribution to the total wave forcing in CCMI-SD models

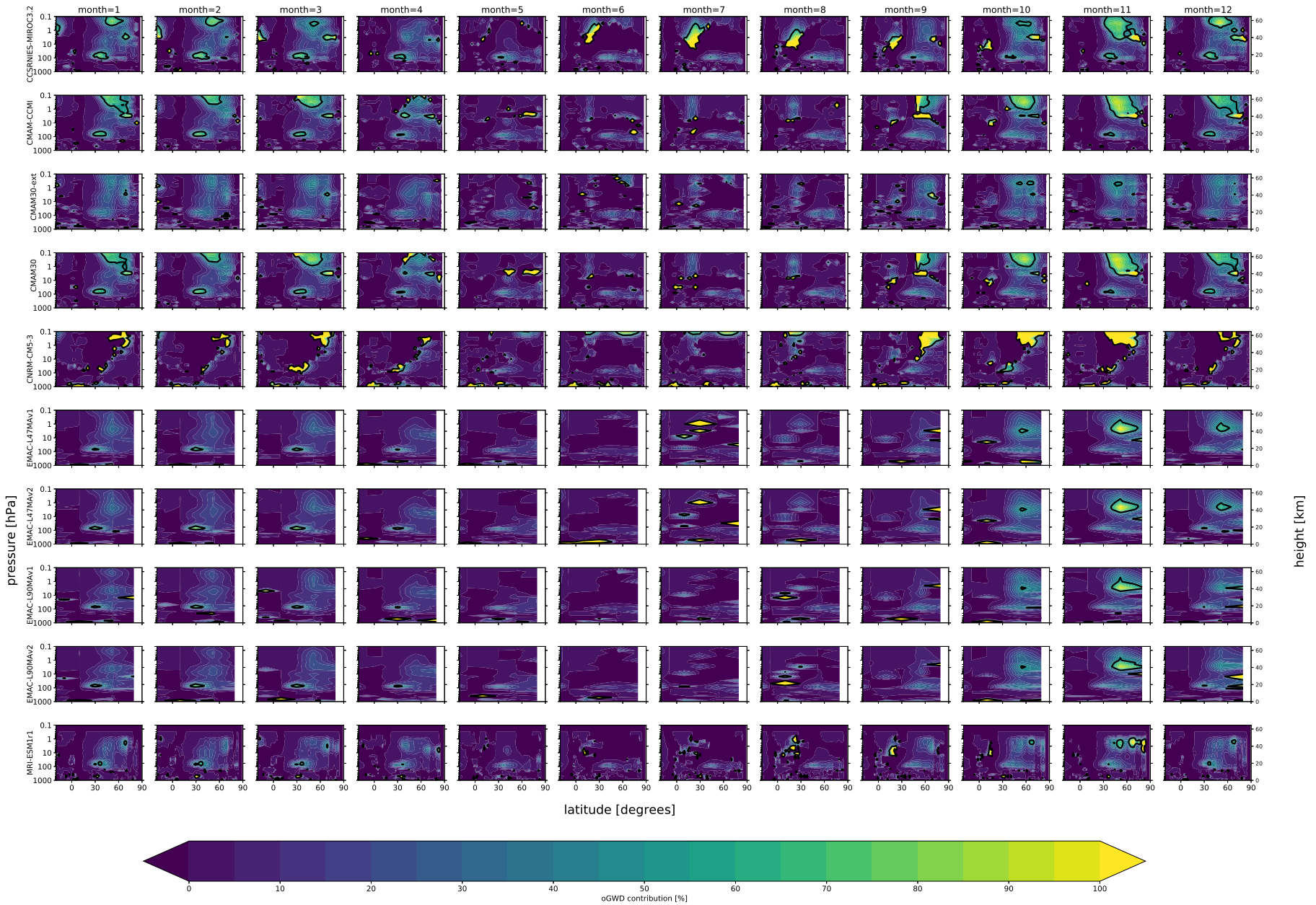

Figure A.1: Percentage that orographic zonally averaged GWD (oGWD) in zonal direction contributes to the total wave forcing (resolved waves represented by EPFD + oGWD + nGWD) for climatological average of the period 1990-2010 in CMAM30, CMAM30-ext and CCMI REFC1-SD simulations: CCSRNIES-MIROC3.2, CMAM-CCMI, CNRM-CM5-3, EMAC-L90MA-v1, EMAC-L90MA-v2, EMAC-L47MA-v1, EMAC-L47MA-v2 and MRI-ESM1r1. Black contour represents 50% contribution of oGWD. The latitudes are limited from 20°S to 90°N.

B. Additional composite outputs

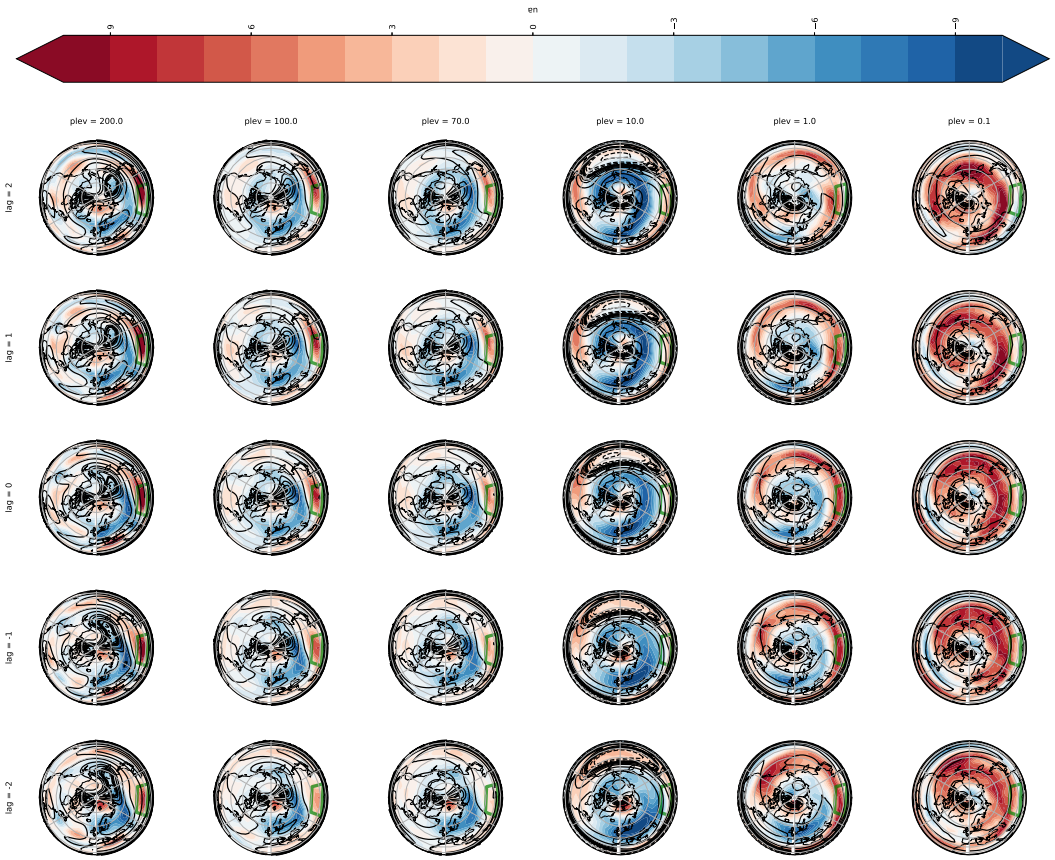

Figure B.1: Anomalous (shading; units: m/s) and absolute (black contours, solid contours for positive values and dashed for negative values when zero contour is shown by bold contour; units: m/s) values of zonal wind composite averages at lags between -2 and +2 representing the Himalayan events. Maps in Orthographic projection show zonal wind at $\{200; 100; 70; 10; 1; 0.1\}$ hPa. The green box represents the Himalayan hotspot.

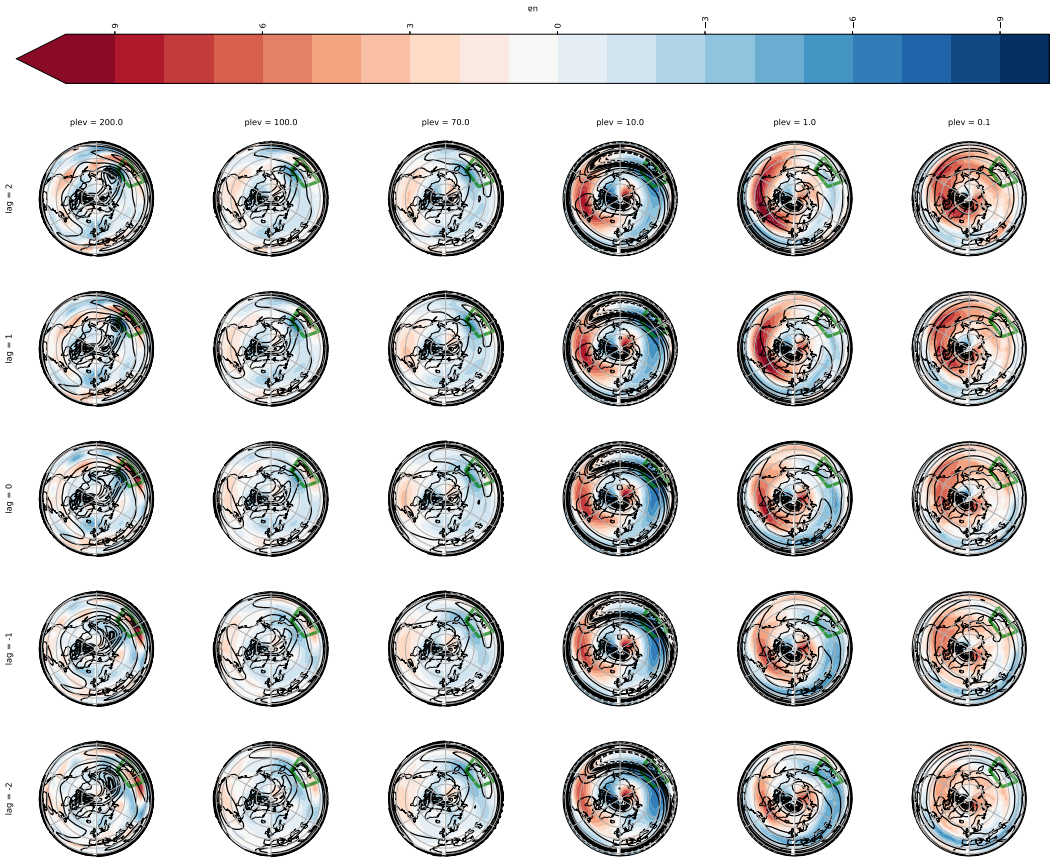

Figure B.2: Anomalous (shading; units: m/s) and absolute (black contours, solid contours for positive values and dashed for negative values when zero contour is shown by bold contour; units: m/s) values of zonal wind composite averages at lags between -2 and +2 representing East Asian events. Maps in Orthographic projection show zonal wind at $\{200; 100; 70; 10; 1; 0.1\}$ hPa. The green box represents the East-Asian hotspot.

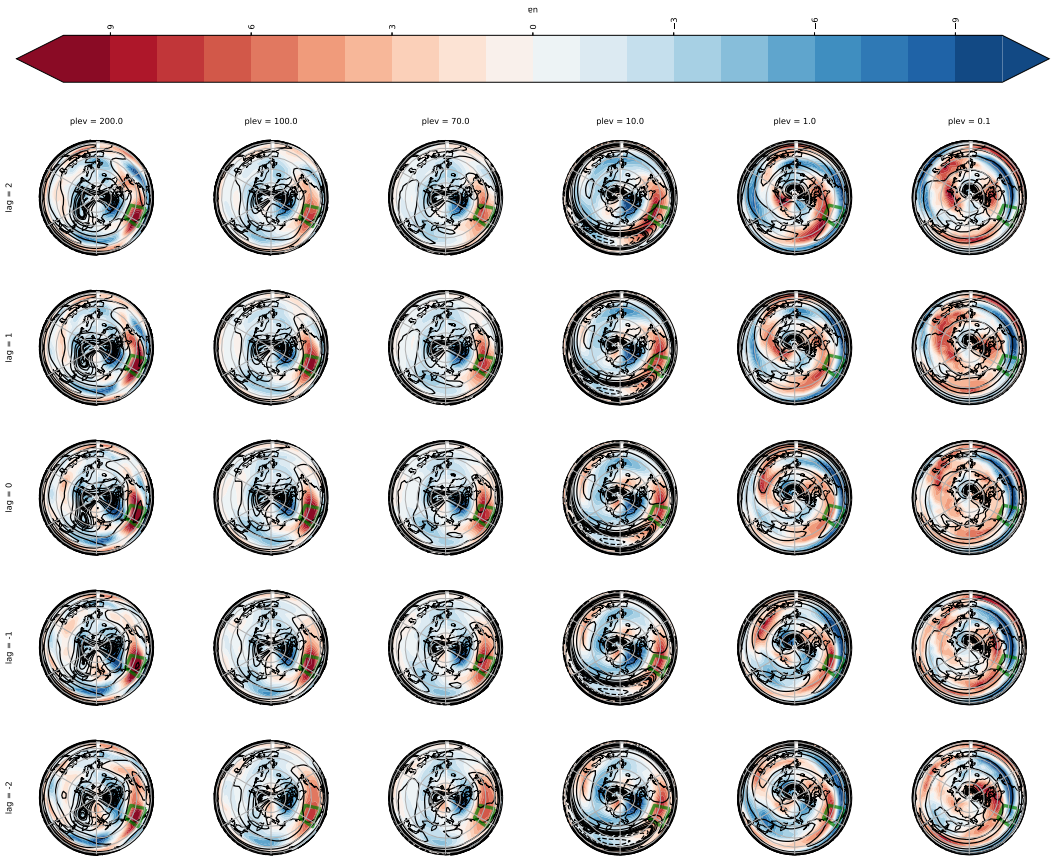

Figure B.3: Anomalous (shading; units: m/s) and absolute (black contours, solid contours for positive values and dashed for negative values when zero contour is shown by bold contour; units: m/s) values of zonal wind composite averages at lags between -2 and +2 representing West American events. Maps in Orthographic projection show zonal wind at $\{200; 100; 70; 10; 1; 0.1\}$ hPa. The green box represents the West-American hotspot.

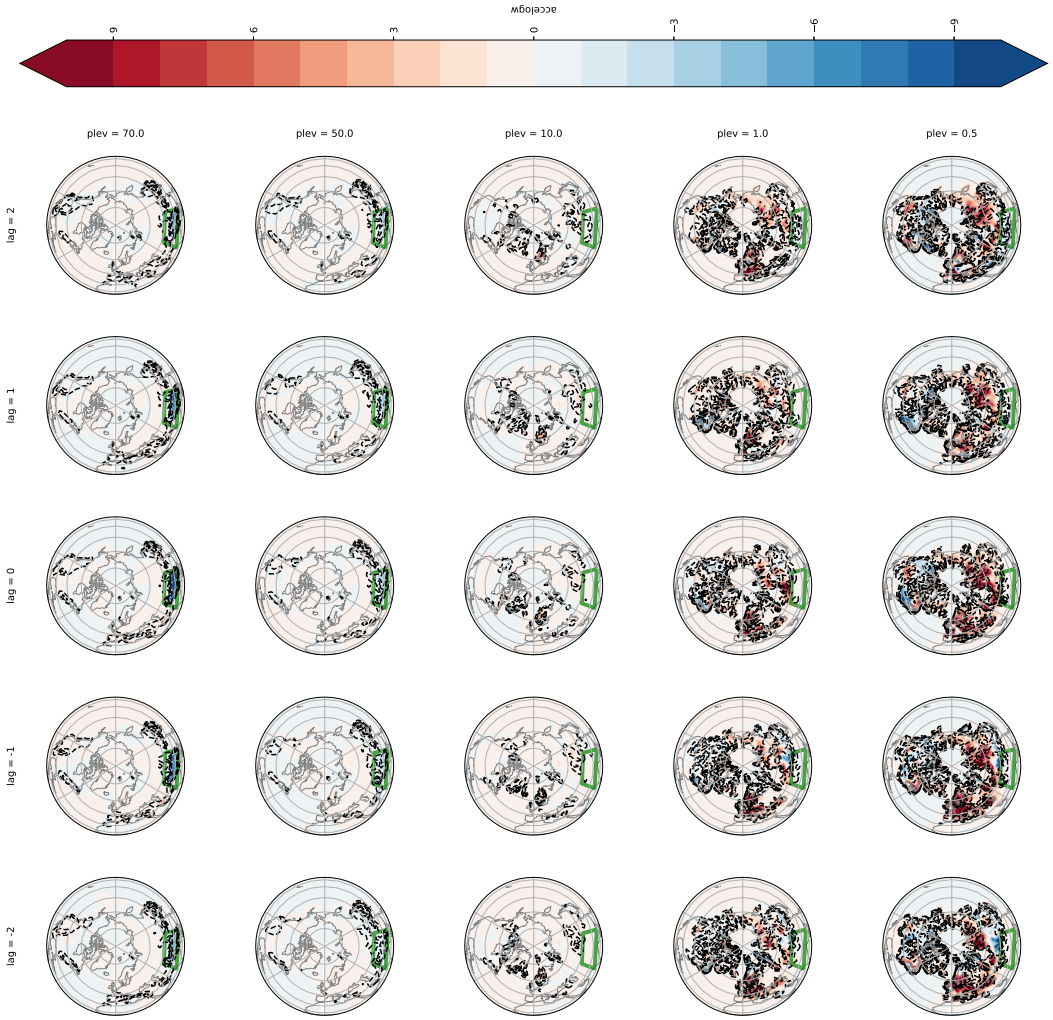

Figure B.4: Anomalous (shading; units: m/s/day) and absolute (black contours, solid contours for positive values and dashed for negative values when zero contour is shown by bold contour; units: m/s/day) values of oGWD composite averages at lags between -2 and +2 representing Himalayan events. Maps in Orthographic projection show zonal wind at $\{70; 50; 10; 1; 0.5\}$ hPa. The green box represents the Himalayan hotspot.

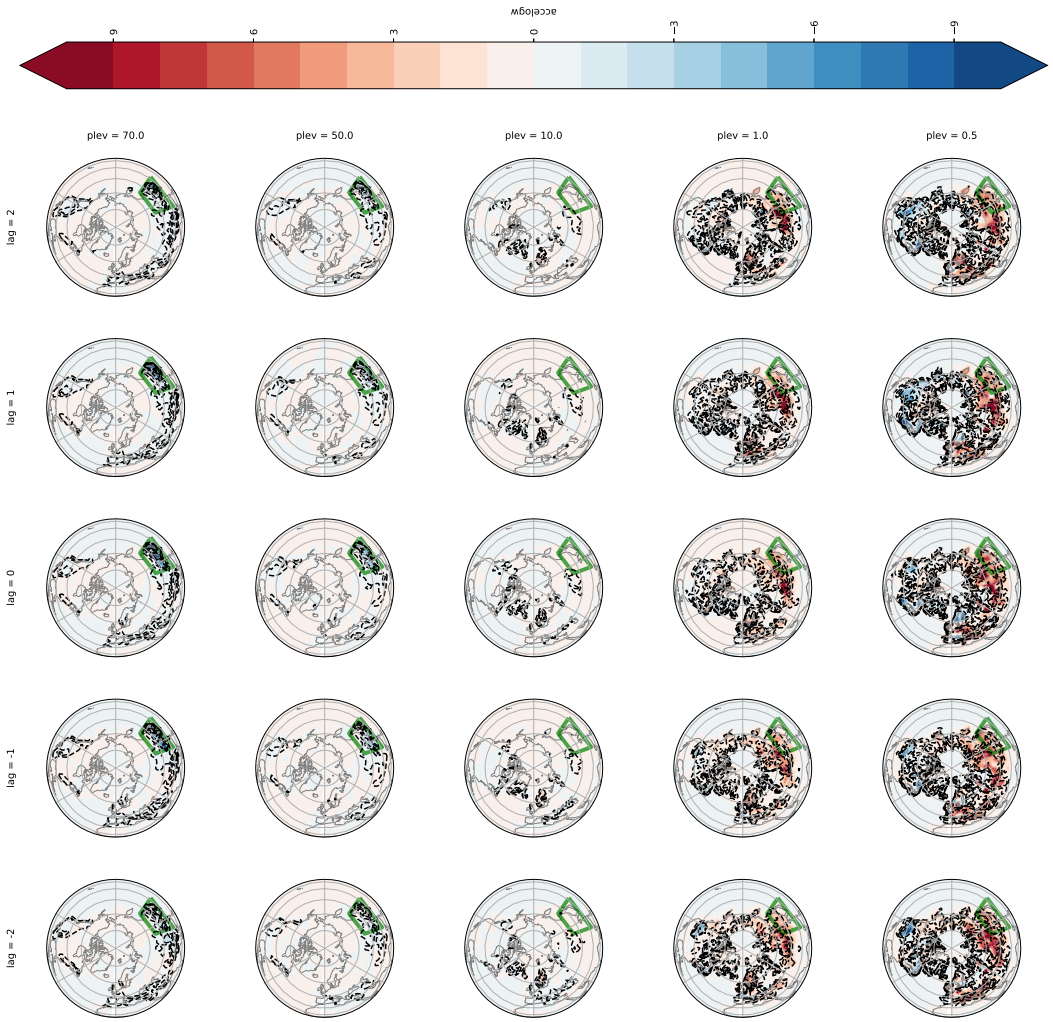

Figure B.5: Anomalous (shading; units: m/s/day) and absolute (black contours, solid contours for positive values and dashed for negative values when zero contour is shown by bold contour; units: m/s/day) values of oGWD composite averages at lags between -2 and +2 representing East Asian events. Maps in Orthographic projection show zonal wind at $\{70; 50; 10; 1; 0.5\}$ hPa. The green box represents the East Asian hotspot.

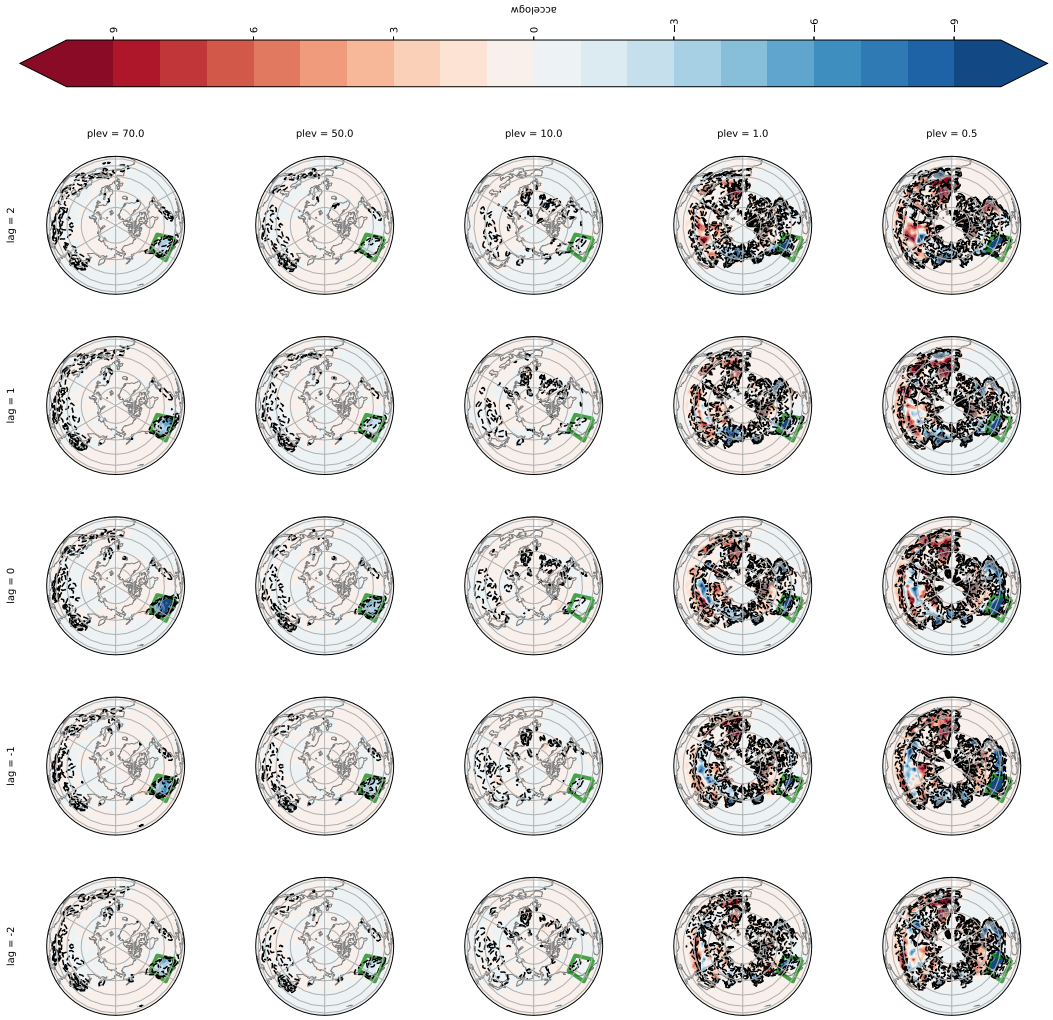

Figure B.6: Anomalous (shading; units: m/s/day) and absolute (black contours, solid contours for positive values and dashed for negative values when zero contour is shown by bold contour; units: m/s/day) values of oGWD composite averages at lags between -2 and +2 representing West American events. Maps in Orthographic projection show zonal wind at $\{70; 50; 10; 1; 0.5\}$ hPa. The green box represents the West American hotspot.